THE MEASUREMENT OF INSTANTANEOUS, LOCAL HEAT TRANSFER FROM A HORIZONTALLY VIBRATING ISOTHERMAL CYLINDER USING A DIFFERENTIAL INTERFEROMETER

A THESIS

Presented to

The Faculty of the Division of Graduate

Studies and Research

By

Wallace Woodrow Carr

In Partial Fulfillment

of the Requirements for the Degree

Doctor of Philosophy in the

School of Mechanical Engineering

Georgia Institute of Technology

March, 1973

THE MEASUREMENT OF INSTANTANEOUS, LOCAL HEAT TRANSFER FROM A HORIZONTALLY VIBRATING ISOTHERMAL CYLINDER USING A DIFFERENTIAL INTERFEROMETER

Approved:

William Z. Black, Chairman

P. V. Kadaba

K. C. Williams

E. W. Thomas

H. C. Ward

Date approved by Chairman: 3/7/73

ACKNOWLEDGMENTS

The author would like to express his appreciation to all those who have contributed their help and encouragement to this work. Special appreciation is due Dr. W. Z. Black, the faculty advisor for this thesis, who suggested this thesis. Dr. Black's understanding, encouragement, and professional advice throughout the course of this work has led to its completion. The constructive comments and time given by those who have served on the author's thesis committee, Dr. P. V. Kadaba, Dr. K. C. Williams, Dr. A. E. Bergles, Dr. E. W. Thomas, and Dr. H. C. Ward, are gratefully acknowledged.

The assistance in the fabrication of the experimental equipment of Messrs. C. R. Bannister, L. A. Cavalli, and J. W. Davis, is very much appreciated. A special word of appreciation is extended to Messrs. H. J. Carr and B. L. Wallace for their advice and assistance in the fabrication of the vibrational equipment. Special thanks is extended to Messrs. J. G. Doyal and T. E. Clopton for their willingness to assist in any way they could. Mr. T. E. Clopton is especially thanked for providing his electronic expertise. Special thanks are due the author's father, Mr. J. M. Carr, Sr., who assisted in the design and fabrication of the test cylinder and its supports.

The assistance in data reduction of Messrs. R. L. Somers, L. J. Jefferson, and J. Farmer is gratefully acknowledged, and the author is indebted to Mr. J. L. Hagerman for his assistance in the fabrication of the shield and for his photographic assistance. The careful preparation of figures by Mr. H. Smith is appreciated, and the arduous job of typing by Mrs. Sharon Butler is gratefully acknowledged.

The guidance, patience, and encouragement of the author's parents throughout his entire educational career is gratefully acknowledged. Finally, the author would like to express his appreciation to his wife, Catherine, for her continual assistance, encouragement, and love throughout this study.

TABLE OF CONTENTS

Page

ACKNOWLEDGMENTS ii

LIST OF TABLES vii

LIST OF ILLUSTRATIONS viii

NOMENCLATURE xii

SUMMARY xxv

Chapter

I. INTRODUCTION 1

II. LITERATURE SURVEY 4

Introduction
Average Heat-Transfer Measurements for Mechanical Vibrations
Local Heat-Transfer Measurements

III. THE DIFFERENTIAL INTERFEROMETER 28

Introduction and Historical Background
Principles of Operation
Application of the Differential Interferometer to Heat-Transfer Problems

IV. SCOPE OF THE EXPERIMENT 55

Flat Plate
Horizontal Cylinder

V. APPARATUS 59

Flat Plate
Cylinder
The Differential Interferometer and Shield
Vibrational Equipment
Photography and Interferogram Analysis
Supporting Equipment

Chapter Page

VI. EXPERIMENTAL PROCEDURE AND DATA REDUCTION. . . . 70

Flat Plate
Stationary Horizontal Cylinder
Vibrating Horizontal Cylinder

VII. RESULTS AND HEAT-TRANSFER CORRELATION. 84

Stationary Tests
Flat Plate
Horizontal Cylinder
Vibratory Tests
Important Dimensionless Numbers
Instantaneous, Local Heat Transfer
Instantaneous, Average Heat Transfer
Average, Local Heat Transfer
Average Heat Transfer
Correlation for $\overline{Nu}_y$
Qualitative Flow Visualization
Discussion of Error Analysis and Reproducibility

VIII. CONCLUSIONS. 160

IX. RECOMMENDATIONS. 162

APPENDIX

A. THE WOLLASTON PRISM. 165

Birefringent Materials
Separation of Rays
Wollaston Prism for Fringe Production

B. ALIGNMENT PROCEDURES FOR THE DIFFERENTIAL INTERFEROMETER. 185

C. EXPERIMENTAL MEASUREMENT OF RAY SEPARATION DISTANCE. 187

D. THE PROPERTIES OF AIR. 189

Gladstone-Dale Constant
Density
Coefficient of Thermal Expansion
Thermal Conductivity
Absolute Viscosity

APPENDIX Page

E. AVERAGE HEAT-TRANSFER COEFFICIENT BY AN ENERGY BALANCE. 193

Radiative Loss From the Cylinder
Convective End Loss
Conductive Loss Through Supports
Thermocouple Lead Loss
Electrical Lead Loss
Average Heat-Transfer Coefficient for Stationary Cylinder
Average Heat-Transfer Coefficient for Vibrating Cylinder

F. COMPUTER PROGRAM FOR DATA REDUCTION. 203

G. IMPORTANT PARAMETERS FROM DIMENSIONLESS GOVERNING EQUATIONS. 206

H. COMPUTER PROGRAM FOR DATA CORRELATION. 215

I. ERROR ANALYSIS 217

BIBLIOGRAPHY 232

VITA 242

LIST OF TABLES

Table		Page
1.	Summary of Test Conditions.	58
2.	Maximum and Minimum Per Cent Changes in $Nu_v(\theta,\psi)$ Relative to $Nu_F(\theta)$	96
3.	Maximum and Minimum Per cent Changes in $Nu_v(\psi)$ Relative to $Nu_F(\theta)$.	111
4.	Comparison of $\overline{Nu}_v$ and $\overline{Nu}_{bal}$	126
5.	Comparison of $\overline{Nu}_v$ and $\overline{Nu}_F$	127
6.	Tabulation of Estimated Errors for Instantaneous, Local Heat-Transfer Measurements .	157
7.	Sets of Dimensionless Parameters.	214
8.	Tabulation of e_{approx} as a Function for Three Temperature Differences	224
9.	Tabulation of e_{end} as a Function of $(\frac{\Delta x_s}{\delta})$ For Several Values of $(\frac{\delta}{L})$	227

LIST OF ILLUSTRATIONS

Figure		Page
1.	Schematic Diagram of a Differential Interferometer.	34
2.	Division of a Single Ray Into Two Components. . .	36
3.	Schematic Diagram of the Recombination of Ray x and Ray y Which Form an Original Incident Ray . .	38
4.	Resulting Fringe Pattern at Eyepiece for an Isothermal Test Section	43
5.	Hypothetical Fringe Pattern at Eyepiece for a Heated Test Object in the Test Section.	45
6.	Infinite Fringe Lines Corresponding to a Constant Gradient of n Perpendicular to Plate . .	47
7.	Ray Separation and Blockage Causing the Double Image on the Test Object.	49
8.	Test Cylinder	60
9.	Locations of Cylinder and Support Thermocouples .	62
10.	The Differential Interferometer and Shield. . . .	64
11.	Vibrational System.	67
12.	Determination of the Normal Component of Temperature Gradient on a Curved Surface.	73
13.	Hypothetical Undeflected Horizontal Fringe Pattern.	76
14.	Schematic Diagram of One Oscillation of the Cylinder.	81
15.	Local Convective Heat-Transfer Coefficient from a Vertical Isothermal Plate	86
16.	Local Variation of Nusselt Number for Stationary Tests.	88

Figure		Page
17.	Local Free Convective Heat-Transfer Coefficient from a Horizontal Cylinder.	89
18.	Distribution of Local Nusselt Number Around Circumference of Circular Cylinder for Forced Convection [42].	98
19.	Distribution of $Nu_V(\theta,\psi)$ with θ for $\frac{A}{D} = 0.1179$, $Re_A = 141$, and $Gr = 25{,}321$.	99
20.	Distribution of $Nu_V(\theta,\psi)$ with θ for $\frac{A}{D} = 0.5007$, $Re_A = 151$, and $Gr = 25{,}590$.	101
21.	Distribution of $Nu_V(\theta,\psi)$ with θ for $\frac{A}{D} = 1.7818$, $Re_A = 155$, and $Gr = 25{,}517$.	102
22.	Distribution of $Nu_V(\theta,\psi)$ with θ for $\frac{A}{D} = 0.5182$, $Re_A = 617$, and $Gr = 24{,}902$.	104
23.	Distribution of $Nu_V(\theta,\psi)$ with θ for $\frac{A}{D} = 1.7760$, $Re_A = 610$, and $Gr = 25{,}469$.	105
24.	Distribution of $Nu_V(\theta,\psi)$ with θ for $\frac{A}{D} = 0.5071$, $Re_A = 304$, and $Gr = 25{,}207$.	106
25.	Distribution of $Nu_V(\theta,\psi)$ with θ for $\frac{A}{D} = 0.5198$, $Re_A = 148$, and $Gr = 44{,}025$.	108
26.	Distribution of $Nu_V(\theta,\psi)$ with θ for $\frac{A}{D} = 0.5132$, $Re_A = 137$, and $Gr = 74{,}429$.	109
27.	Variation in Instantaneous Average Nusselt Number, $Nu_V(\psi)$, with the Amplitude to Diameter Ratio, $\frac{A}{D}$.	113
28.	The Effect of Increasing Re_A on $Nu_V(\psi)$.	114
29.	The Effect of Increasing Gr on $Nu_V(\psi)$	115
30.	Comparison of $Nu_V(\psi)$ at ψ of 90° with Forced and Mixed Free-Forced Convection for $Gr = 2.4 \times 10^4$.	117
31.	Comparison of $Nu_V(\psi)$ at ψ of 90° with Forced and Mixed Free-Forced Convection for $Gr = 4.4 \times 10^4$.	118

Figure		Page
32.	Comparison of $Nu_V(\psi)$ at ψ of 90° with Forced and Mixed Free-Forced Convection for $Gr = 7.4 \times 10^4$	119
33.	Distribution of $Nu_V(\theta)$ with θ for $\frac{A}{D} = 0.41$, $Gr = 24{,}956$, and $Re_A = 660$	121
34.	Distribution of $Nu_V(\theta)$ with θ for $\frac{A}{D} = 1.78$, $Gr = 25{,}469$, and $Re_A = 610$	123
35.	Comparison of $\overline{Nu}_V$ with Forced and Mixed Free-Forced Convection for $Gr = 2.4 \times 10^4$	129
36.	Comparison of $\overline{Nu}_V$ with Forced and Mixed Free-Forced Convection for $Gr = 4.4 \times 10^4$	130
37.	Comparison of $\overline{Nu}_V$ with Forced and Mixed Free-Forced Convection for $Gr = 7.4 \times 10^4$	131
38.	Correlation for $\frac{\overline{Nu}_V}{\overline{Nu}_F}$ Expressed in Equation (83)	138
39.	Correlation for $\overline{Nu}_V/\overline{Nu}_F$ (Equation (83)) Applied to Mechanical Vibrational Data of Reference 25	140
40.	Vertical Infinite Fringe Interferograms for $\frac{A}{D} = 0.12$, $Re_A = 136$, and $Gr = 44820$	143
41.	Horizontal Infinite Fringe Interferograms for $\frac{A}{D} = 0.52$, $Re_A = 148$, and $Gr = 44025$	146
42.	Vertical Infinite Fringe Interferograms for $\frac{A}{D} = 0.52$, $Re_A = 148$, and $Gr = 44025$	147
43.	Horizontal Infinite Fringe Interferograms for $\frac{A}{D} = 1.77$, $Re_A = 147$, and $Gr = 46183$	149
44.	Vertical Infinite Fringe Interferograms for $\frac{A}{D} = 0.51$, $Re_A = 586$, and $Gr = 44989$	151
45.	Vertical Infinite Fringe Interferograms for $\frac{A}{D} = 1.78$, $Re_A = 586$, and $Gr = 45643$	154
46.	Schematic Diagram of the Effective Index of Refraction	167
47.	Division of a Single Ray Into Two Components	169
48.	Schematic Diagram of Ray Division by Wollaston Prism	170

Figure		Page
49.	Schematic Diagram of a Converging Beam Entering the Wollaston Prism.	175
50.	Incident Ray Entering Wollaston Prism X Distance Above Center Line.	177
51.	Orientation of Plane of Polarization of Analyzer	182
52.	Curvilinear Coordinate System.	207
53.	Schematic Diagram of a Refracted Ray Passing Through a Thermal Boundary Layer	228

NOMENCLATURE

Symbol	Definition	Units
	(a) Latin Letter and Composite Symbols	
a	constant used in correlation analysis	dimensionless
a_f	fringe number at center of cylinder	dimensionless
A	amplitude of vibration	ft
A_1	constant used in correlation analysis	dimensionless
A_2	constant used in correlation analysis	dimensionless
A_3	constant used in correlation analysis	dimensionless
A_4	constant used in correlation analysis	dimensionless
A_5	constant used in correlation analysis	dimensionless
A_{cov}	cross sectional area of covering	ft^2
A_{end}	total exposed area of both cylinder ends	ft^2
A_{eq}	equivalent cross sectional area	ft^2
A_{ij}	rectangular matrix of constants used in correlation analysis	dimensionless
A_j	column matrix of constants used in correlation analysis	dimensionless
A_{ny}	cross sectional area of nylon support	ft^2
A_{sur}	cylinder surface area	ft^2
A_{wire}	cross sectional area of wire	ft^2
b	constant used in correlation analysis	dimensionless
b_o	quantity used in refraction error analysis	dimensionless

Symbol	Definition	Units
b_1	quantity used in refraction error analysis	dimensionless
b_2	quantity used in refraction error analysis	dimensionless
b_3	quantity used in refraction error analysis	dimensionless
b_f	radius of cylinder in fringes	dimensionless
B	constant used in correlation analysis	dimensionless
B_i	column matrix of constants used in correlation analysis	dimensionless
c_p	specific heat at constant pressure	Btu/lbm-°R
C	constant used in correlation analysis	dimensionless
$\overline{C}$	velocity of light in a vacuum	ft/sec
$\overline{C}_x$	velocity of ray x	ft/sec
$(\overline{C}_x)_1$	velocity of ray x in first half of WP1	ft/sec
$(\overline{C}_x)_2$	velocity of ray x in second half of WP1	ft/sec
$\overline{C}_y$	velocity of ray y	ft/sec
$(\overline{C}_y)_1$	velocity of ray y in first half of WP1	ft/sec
$(\overline{C}_y)_2$	velocity of ray y in second half of WP1	ft/sec
C_{cor}	correction factor	dimensionless
d	constant used in correlation equation	dimensionless
d_w	distance between ray x and ray y as they leave WP1	ft
D	diameter of test cylinder	ft
D_{proj}	projected diameter of test cylinder	ft
D_{pb}	distance from right side of cylinder to plumb bob	ft

Symbol	Definition	Units
e	error	dimensionless
e_{approx}	error involved in the approximation in Equation (19)	dimensionless
e_c	constant used in correlation analysis	dimensionless
e_{end}	error due to end effects	dimensionless
e_{fs}	fringe shift reading error	dimensionless
$\bar{e}_{fs}$	average fringe shift reading error	dimensionless
e_{ref}	error due to refraction	dimensionless
e_α	error in using Equation (106) for the calculation of α	dimensionless
E	electric vector	volts/m
E_x	electric vector in the x direction	volts/m
E_y	electric vector in the y direction	volts/m
f	frequency of oscillation	cycles/sec
F	constant in Equations (6) and (117)	1/ft
F_c	parameter used in correlation analysis	dimensionless
g	distance between WP1 and spherical mirror	ft
g_o	gravitational constant	ft/sec^2
G	Gladstone-Dale coefficient	ft^3/lbm
Gr	Grashof number	dimensionless
h	convective heat-transfer coefficient	Btu/hr ft^2 °R
h_2	convective heat-transfer coefficient of section 2	Btu/hr ft^2 °R
$\bar{h}$	average convective heat-transfer coefficient	Btu/hr ft^2 °R
$\bar{h}_{bal}$	average convective heat-transfer coefficient obtained from energy balance	Btu/hr ft^2 °R

Symbol	Definition	Units
h_{end}	convective heat-transfer coefficient of cylinder ends	Btu/hr ft^2°R
h(x)	local convective heat-transfer coefficient as a function of x	Btu/hr ft^2°R
h(θ)	local convective heat-transfer coefficient as a function of θ	Btu/hr ft^2°R
i	integer	dimensionless
I	intensity of light	watts/m^2
j	integer	dimensionless
J	number of thermocouples	dimensionless
k	thermal conductivity	Btu/hr ft°R
k_{cov}	thermal conductivity of covering material	Btu/hr ft°R
k_{eq}	equivalent thermal conductivity	Btu/hr ft°R
k_{ny}	thermal conductivity of nylon	Btu/hr ft°R
k_s	thermal conductivity of air at surface temperature	Btu/hr ft°R
k_{wire}	thermal conductivity of wire	Btu/hr ft°R
K	constant in Equations (7) and (128)	watts/m^2
K_1	constant in Equation (23)	ft^3/lbm
ℓ	optical path	ft
$\Delta\ell$	change in optical path	ft
$\Delta\ell_H$	actual change in optical path	ft
$\Delta\ell_{ref}$	change in optical path due to refraction	ft
$\Delta\ell_{ref_{ray\ x}}$	change in optical path of ray x due to refraction	ft
$\Delta\ell_{ref_{ray\ y}}$	change in optical path of ray y due to refraction	ft

Symbol	Definition	Units
L	length of heated test object in the direction of light propagation	ft
L_f	distance from end of test object that is closest to camera to the object plane	ft
m	number of fringe shifts	dimensionless
$m(\theta)$	number of fringe shifts at θ	dimensionless
m_s	number of fringe shifts at surface	dimensionless
m_ρ	measured number of fringe shifts due to horizontal gradients	dimensionless
m_{ρ_A}	actual number of fringe shifts due to horizontal gradients	dimensionless
m_η	measured number of fringe shifts due to vertical gradients	dimensionless
m_{η_A}	actual number of fringe shifts due to vertical gradients	dimensionless
M	magnification	dimensionless
$\overline{M}$	number of simultaneous equations	dimensionless
M_1	measurement of distance used in calculating b_f	ft
M_2	measurement of distance used in calculating b_f	ft
M_3	measurement of distance used in calculating a_f	ft
M_4	measurement of distance used in calculating a_f	ft
M_5	measurement of distance used in calculating b_f	ft
M_6	measurement of distance used in calculating b_f	ft
n	index of refraction	dimensionless

Symbol	Definition	Units
n_e	extraordinary index of refraction of birefringent material	dimensionless
n_{eff}	effective index of refraction	dimensionless
n_o	ordinary index of refraction of birefringent material	dimensionless
$n_{ray\ x}$	index of refraction of medium through which ray x passes	dimensionless
$n_{ray\ y}$	index of refraction of medium through which ray y passes	dimensionless
n_{ref}	reference index of refraction	dimensionless
n_∞	index of refraction of surroundings	dimensionless
$\overline{N}$	number of unknowns	dimensionless
$N_u(\theta)$	undeflected fringe number at angular position θ	dimensionless
$N_d(\theta)$	undeflected fringe number at angular position θ	dimensionless
Nu	Nusselt number	dimensionless
$\overline{Nu}_{bal}$	average Nusselt number calculated from energy balance	dimensionless
$Nu_F(\theta)$	local Nusselt number of free convective test	dimensionless
$\overline{Nu}_F$	average Nusselt number of free convective test	dimensionless
$\overline{Nu}_{osc}$	$\overline{Nu}_v - \overline{Nu}_F$	dimensionless
$Nu_v(\theta,\psi)$	instantaneous, local Nusselt number	dimensionless
$Nu_v(\psi)$	instantaneous, average Nusselt number	dimensionless
$Nu_v(\theta)$	average, local Nusselt number	dimensionless
$\overline{Nu}_v$	average Nusselt number of vibratory test	dimensionless
p	an odd integer	dimensionless

Symbol	Definition	Units
P	absolute atmospheric pressure	lbf/in^2
P_{vap}	partial pressure of water vapor	lbf/in^2
Pr	Prandtl number	dimensionless
q(y)	heat flux from the surface of body	Btu/hr ft^2
q_1	heat flux in section 1	Btu/hr ft^2
q_2	heat flux in section 2	Btu/hr ft^2
q_{conv}	heat flux due to convection	Btu/hr ft^2
q_{rad}	heat flux due to radiation	Btu/hr ft^2
Q	number of points in polynomial fit	dimensionless
Q_{cond}	rate of heat loss due to conduction	Btu/hr
Q_{conv}	rate of heat loss due to convection from cylinder ends	Btu/hr
Q_{el}	rate of heat loss through electrical leads	Btu/hr
Q_{input}	total rate of energy input to the cylinder	Btu/hr
Q_{loss}	total rate of heat loss from cylinder	Btu/hr
Q_p	number of ψ positions analyzed	dimensionless
Q_{rad}	rate of heat loss due to radiation	Btu/hr
Q_{sur}	rate of heat loss from cylinder surface by convection	Btu/hr
Q_{tc}	rate of heat loss through thermocouple leads	Btu/hr
r	coordinate in radial direction	ft
$\bar{r}_i$	column matrix of residues	dimensionless
ray e	extraordinary ray	dimensionless
ray o	ordinary ray	dimensionless

Symbol	Definition	Units
ray x	ray associated with electric vector E_x	dimensionless
ray y	ray associated with electric vector E_y	dimensionless
R	cylinder radius	ft
R_a	gas constant for air	ft-lbf/lbm-°R
Re	Reynolds number	dimensionless
Re_A	average Reynolds number	dimensionless
Re_{freq}	frequency Reynolds number	dimensionless
$Re_v(\psi)$	instantaneous Reynolds number based on instantaneous speed of cylinder	dimensionless
Re_{osc}	oscillatory Reynolds number	dimensionless
Re_s	streaming Reynolds number	dimensionless
S	sum of squares of the residues	dimensionless
(SPL)	sound pressure level	db
(sq)	quantity used in expression for e_{end}	dimensionless
t	thickness of Wollaston prism	ft
T	absolute temperature	°R
T_1	absolute temperature in section 1	°R
T_2	absolute temperature in section 2	°R
T_s	absolute temperature of cylinder surface	°R
T_t	absolute temperature at tip end of support	°R
T_{wire}	absolute temperature of wire	°R
$(T_{wire})_1$	absolute temperature of wire in section 1	°R
$(T_{wire})_2$	absolute temperature of wire in section 2	°R
T_∞	absolute temperature of surroundings	°R
u	velocity in x_d direction	ft/sec

Symbol	Definition	Units
U	velocity outside the boundary layer in x_d direction	ft/sec
v	velocity in y_d direction	ft/sec
w_w	coordinate perpendicular to surface of test object	ft
W	distance from center of Wollaston prism	ft
WP1	Wollaston prism 1	dimensionless
WP2	Wollaston prism 2	dimensionless
WP3	Wollaston prism 3	dimensionless
x	coordinate in vertical direction	ft
x_d	radial coordinate in curvilinear coordinate system	ft
$\bar{x}_d$	dimensionless radial coordinate in curvilinear coordinate system	dimensionless
x_s	coordinate in the direction in which gradient is measured	ft
Δx_s	separation distance between ray x and ray y in test section	ft
X_1	unknown in correlation analysis	dimensionless
X_2	unknown in correlation analysis	dimensionless
X_3	unknown in correlation analysis	dimensionless
X_4	unknown in correlation analysis	dimensionless
X_5	unknown in correlation analysis	dimensionless
X_j	column matrix of unknowns in correlation analysis	dimensionless
X_n	ratio of $\overline{Nu}_V$ to $\overline{Nu}_F$	dimensionless
y	coordinate in horizontal direction perpendicular to direction of light propagation	ft

Symbol	Definition	Units
y_d	tangential coordinate in curvilinear coordinate system	ft
$\bar{y}_d$	dimensionless coordinate in curvilinear coordinate system	dimensionless
Y	instantaneous wave displacement	volts/m
Y_{result}	resultant wave displacement	volts/m
Y_x	instantaneous wave displacement of ray x	volts/m
Y_y	instantaneous wave displacement of ray y	volts/m
z	coordinate in direction of light propagation	ft
z_c	constant used in correlational analysis	dimensionless
Z	compressibility factor of air	dimensionless

(b) Greek Letter and Composite Symbols

α	total angle of divergence between ray x and ray y as they leave WP1	degrees
α_1	angle of divergence between ray y and z direction as ray y leaves WP1	degrees
α_2	angle of divergence between ray x and z direction as ray x leaves WP1	degrees
α_D	parameter used in analysis in Appendix G	dimensionless
α_w	parameter used in refraction error analysis	dimensionless
α_ξ	total angle of divergence between ray x and ray y as they leave WP1 when rays enter at angle ξ from normal to prism surface	degrees
β	coefficient of thermal expansion $(-\frac{1}{\rho}[\frac{\partial \rho}{\partial T}]_p)$	$^\circ R^{-1}$

Symbol	Definition	Units
γ_1	angle between incident direction of ray y and normal to back side of WP1	degrees
γ_2	angle between incident direction of ray x and normal on back side of WP1	degrees
γ_D	parameter used in analysis in Appendix G	dimensionless
γ_R	angle between radial and horizontal directions	degrees
γ_T	angle between tangential and horizontal directions	degrees
δ	boundary layer thickness	ft
δ_{ac}	a.c. boundary layer thickness	ft
ε_{ny}	emissivity of nylon	dimensionless
ε_p	permittivity of medium	farad/m
ε_{sur}	emissivity of cylinder surface	dimensionless
ε_∞	emissivity of surroundings	dimensionless
ζ	coordinate in horizontal direction	ft
η	coordinate in vertical direction	ft
η_δ	coordinate perpendicular to heat-transferring surface	ft
θ	angular measurement around cylinder measured from the zero location at the geometric bottom of the cylinder	degrees
$\overline{\theta}_s$	$(T_s-T_\infty)/T_\infty$	dimensionless
θ_T	$T-T_\infty$	°R
$\overline{\theta}_T$	$(T-T_\infty)/(T_s-T_\infty)$	dimensionless
$(\theta_T)_s$	T_s-T_∞	°R

Symbol	Definition	Units
Θ	wedge angle of Wollaston prism	degrees
Λ	angle between the electric vector associated with ray e and the optic axes	degrees
λ	wavelength of light	ft
λ_D	angle used in the analysis in Appendix G	dimensionless
μ_p	permeability of medium	henry/m
μ_a	absolute viscosity of air	lbm/(ft sec)
ν	kinematic viscosity	ft^2/sec
ξ	angle between incident ray and normal on front surface of WP1	degrees
ξ_{max}	maximum angle between incident rays and normal on front surface of WP1	degrees
ξ_1	angle between direction of ray y and normal on Wollaston prism interface	degrees
ξ_2	angle between direction of ray x and normal on Wollaston prism interface	degrees
π	constant (3.1416)	dimensionless
ρ	density	lbm/ft^3
σ	Stefan-Boltzmann constant	$Btu/hr\ ft^2{}^\circ R^4$
τ	time	hr
$\bar{\tau}$	dimensionless time	dimensionless
τ_x	time required for ray x to travel through Wollaston prism	hr
τ_y	time required for ray y to travel through Wollaston prism	hr
ϕ	phase	dimensionless
ϕ_x	phase of ray x	dimensionless

Symbol	Definition	Units
ϕ_y	phase of ray y	dimensionless
$\Delta\phi_{total}$	total phase difference	dimensionless
$\Delta\phi_{ts}$	phase difference introduced in test section	dimensionless
$\Delta\phi_{WP3}$	phase difference produced by WP3	dimensionless
Φ	function	dimensionless
Φ_1	correlation function defined in Equation (85)	dimensionless
ψ	angular position of cylinder measured from left extreme position	degrees
Ψ	stream function	ft^2/sec
$\overline{\Psi}$	dimensionless stream function	dimensionless
ω	circular frequency	1/sec

SUMMARY

This thesis describes the application of a differential interferometer to the measurement of instantaneous, local heat-transfer rates. There were two objectives of this investigation. Since the application of the differential interferometer to heat-transfer problems has been quite limited, the first objective was to determine the potential of the interferometer when applied to the measurement of heat-transfer rates. The second objective was to investigate the effect of horizontal, mechanical vibration on the heat-transfer rate from a heated, horizontal, isothermal cylinder to air in free convection.

The potential of the differential interferometer was investigated by applying this instrument to heat-transfer measurements both for simple steady state problems and a complex transient problem. Measurements of local steady state free convective heat-transfer coefficients over a vertical flat plate were made. The results of these measurements were within five per cent of theoretical results. A second steady state application of the differential interferometer was the measurement of local heat-transfer rates from a stationary, heated, isothermal cylinder losing heat to air by free convection. Excluding the region near the top of the cylinder where heat-transfer rates are small, the results of these

tests varied from the experimental values of a previous investigation by no more than three per cent. Reproducibility was verified by repeating steady state measurements several times and comparing the results.

The transient problem studied was an investigation of the effect of horizontal, mechanical vibration on the heat-transfer rate from a heated, horizontal, isothermal cylinder to air in free convection. The ranges of the dimensionless parameters investigated were: Grashof numbers from 2.45×10^4 to 7.60×10^4, ratios of amplitude of vibration to diameter of cylinder from 0 to 1.78, and average Reynolds numbers from 0 to 660. Instantaneous, local Nusselt numbers (local values at one instant of time) were measured throughout the cycle of oscillation by using a differential interferometer. Instantaneous, average Nusselt numbers (average values at one instant of time) were calculated for all the vibratory tests by averaging the instantaneous, local Nusselt numbers over the entire cylinder surface. Average, local Nusselt numbers (local values averaged over time) were calculated by averaging the instantaneous, local values over a cycle of oscillation. Finally, an overall average Nusselt number was calculated by averaging the instantaneous, average Nusselt numbers over a cycle of oscillation. A check of the interferometric measurement of the overall average Nusselt number was made by writing an energy balance on the cylinder. The average discrepancy between the values for the two methods

was 3.8 per cent. Two vibratory tests were repeated, and the reproducibility of the results was 2.6 per cent.

A successful correlation of the overall average Nusselt number was achieved as a function of three dimensionless parameters: the Grashof number, the ratio of the amplitude of vibration to cylinder diameter, and the Reynolds number. The average difference between the values from the correlation and the experimental values was 6 per cent.

The primary conclusions of the investigation were: the differential interferometer is an instrument that is easily adapted to heat-transfer problems and provides an accurate and reproducible measurement of heat-transfer rates for both steady state and transient problems as well as an excellent method for flow visualization of thermal boundary layers; vibration can significantly affect the heat transfer from a horizontal isothermal cylinder (increases up to 1400 per cent in the instantaneous, local Nusselt number were measured), and its effect varies significantly with the parameters: the Grashof number, the ratio of amplitude of oscillation to cylinder diameter, and the Reynolds number.

CHAPTER I

INTRODUCTION

The need for more efficient thermal systems stemming from industrial and space program applications have stimulated an interest in methods to augment heat transfer. One method of augmentation that has been investigated has involved the use of vibration. Both acoustical and mechanical vibrations have been used in cases involving both free and forced convection. The test body most often studied has been a heated horizontal cylinder vibrating either horizontally or vertically.

This dissertation is concerned with the effect of horizontal, transverse, mechanical vibrations on the heat-transfer rate from an isothermal cylinder to air in free convection. Most of the investigations in this area have been limited to the measurement of average heat-transfer coefficients. In fact, there does not appear to be any measurements of local heat-transfer coefficients for mechanical vibrations. A very limited number of average, local heat-transfer measurements (local values averaged over time) have been made for acoustic vibration. No measurement of instantaneous, local heat-transfer coefficients (local values at one instant of time) have been reported for either acoustical

or mechanical vibration. The lack of instantaneous, local data may be due to the absence of a good technique of measurement.

A differential interferometer was used in this study to obtain instantaneous, local heat-transfer data. The differential interferometer is relatively new and has not previously been used for the measurement of heat-transfer coefficients. Other optical instruments such as the Mach-Zehnder interferometer have been used extensively for heat-transfer measurements; however, the differential interferometer possesses unique capabilities for measuring local heat-transfer coefficients under rapidly changing transient conditions. The differential interferometer produces fringe shifts proportional to local temperature gradients. As a result, local heat-transfer coefficients can be readily measured with this device.

The purpose of this investigation has been twofold. Since the application of the differential interferometer to heat-transfer problems has been limited, one objective of this investigation has been to determine the potential of the differential interferometer when applied to heat-transfer problems. The second objective has been to investigate the effect of horizontal, mechanical vibration on the heat-transfer rate from a heated isothermal cylinder to air by free convection. Instantaneous, local heat-transfer

coefficients have been measured throughout the cycle of oscillation by using a differential interferometer.

CHAPTER II

LITERATURE SURVEY

Introduction

Over the past few years, there have been many investigations on the effect of vibration on heat-transfer rates. Some investigators have reported large increases in heat-transfer rates with vibration while others have reported little or no effect. In some cases, decreases in heat-transfer rates have been reported. The variation in results are not surprising due to the large number of oscillatory and convective variables involved.

Two types of vibrations can be distinguished. These are mechanical vibrations and acoustical vibrations. Mechanical vibrations are vibrations of the surface relative to the surrounding fluid. Acoustical vibrations are vibrations applied to a fluid and directed toward the heat-transferring surface.

In the discussion of the various papers, the following parameters are most often used: the amplitude of vibration A; the frequency of oscillation f; the product of amplitude and frequency which is called vibrational intensity Af; the ratio of amplitude of vibration to the diameter of the cylinder $\frac{A}{D}$; the Reynolds number Re; the Grashof number Gr;

and the temperature difference between the cylinder and the surroundings ΔT.

Most of the investigators have reported a critical vibrational parameter below which the heat transfer is unaffected by oscillation. In some reports this vibrational parameter has been the vibrational intensity Af while in other reports this parameter has been the Reynolds number.

The vibrational parameter $\frac{A}{D}$ gives an indication of the type of process to expect in the vicinity of the cylinder. For $\frac{A}{D} >> 1$, a quasi-steady type flow exists. Three regions of flow are found: 1.) a region where free convection dominates; 2.) a transitional region of both free and forced convection; and 3.) a region where forced convection dominates.

For $\frac{A}{D} << 1$, there is no periodic displacement of fluid across the cylinder to effect a net increase in enthalpy transport. In this case, natural convection dominates until the critical vibrational intensity is reached. Then, a type of coupling between streaming currents due to vibration and natural convective currents occurs which causes a net increase in enthalpy transport. The nature of the phenomenon occurring to produce this increase in enthalpy transport has stimulated several hypotheses explaining this phenomenon. Fand [1][1] discusses Westervelt's hypothesis [2], Sprott, Holman, and Durand's hypothesis [3], and Fand and Kaye's hypothesis [4].

[1]Numbers in brackets refer to the Bibliography at the end of the dissertation.

All of these hypotheses attempt to explain the observed fact that intense sound significantly increases the rate of heat transfer from horizontal cylinders. Fand states the first two hypotheses fail since experimental data contradict them. Fand and Kaye's hypothesis states that the sudden increases in heat-transfer rates are caused by thermoacoustic streaming, a phenomenon that is characterized by the development of two vortices around the cylinder. The vortex flow begins to form when the sound pressure level (SPL) reaches a critical value and becomes fully developed at a higher sound pressure level. This level is called the SPL for fully developed vortex flow. Further increases in the sound pressure level cause the vortices to increase in size, but the basic character of the flow remains unaltered. This flow results from the interaction between the thermal and acoustic velocity and temperature fields. Fand states that experimental evidence supports this explanation. It was concluded that the differential equations describing the coupling between vibrations and free convection are nonlinear, and for such a system it is invalid to regard the simple superposition of the uncoupled effects as the solution to the coupled system. Furthermore, Fand states the ratio of amplitude to diameter $\frac{A}{D}$ is an important parameter and probably can be used to explain the difference in the experimental results of various investigations.

Richardson has authored several papers [5-12] attempting to analytically explain the effects of acoustical and

mechanical vibration on heat transfer from horizontal cylinders. Most of the analyses are for sound in the absence of gravitational fields. Since no tests have been performed in the absence of gravity, attempts to check the analyses have been limited to extrapolation from cases when the ratio Gr/Re^2 approaches zero. Theoretical attempts [7] to combine the effects of vibration and natural convection by simple superposition proved to be unsatisfactory. Computer solutions [10] of the simplified differential equations for coupled vibration and natural convection were made for a few special cases. Comparison with experimental data from previous investigations [5, 6, 12] showed qualitative agreement but was quantitatively incorrect. This inconsistency was explained through the fact that several assumptions used in a computer solution were not sufficiently close to experimental conditions.

For intermediate ratios of vibrational amplitude to cylinder diameter, $\frac{A}{D}$, in the neighborhood of unity, theoretical results are scarce.

Average Heat-Transfer Measurements For Mechanical Vibration

Over the last thirty years, there have been several investigations on the effect of mechanical vibrations on the heat-transfer rate from wires and cylinders in free convection. As early as 1923, Richards [13] reported that the thermal resistance of an oscillating hot wire was a strong

function of both amplitude and frequency of vibration. In 1928, Maxwell [14] noted that the "escape of heat" was increased by 25 per cent when small (0.0006 inches in diameter), platinum wires were vibrated at a frequency of 96 cycles per second and an amplitude of 0.06 inches.

In 1938, Martinelli and Boelter [15] investigated the effect of sinusoidal vibration in the vertical direction on heat transfer by free convection from a horizontal cylinder to water. The cylinder was 0.75 inches in diameter and approximately 12.63 inches long, and the ratios of amplitude to diameter ranged from 0 to 0.133. For the range of parameters investigated, a critical value of the Reynolds number of approximately 1000 was measured. Above the critical Reynolds number, the rate of heat transfer increases with increasing Reynolds number, and increases in the heat-transfer coefficient of up to 400 per cent were observed. The data were correlated in an equation containing the following parameters: Nusselt number, Reynolds number, and the product of the Grashof number and the Prandtl number. An analytical solution based on an oscillating vertical flat plate was presented. Considering the number of assumptions in the solution, the agreement between the experimental and analytical results was fair.

In 1949, Mason and Boelter [16] extended the work of Martinelli and Boelter. Three cylinders having diameters of 0.375, 0.75, and 1.25 inches were used, and the ratios of

amplitude to diameter ranged from 0 to 0.693. Increases in the heat-transfer rate of more than thirty fold for a Grashof-Prandtl product of 10^5 and of more than eighteen fold for a Grashof-Prandtl product of 10^6 were reported. A critical Reynolds number of approximately 1000 was determined. Above the critical Reynolds number, the heat-transfer rate increased with increasing Reynolds number. At very high Reynolds number, the increase in the heat-transfer rate with increasing Reynolds number was much less than at Reynolds numbers just slightly greater than the critical value. The results of the tests were plotted in terms of the Nusselt number, the Grashof-Prandtl product, and the Reynolds number. Unfortunately, the accuracy of these results are in doubt since Boelter later indicated that results obtained from a check on some of the experimental data did not agree with the original data.

In 1954, Lemlich [17, 18] investigated the effect of vibration on natural convective heat transfer in air from electrically heated wires of three different diameters (0.0253, 0.0396, and 0.0810 inches). The ratios of amplitude to diameter ranged from 0.34 to 4.6. Both horizontal and vertical oscillations were studied. Correlation equations for the data were presented. Lemlich concluded from his results that: 1.) the heat-transfer coefficient increased with either an increase in amplitude or frequency, and increases up to 300 per cent were obtained; 2.) the direction of vibration had no effect in the range of variables investigated. This

observation was explained through the concept of a stretched film that surrounds the entire path of vibration.

In 1958, Hutton [19] studied the effect of transverse vibrations on the heat-transfer rate from a horizontal cylinder in free convection. The cylinder was 1.5 inches in diameter and 10 inches long. Small ratios of amplitude to diameter (0.00143 to 0.0643) were investigated. Hutton presented his results in the form of graphs of the heat-transfer coefficient plotted as a function of frequency. He concluded that there was some critical frequency below which the heat-transfer coefficient is unaffected by vibration. This critical frequency is a function of amplitude and decreases with increasing amplitude. The maximum increase in the heat-transfer coefficient found by Hutton was 25 per cent. A Mach-Zehnder interferometer was employed to calculate the average heat-transfer coefficient. Although the interferograms could have been used to calculate local values of the heat-transfer coefficient, an averaging technique was used to measure the average heat-transfer coefficient. On reviewing reference 19, an error was found in Hutton's method of calculating average temperature gradients. This error could have introduced a significant error in the calculation of the heat-transfer coefficient. Also, the average was taken over only one half of the cylinder and at only two points of the cycle through which the cylinder oscillates. As a result, the accuracy of Hutton's data is questionable.

In 1960, Eisele [20] studied the effect of horizontal transverse vibrations on the heat-transfer rate from heated horizontal cylinders in free convective flow. Four cylinders having diameters of 1.5, 0.75, 0.25, and 0.085 inches were used. The large diameter cylinders were tested at small ratios of amplitude to diameter (0.008 to 0.0427 and 0.041 to 0.089, respectively) while the small diameter cylinders were tested at moderate ratios of amplitude to diameter (0.10 to 0.21 and 0.49 to 0.74, respectively). Eisele presented his results in the form of graphs of the ratio of Nusselt number with vibration to Nusselt number without vibration at the same total energy input to the cylinder plotted as a function of the intensity of vibration, Af. Eisele concluded from his results that: 1.) the critical vibrational intensity was approximately 1 inch per second and was independent of cylinder diameter; 2.) waviness in the boundary layer occurred only at vibrational intensities considerably greater than the critical vibrational intensity; and 3.) for small tubes and wires vibrating at intensities greater than 3.5 inches per second, the boundary layer stretched to enclose the vibratory motion. Similar to Hutton, Eisele employed a Mach-Zehnder interferometer to calculate the average heat-transfer coefficient. Eisele used the same averaging technique as Hutton which could have introduced errors in his results. Eisele stated that the accuracy in measuring the heat-transfer coefficient for the 0.25 and 0.085 inch diameter cylinders was

very poor due to difficulty in measuring fringe spaces on the interferograms.

In 1960, Teleki, Fand, and Kaye [21] made an experimental investigation on the influence of vertical mechanical vibration on free convective heat transfer from a heated horizontal 0.875 inch diameter cylinder to air. The tests were conducted at ratios of amplitude to diameters of 0.011 to 0.18. The conclusions drawn from the results of this investigation were: 1.) for the same temperature potential, the heat-transfer coefficient was observed to increase in the presence of large vibrational intensities by as much as 200 per cent; 2.) a critical vibrational intensity of approximately 2.4 inches per second existed; 3.) for values of the vibrational intensity between 2.4 inches per second and 10.8 inches per second, the heat-transfer coefficient increased with increasing values of vibrational intensity. For values greater than 10.8 inches per second, the heat-transfer coefficient increased less rapidly; and 4.) the effect of vibration on the heat-transfer coefficient was greater as the temperature difference was decreased.

In 1961, Fand and Kaye [22] experimentally investigated the influence of vertical mechanically induced simple harmonic vibration upon the rate of heat transfer from a heated horizontal cylinder to air. The cylinder was 0.875 inches in diameter, and the ratios of amplitude to diameter ranged from 0 to 0.18. The results of the investigation indicated that

the sole controlling vibrational variable was the intensity of vibration. A critical intensity of vibration, approximately 3.6 inches per second, was observed. A flow visualization study employing smoke indicated that the mechanism which caused the observed increases in the heat transfer was vibrationally induced turbulence. Fand and Kaye noted that the type of turbulent boundary-layer flow observed differed radically from the vortex type of flow observed near a heated horizontal cylinder subjected to acoustically induced transverse horizontal vibrations.

In 1961, James [23] investigated the effect of horizontal transverse vibrations on the heat-transfer rate from cylinders in air. Three cylinders having diameters of 0.085, 0.25, and 0.75 inches were used. James concluded from the results of his investigation that: 1.) the diameter of the cylinder influenced the per cent increase in heat transfer; and 2.) the increment of temperature difference had an influence on the heat-transfer rate, but its influence decreased as the vibrational intensity increased.

In 1962, Deaver, Penney and Jefferson [24] made an investigation of the effect of low-frequency, large-amplitude oscillations ($6.43 \leq \frac{A}{D} \leq 197$) of a small (0.007 inches in diameter) wire on free convection in water. The harmonic motion of the wire was in a vertical plane. Regions of free, mixed, and forced convection were found. Empirical equations were formulated for each of these regions. At high vibrational

Reynolds numbers based on the average speed of the cylinder, the vibrational heat-transfer rates agreed well with those of forced convection at the same Reynolds number. For low Reynolds numbers, the heat-transfer rate was independent of the Reynolds number.

In 1962, Fand and Peebles [25] made a comparison of the influence of horizontal mechanical vibration and acoustical vibration on free convection in air from a horizontal cylinder with a 0.875 inch diameter. The ratio of amplitude to diameter ranged from 0.028 to 0.15. The amount of data for the two types of vibration was limited; however, Fand and Peebles concluded: 1.) the critical intensity was 4.32 inches per second, and the vertical intensity was not a function of frequency; and 2.) for values of vibrational intensity greater than 8.4 inches per second, the same correlation equation can be used to compute the rate of heat transfer from a heated horizontal cylinder subjected to either acoustically or mechanically induced horizontal transverse oscillations.

In 1962, Russ [26] studied the effect of horizontal transverse vibrations on the heat-transfer rate from heated, horizontal cylinders in free convection. Three cylinders having diameters of 0.085, 0.25, and 0.75 inches were used. The ranges of the ratios of amplitude to diameter for the three cylinders were 0.167 to 3.912, 0.050 to 1.130, and 0.387 to 0.2053, respectively. Russ concluded from his results that: 1.) the diameter of the cylinder had an appreciable effect on

the heat-transfer rate; 2.) at high vibrational intensities, the increment of temperature difference had no appreciable effect on the heat-transfer rate; 3.) for a given test cylinder, the only important parameter was the vibrational intensity; 4.) for high vibrational intensities, increases in the heat-transfer rate may exceed 300 per cent; 5.) the heat-transfer rate as a function of the vibrational intensity was very complex, and no simple analogy to that of forced convection existed for the range of parameters investigated; and 6.) the boundary-layer changed considerably as the vibrational intensity was increased, and for high vibrational intensities, the boundary-layer shape approached that observed in forced convection. Russ presented the results of his tests in the form of graphs with Log $(\overline{Nu}_V/Pr^{0.3})$ plotted as a function of Log Re_A. Nearly all of his tests were conducted at different Grashof numbers, but the correlation did not include the Grashof number.

In 1964, Neely [27] made an investigation to determine the effect of diameter, temperature difference, and vibrational intensity on the free convective heat-transfer rate from the surface of horizontal cylinders subjected to transverse horizontal vibrations. Two cylinders with diameters of 0.085 and 0.25 inches were used. Moderate ratios of amplitude to diameter (0.207 to 1.13 and 0.402 to 4.03, respectively) were investigated. Air was the medium employed. This investigation was at much higher vibrational intensities than had

been previously investigated. From his results, Neely concluded that: 1.) for vibrational intensities between 12 and 29 inches per second, the variation of the heat-transfer coefficient follows the forced convective curve; the slope of the curve was independent of the cylinder diameter; 2.) for a given cylinder diameter and vibrational intensity, the value of the heat-transfer coefficient was independent of the temperature difference for vibrational intensities between 12 and 29 inches per second and for the range of parameters studied; and 3.) the boundary layer was turbulent for vibrational intensities between 12 and 29 inches per second. Similar to Russ, Neely presented his results in the form of graphs with Log $(Nu_V/Pr^{0.3})$ plotted as a function of Log Re_A. Most of his tests were conducted at different Grashof numbers with the Grashof number decreasing with increasing vibrational intensity. No attempt was made to bring the Grashof number into his correlation.

In 1965, Lemlich and Rao [28] studied the effect of vertical transverse vibration from a 0.049 inch diameter horizontal cylinder. The ratios of amplitude to diameter ranged from 0.47 to 3.09. Water and aqueous glycerine were the two media used. Lemlich and Rao attempted to correlate their results along the data of Deaver [24], Lemlich [17], Fand and Kaye [22], and Lemlich and Levy [29]. A satisfactory correlation of the form

$$\frac{\overline{Nu}_V}{\overline{Nu}_F} = \Phi\left[\frac{Re_A\left(\frac{A}{D}\right)^{0.4} Pr^{0.6}}{(GrPr)^{0.26}}\right] \qquad (1)$$

was obtained when Deaver's data was omitted. Deaver's tests were conducted at much lower frequencies and higher $\frac{A}{D}$ than the tests of the other investigators. Lemlich and Rao concluded that vertical vibration in free convection to water or aqueous glycerine markedly increased the heat-transfer coefficient, sometimes up to ten fold, and increasing either amplitude or frequency increased the vibrational effect.

In 1966, Penney and Jefferson [30] conducted an investigation of the effect of low-frequency, large-amplitude ($15 \leq \frac{A}{D} \leq 150$), horizontal oscillations on free convection from a heated horizontal wire (0.008 inches in diameter) to water and ethylene glycol. A comparison was made between the data taken in this investigation and a previous investigation [24] of a horizontal wire oscillating in a vertical plane. For the free convective region, the two cases correlated closely; however, the vertically oscillating cylinder had higher heat-transfer rates in the forced convection dominated region. A correlation for both water and ethylene glycol on a single plot was unsuccessfully attempted by previously accepted methods ($\overline{Nu}_V/Pr^{0.3}$ plotted as a function of Re_A at a constant Gr Pr and $\overline{Nu}_V$ plotted as a function of Gr Pr at constant Re_A). A plot of $\overline{Nu}_V$ as a function of $Re_A\ Pr^{0.8}$ at

constant Gr Pr did successfully correlate both water and ethylene glycol data, but the plot failed to correlate data of previous investigators. Penney and Jefferson recommended that the ratio $\frac{A}{D}$ be included in future investigations.

In 1969, Thrasher and Schaetzle [31] reported on the measurement of instantaneous heat-transfer rates from wires that were oscillated by means of thermal contractions and expansions. Wires with diameters of 0.0031 and 0.008 inches were used, and large ratios of amplitude to diameter (up to 202) were studied. A temperature variation in the wire during oscillation resulted from internal resistance heating by an alternating current. Results were plotted in the form of Log $\overline{Nu}_v$ as a function of Log Re_A and correlation equations were presented. The following conclusions were drawn: 1.) a critical Reynolds number existed which divided the heat-transfer rates into free and forced convective regimes; 2.) the average heat-transfer rate for an oscillating wire was approximately 20 per cent less than the rate for steady state forced convection at the average Reynolds number of the oscillating wire; 3.) no significant difference existed in the average heat-transfer rates for oscillations in the vertical or horizontal planes; 4.) for Reynolds numbers below the critical value, the data exhibited the dominance of free convection which was approximately one and one-half times the steady state free convective rate; and 5.) above the critical Reynolds number, the instantaneous heat-transfer data had

approximately the same slope as those for steady state forced convection.

In 1971, Armaly and Madsen [32] experimentally studied the effect of large horizontal amplitude ($\frac{A}{D}$ up to 132.8) oscillations on heat transfer by natural convection in air. A platinum wire 0.01 inches in diameter was used in the investigation. The results of the study showed that an increase in either the amplitude or the frequency of the vibration will increase the heat transfer. The results of the tests could be predicted with reasonable accuracy by using the average wire velocity with an appropriate uniform forced convection relation.

This discussion has been limited to mechanical vibration of horizontal cylinders in free convection; however, numerous investigations have been made of mechanical vibration for other geometries and for forced flow conditions. Also, many investigations of the effect of acoustical vibrations have been reported. A survey of investigations in this area along with an extensive bibliography has been made by Bergles [33].

Local Heat-Transfer Measurements

Although many investigations of the effect of mechanical vibration on the heat-transfer rate from an isothermal horizontal cylinder to air in free convection have been made, all of these investigations have been limited to the measurement

of average heat-transfer coefficients. However, two groups of investigations have been made on the effect of acoustical vibration on the average, local heat-transfer rate from an isothermal, horizontal cylinder to air in free convection. The local heat-transfer coefficients obtained in these investigations were averaged over time; and therefore, they are referred to as average local heat-transfer coefficients. The term instantaneous, local heat-transfer coefficient is used to refer to local heat-transfer coefficients that were measured at one instant of time and are considered to be instantaneous values. Since these investigations were made for acoustical vibrations, they are limited to small ratios of amplitude to diameter which are approximately two orders of magnitude smaller than those reported in this study. Therefore, the results of these investigations can not be expected to compare closely with the results reported here.

In 1962, Fand, Roos, Cheng, and Kaye [12] reported the measurement of average, local heat-transfer coefficients around the circumference of a heated horizontal cylinder in the presence of a strong stationary sound field directed horizontally toward the cylinder. This investigation was limited to one test for a constant temperature difference of 169 degrees F with and without sound and one test for a constant energy input to the cylinder with and without sound. Both sound tests were conducted at a frequency of 1500 cycles per second, an amplitude to diameter ratio of 0.0076, and a

sound pressure level of 146 db which corresponds to an Af product of 8.58 inches per second. The sound pressure level was of a magnitude considered necessary for fully developed thermoacoustic streaming. The tests were performed with a segmented cylinder having a diameter of 0.75 inches. The test segment from which average, local heat-transfer coefficients were obtained subtended an arc of 30 degrees of the cylinder. Local heat-transfer coefficients were obtained by utilizing the symmetry of the system and by rotating the cylinder about its axis in 15 degree increments of the base circle. The assumption was made that the heat-transfer coefficients approximated the local values at the center of the arc. The largest source of error was reported to be due to the conduction from the test segment of the cylinder to the guard section. The conductive loss was estimated to have introduced an error ranging from 2 to 25 per cent depending on the magnitude of the heat-transfer coefficient. When polar plots of the heat-transfer results were made, figure 8-shaped curves were obtained for both tests. The results showed that the sound field caused large percentage increases in the heat-transfer coefficient on the lower and upper portions of the cylinder, but at 97 degrees from the lower stagnation point (the geometric bottom of the cylinder), the local heat-transfer coefficient was reduced. For the constant temperature difference case, the percentage increases in the average, local heat-transfer coefficient at 0 and 180 degrees from the

lower stagnation point were 250 and 1200 per cent, respectively. Flow visualization using smoke as the indicating medium was used along with the polar plots of the heat-transfer coefficient in an attempt to explain the phenomenon occurring. The conclusion was drawn that the surface of the heated cylinder could be subdivided into two regions that had different boundary-layer flow characteristics. The lower region of the cylinder (0 to 97 degrees from the lower stagnation point) corresponded to a region of laminar boundary-layer flow. The upper region (97 to 180 degrees from the lower stagnation point) corresponded to a region of oscillating vortex flow. The reasons for the development of vortex flow in the upper regions of the cylinder were not understood, but it was clear that this vortex motion could increase the heat-transfer rate. The increase in the heat-transfer coefficient in the lower regions of the cylinder were attributed to two reasons. One reason was an increase in laminar boundary-layer velocities which caused a reduction in the boundary-layer thickness. The second reason was a modification of the boundary-layer temperature profile due to acoustically induced oscillations within the laminar boundary layer. The important conclusion was drawn that simple superposition of acoustic streaming around a cylinder in the absence of a temperature potential and free convective flow field in the absence of sound is invalid. Simple superposition is invalid because the differential equations which

describe the coupling between sound and convective heat transfer are nonlinear.

The second group of investigations [5, 6, 10, 11] on the effect of sound on average, local heat-transfer coefficients were conducted at sound pressure levels below the often reported critical sound pressure level of 140 db. The critical sound pressure level is the level below which the effect of sound on the heat-transfer coefficient is negligible. These investigations were performed below 140 db because the optical technique used failed above this level.

Richardson [5] has investigated the effect of horizontal, transverse sound fields on the average, local heat-transfer rate from a horizontal cylinder to air in free convection. Measurements and observations were made using a schlieren system. The cylinder used had an outside diameter of 0.75 inches. The range of Grashof numbers studied was 1.68×10^3 to 4.24×10^3. Quantitative measurements were made for sound pressure levels of 130 to 134 db which corresponds to Af products of 1.2 to 2.2 inches per second. Local changes of the heat-transfer rate of 5 to 10 per cent were measured. For these measurements, the ratios of amplitude to diameter ranged from 0.002 to 0.004. Measurements at angular positions around the cylinder between 0 degrees and beyond 110 degrees from the lower stagnation point showed a progressive change from a maximum increase at 0 degrees to a maximum decrease beyond 110 degrees. For sound pressure levels

of 130 to 134 db, there appeared to be no local influence of sound on the heat-transfer rate in the vicinity of 70 degrees from the bottom stagnation point. At higher sound pressure levels, the schlieren method was unreliable, but did provide a flow visualization for sound pressure levels between 135 to 140 db. Visual observations showed that at sound pressure levels between 135 to 140 db, the buoyant plume rose, widened, and divided into two parts. The two parts of the plume separated from each other as the sound intensity was increased and progressively moved farther apart until the position of separation of the plume on each side was about 100 degrees from the bottom of the cylinder. Richardson hypothesized that as the plume moved down the sides of the cylinder, the regions of locally reduced heat transfer were eliminated. The elimination of these regions of reduced heat transfer corresponded to the critical condition that has been observed in overall heat-transfer measurements. The conclusion was drawn that since the local processes were smoothly progressive, the critical level determined from average heat-transfer measurements had no intrinsic fluid-mechanical significance.

Fand [34] commented on Richardson's conclusion concerning the critical sound pressure level. The data presented in reference 12 by Fand were in contradiction to Richardson's observation that at SPL's close to the critical level, regions of locally reduced heat transfer were wiped away. Fand pointed out that the data in reference 12 demonstrated

quantitatively that even at supercritical intensities, regions of locally reduced heat transfer existed. Fand mentioned that Richardson's conclusions were drawn from qualitative observations and that the complete failure of the schlieren system at about 140 db could be related to thermoacoustic streaming. Fand maintained that a new type of flow (thermoacoustic streaming) does occur at 140 db and becomes fully developed after going through a transitional stage.

Richardson [6] reported an investigation of the effect of vertical transverse sound fields on the local heat transfer from a horizontal heated cylinder. The study was conducted for a sound pressure level range from 0 to about 140 db which corresponds to an Af product of 0 to 4.4 inch/sec. Three oscillatory frequencies of 709, 1084, and 1476 cycles per second were used. The test cylinder had a diameter of 1.83 inches. By observing the changes in the boundary-layer thickness and ray deflections made visible with a schlieren system, Richardson was able to make some qualitative observations. For sound pressure levels from 0 to 129 db or Af product from 0 to 1.2 inch/sec, no perceptible effect of sound on the local distribution of heat transfer was observed. For sound pressure levels between 129 and 137 db (Af product from 1.2 to 3 inches per second), there was a progressive local variation of boundary-layer thickness and heat transfer with the flow apparently remaining steady. For sound pressure levels above 137 db, unstable behavior developed in the flow. This unstable

behavior occurred first as a mode of laminar flow. Richardson stated that similarly to horizontally directed sound fields, vertically directed sound fields caused local changes in heat-transfer rates long before appreciable changes in average heat-transfer rates were detected. The initial local effects had opposite directions at the same positions on the cylinder for vertical and horizontal propagation. For vertical sound fields of sufficient intensity, Richardson observed that the boundary layer on the bottom of the cylinder thickened, became unstable, and bubbled up repeatedly into the top plume. Richardson further claimed that the superposition of isothermal streaming on the natural convective flow was qualitatively consistent with experimental results.

Richardson [11] reported the results of experiments with a heated horizontal cylinder subjected to either transverse horizontal or transverse vertical standing sound fields. The test cylinder was 1.83 inches in diameter, and sound pressure levels ranged from 120 to 140 db. The frequency range was 710 to 1470 cycles per second. Shadowgraphs for various test conditions were presented. Richardson stated that the observations made in these tests confirmed his earlier claims presented in references 5 and 6. The rising plume split progressively as the intensity of a horizontal sound field was increased. The reverse-flow bubble at the bottom of a cylinder in a vertical sound field was observed.

It should be mentioned that the results appearing in references 5, 6, and 11 were based on shadowgraph methods in which photographs of the heated region surrounding the cylinder were taken. The film on which the shadowgraphs were recorded had exposure times of five to eight seconds. With exposure times much longer than the time of one cycle of oscillation of the cylinder, it is difficult to say with any confidence to what thickness the photographed boundary layer corresponded.

CHAPTER III

THE DIFFERENTIAL INTERFEROMETER

Introduction and Historical Background

The interferometer has proved to be a useful and versatile instrument in many scientific and engineering fields. It has provided methods of measuring parameters with precision and convenience. For some measurements, interferometers have particular capabilities not provided by any other measuring device. In particular, the Mach-Zehnder interferometer has been frequently used to measure the temperature distribution around a heated or cooled body and to qualitatively observe the flow field surrounding the body.

The interferometer possesses several advantages over other measuring instruments when it is applied to heat-transfer problems. A thermocouple or some other measuring device disturbs the flow field around the test section merely by its presence, but the presence of light rays does not alter the flow field. The light rays pass through the medium leaving it undisturbed. Another advantage of the interferometer is that it is well suited for transient measurements of temperature distributions around a body. This is due to the fact that the light ray had practically no inertia. When transient measurements are desired, the only limiting factors are camera frame speed and film exposure time. Another advantage of the

interferometer is that measurements may be made on test objects of fairly complex shapes. Furthermore, the interferometer is an accurate and sensitive device that can be used to measure temperature to within a fraction of a degree. All of these factors combine to make the interferometer an extremely versatile and accurate instrument.

The type of interferometer used most extensively in the study of heat-transfer processes has been the Mach-Zehnder interferometer. The first applications of the Mach-Zehnder interferometer to temperature measurement were made by Kennard [35, 36] and Hansen [37] in the early 1930's. Since that time there have been numerous publications in which researchers have utilized a Mach-Zehnder interferometer to visualize flow fields and to measure heat-transfer coefficients (references 38 through 46, for example). A summary of optical techniques applied to heat-transfer measurements can be found in reference 47.

Although the Mach-Zehnder interferometer has been used extensively, it does have its limitations. The fringe pattern of the Mach-Zehnder yields information regarding the temperature distribution around a test object. Since the heat-transfer coefficient is proportional to the temperature gradient normal to the surface, the calculation of local heat-transfer coefficients with a Mach-Zehnder interferometer is a two step process. First, the fringe pattern must be analyzed to give the temperature distribution around the test body, and

then an additional procedure such as the graphical technique used by Eckert [39] must be carried out to provide the temperature gradient. Fortunately the differential interferometer does not require this two step procedure to measure the heat-transfer coefficient and is therefore a more desirable instrument when the heat-transfer coefficient is desired. A differential interferometer produces a fringe pattern in which the deflection of an individual fringe is proportional to the temperature gradient of the medium surrounding the test object. Thus, the interferogram of a differential interferometer is a direct measure of the convective heat-transfer coefficient.

The differential interferometer is a relatively new type of interferometer. This instrument is a particular form of a shearing interferometer which, according to Bryngdahl [48], was first used by Waetzmann [49]. The differential interferometer used in this investigation is based on a principle discovered by Normarski [50, 51, 52] for a microscope using polarized light and double refracting prisms. One of the first to apply this type differential interferometer was Philbert [53-56] who used it in the study of supersonic flow in a wind tunnel. Since then, the primary application of this instrument has been in the study of density distribution and shocks in supersonic wind tunnels [57-63]. A differential interferometer has also been used for the study of the quality of optical components [64-69]. Lamb and Schreiber [70] used

the differential interferometer to measure the variation of the index of refraction within an argon plasma.

The theory of operation of wavefront shearing interferometers that uses savart plates for ray separation has been described in references 48 and 72 through 77. Ingelstam [75, 76] has applied the differential interferometer to various diffusion problems for the measurement of diffusion coefficients. Mordchelles-Regnier and Kaplan [77] used the differential interferometer to visualize the flow pattern of air in a small gap between two plane surfaces.

While the Mach-Zehnder interferometer has been used extensively in heat-transfer work, the application of the differential interferometer to heat-transfer measurements has been very limited. Bryngdahl [73, 74] used the differential interferometer in the measurement of thermal conductivity of liquids (alcohol, glycerin, water, and castor oil). Spence [78] applied the differential interferometer to two-dimensional, laminar, free convection of water contained in a horizontal cylinder. The study was made under the condition of a constant wall temperature that was initially higher than the temperature of the water. The results of the test were presented in the form of isotherms of the water filled cavity as a function of time.

The differential interferometer used in this investigation and its application to heat and mass transfer are discussed in references 79 and 80. A brief description of

the optical components and principles of operation is included in these references.

The development of a single Wollaston prism schlieren interferometer and its application in local heat flux measurements for two-dimensional configurations are discussed in references 81 and 82. The single Wollaston prism schlieren interferometer is similar to the differential interferometer discussed here but has several limitations not associated with the differential interferometer. These limitations are discussed in reference 80.

Grossin, Jannot, and Viannay [83] have described an interferometer consisting of three astigmatic and cylindrical lenses. Like the differential interferometer, this instrument permits the measurement of the index of refraction gradient in an arbitrary direction relative to the test section.

The application of the differential interferometer to heat-transfer measurements has been limited, and the full potential of this instrument in the area of heat transfer has not been determined. One of the purposes of the present investigation has been to determine the potential of the differential interferometer when applied to heat-transfer problems.

Principles of Operation

This section begins with an in depth discussion of the

differential interferometer and its optical components. A supporting discussion and further details may be found in Appendix A. Readers desiring a brief explanation of the differential interferometer are referred to references 79 and 80. This section concludes with the derivation of an expression relating the fringe shift and the index of refraction gradient produced within the test section. This expression forms the basis for the analysis presented in the following section which relates the fringe shift to the heat-transfer coefficient.

A schematic diagram of the differential interferometer used in this investigation is shown in Figure 1. The optical arrangement consists of a light source, a light filter, a condensing lens, a telescopic objective, three Wollaston prisms, two plane mirrors, two spherical mirrors, a polarizer, an analyzer, and an eyepiece.

The most critical component in the operation of the differential interferometer is a polarizing beam splitter. The most commonly used polarizing beam splitter is a Wollaston prism [84] although savart plates can be used. Since the differential interferometer used in this investigation utilizes a Wollaston prism for beam separation and for the production of parallel fringes, a detailed discussion and analysis of the Wollaston prism are presented in Appendix A. The results of Appendix A will be used in this section.

In the differential interferometer, light leaves the light source and passes through a condensing lens, through a

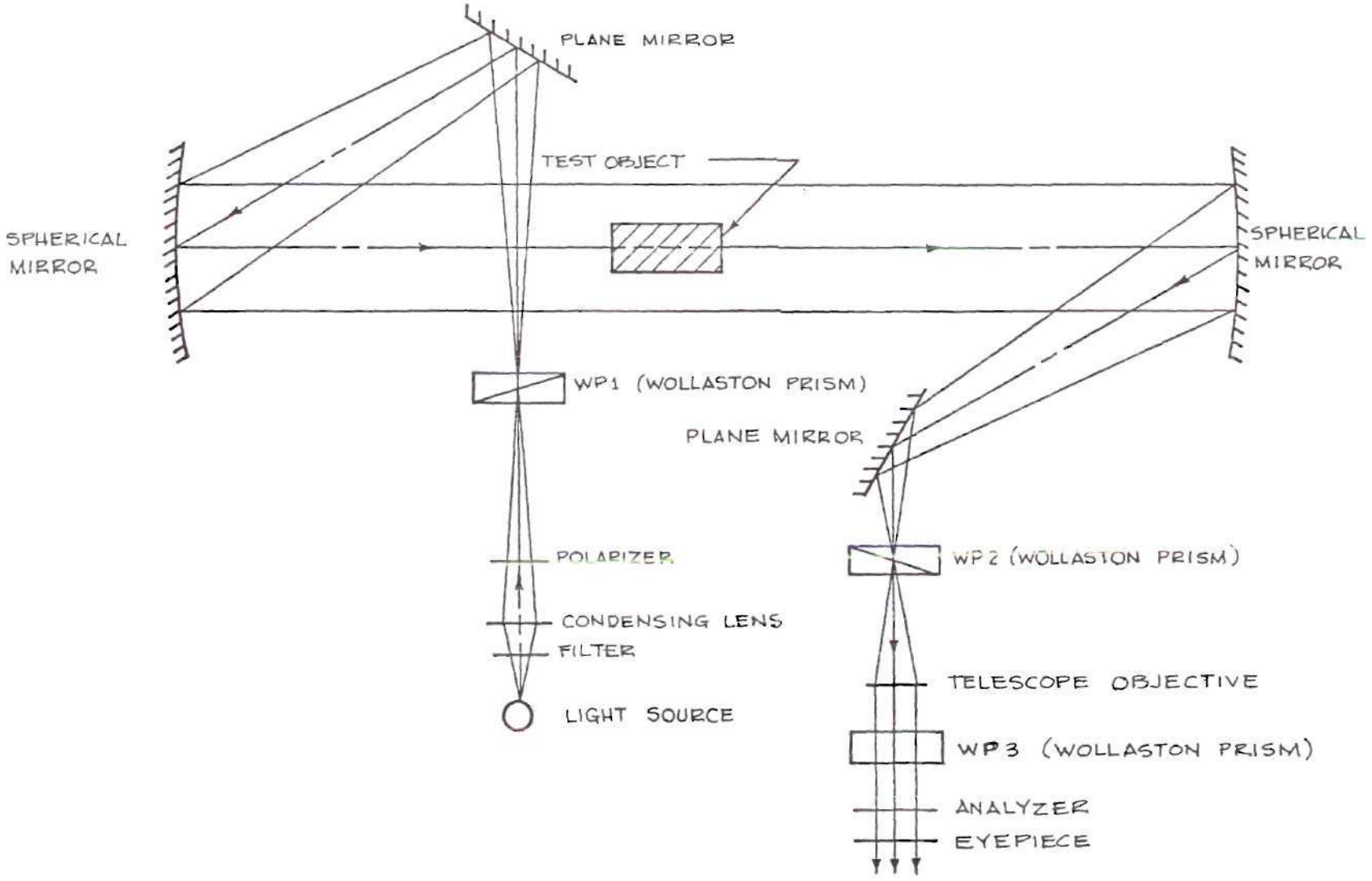

Figure 1. Schematic Diagram of a Differential Interferometer

filter, and then through a plane polarizer. The condensing lens focuses the light beam on the center line of the first Wollaston prism WP1. The plane polarizer is aligned with its plane of polarization at an angle of 45 degrees with the x_s-z plane as shown in Figure 2. With this alignment, an incident ray is polarized such that it has two components with equal magnitude electric vectors E_x and E_y which lie along the x_s and y axes, respectively. The component with the electric vector E_x will be referred to as ray x, and the component with the electric vector E_y will be referred to as ray y. The Wollaston prism causes ray x and ray y to diverge slightly as they leave the Wollaston prism. Ray y is deflected upward in the x_s-z plane, and ray x is deflected downward in the x_s-z plane. The total angle between ray x and ray y is given in reference 70

$$\alpha = 2(n_e - n_o)\tan\Theta \qquad (2)$$

where $(n_e - n_o)$ is the difference between the extraordinary and ordinary indices of refraction of the Wollaston prism material, and Θ is the wedge angle of the Wollaston prism.

After passing through WP1, the beam is reflected by a plane mirror onto a spherical mirror. WP1 is located in the focal plane of the spherical mirror so that after reflection from the mirror, ray x and ray y travel parallel, but slightly

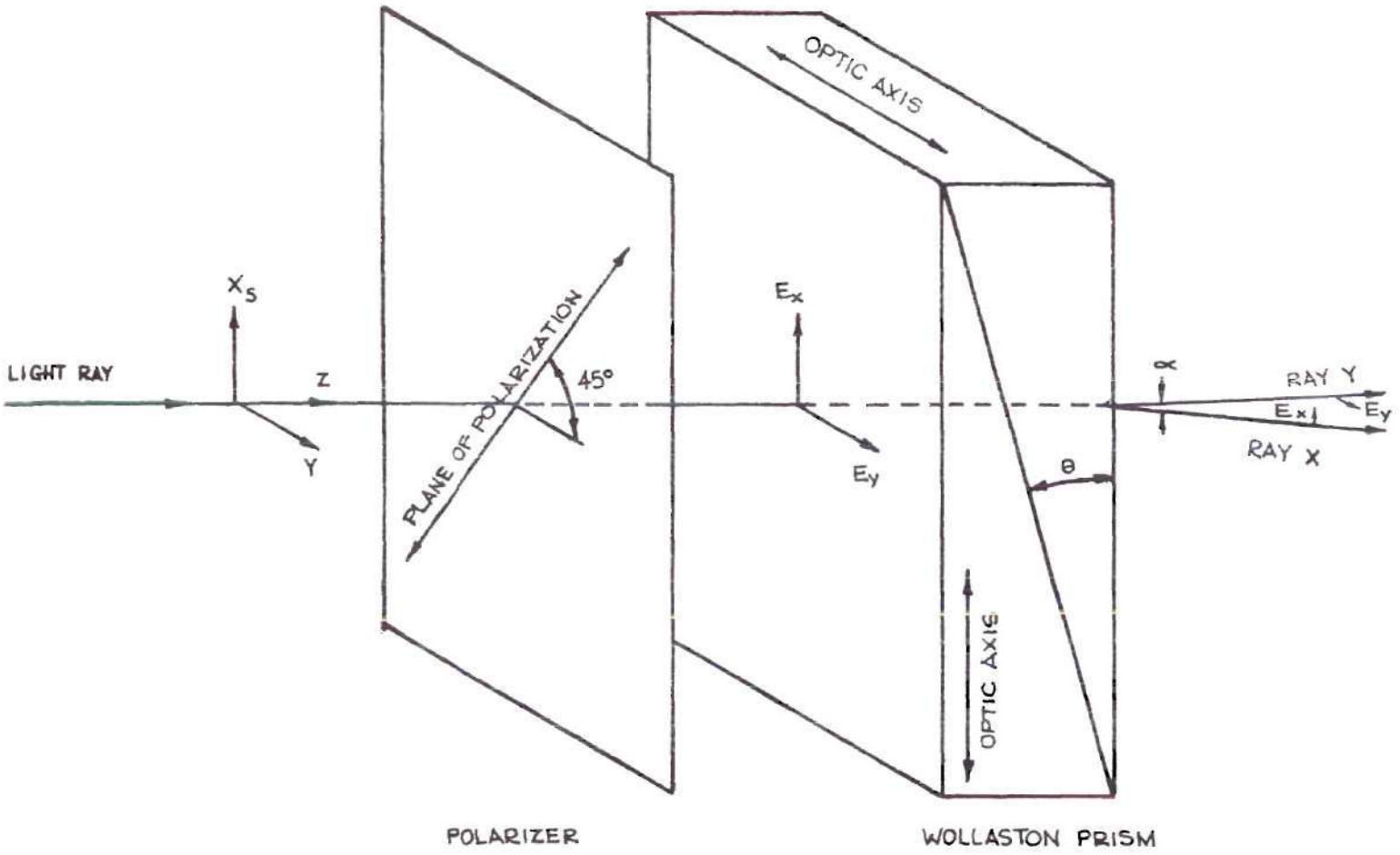

Figure 2. Division of a Single Ray Into Two Components

separated, paths through the test section. The separation distance Δx_s between ray x and ray y that originally formed an incident ray is

$$\Delta x_s = \alpha g \tag{3}$$

where g is the distance between WP1 and the spherical mirror. By substituting for α from Equation (2), the separation distance can be written as

$$\Delta x_s = 2g(n_e - n_o)\tan\Theta \tag{4}$$

After passing through the test section, the beam reaches the second spherical mirror where it is reflected toward a point in the focal plane of the spherical mirror. The beam is reflected by the second plane mirror and is focused on the second Wollaston prism WP2. The second Wollaston prism is identical to the first except that it has been rotated 180 degrees about the y axis so that the effect of the first prism is reversed by WP2. Thus, ray x and ray y are recombined into a single ray as shown schematically in Figure 3. If there is no test object in the test section, the diverging beam leaving WP2 is identical with the beam entering WP1.

After leaving WP2 the light rays pass through a

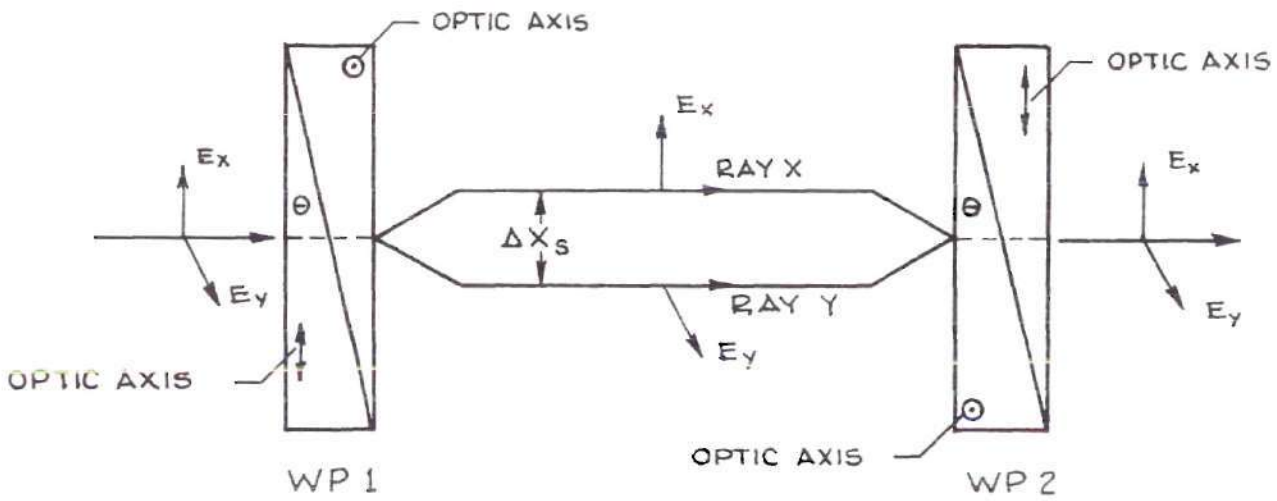

Figure 3. Schematic Diagram of the Recombination of Ray x and Ray y Which Form an Original Incident Ray

telescopic objective which directs the light beam through a circular area of a third Wollaston prism WP3. This prism produces a phase shift between ray x and ray y that is a linear function of the y coordinate. Upon leaving WP3, the light beam passes through an analyzer (a second polarizer in the system) which allows a visualization of the phase shift. A series of equally spaced fringes that are parallel to the x_s direction are produced when the beam passes through the analyzer. WP3 is rotated at 90 degrees with respect to WP1 and WP2 so the fringes are parallel to the x_s direction. WP3 can be rotated so the fringes will run in any desired direction, but experience indicates that the most convenient direction is parallel to the direction in which the gradient is being measured.

At the eyepiece, each ray of the fringe pattern appears to have traveled through the test section at the position (x_s,y); however, its ray x component traveled through at position $(x_s - \frac{\Delta x_s}{2},y)$, and its ray y component traveled through at position $(x_s + \frac{\Delta x_s}{2},y)$ where Δx_s is given by Equation (4). If a heated body is introduced into the test section of the interferometer, ray x and ray y pass through regions of slightly different temperature since they are separated by the distance Δx_s. As a result, there exists a difference in optical paths, $\Delta \ell$, between ray x and ray y when they leave the test section. This difference is given by

$$\Delta\ell = \Delta[(n_{ray\ x}-n_{ray\ y})L] = L\Delta n = m\lambda \qquad (5)$$

where L is the length of the heated test object in the direction of light propagation, $n_{ray\ x}$ is the index of refraction of the air through which ray x passes, $n_{ray\ y}$ is the index of refraction of the air through which ray y passes, n is the index of refraction for the wavelength of light λ, and m is the optical path difference in wavelengths which will be shown to be equivalent to fringe shifts. This optical path difference causes a fringe shift in the parallel fringe pattern produced by WP3.

The fringe patterns can be interpreted with the aid of Figures 4 and 5 and the results from Appendix A. As shown in Appendix A, WP3 produces a phase difference between ray x and ray y which is given by

$$\Delta\phi_{WP3} = Fy \qquad (6)$$

where F is a constant for a given wavelength of light and Wollaston prism. If no optical path difference exists in the test section, fringes parallel to the x_s axis are produced. The intensity of the light, I, leaving the analyzer is shown in Appendix A to be

$$I = K[1+\cos\Delta\phi] \qquad (7)$$

where K is a constant for a given light source and medium, and $\Delta\phi$ is the phase difference between the components ray x and ray y.

Whenever the air in the test section is isothermal, the total phase difference between ray x and ray y is due solely to WP3 or

$$\Delta\phi_{total} = \Delta\phi_{WP3} = Fy \tag{8}$$

Substitution of Equation (8) into Equation (7) gives

$$I = K[1+\cos Fy] \tag{9}$$

For the condition

$$I = 0 \tag{10}$$

the intensity of the light leaving the analyzer is zero, which corresponds to a black band or a dark fringe line. The condition for a dark fringe line for an isothermal test section is satisfied when

$$y = \frac{p\pi}{F} \tag{11}$$

where p is an odd integer. The fringe pattern for an

isothermal test section is shown schematically in Figure 4.

When an optical path difference is introduced into the test section, the phase difference in the test section is

$$\Delta\phi_{ts} = 2\pi m \tag{12}$$

The total phase difference between ray x and ray y is

$$\Delta\phi_{total} = \Delta\phi_{WP3} + \Delta\phi_{ts} \tag{13}$$

$$\Delta\phi_{total} = Fy + 2\pi m \tag{14}$$

Substitution of Equation (14) into Equation (7) gives

$$I = K[1+\cos(Fy+2\pi m)] \tag{15}$$

The condition for a dark fringe line expressed in Equation (10) is satisfied when

$$Fy+2\pi m = p\pi \tag{16}$$

where again p is an odd integer. Solving for y gives

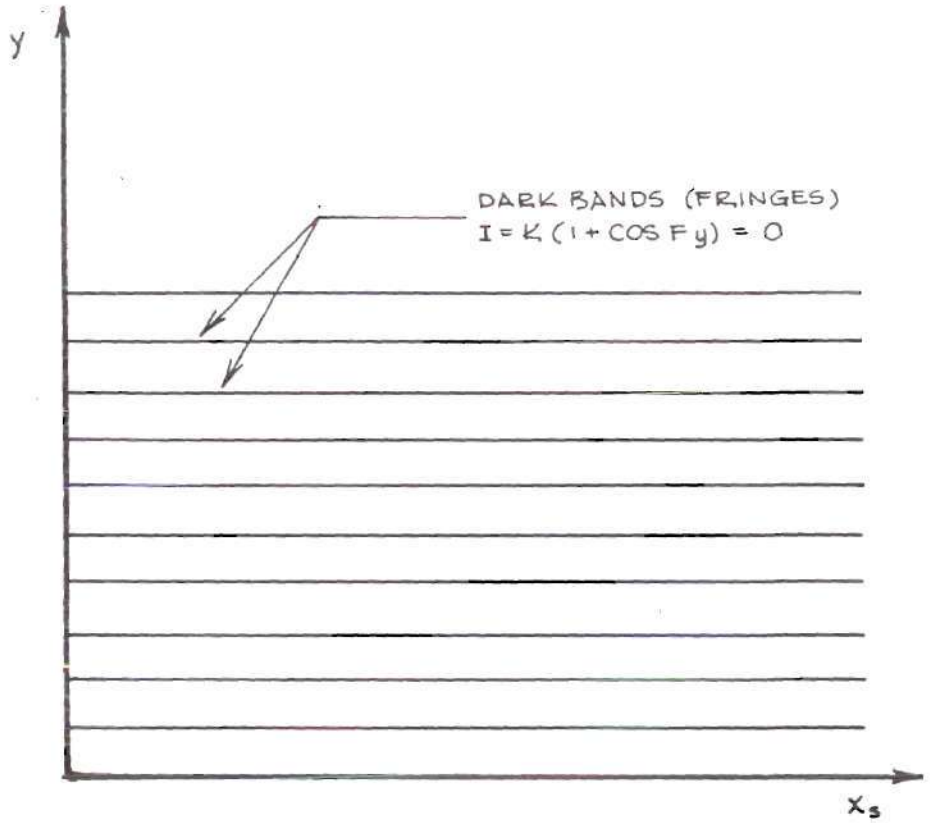

Figure 4. Resulting Fringe Pattern at Eyepiece for an Isothermal Test Section

$$y = \frac{p\pi}{F} - \frac{2\pi m}{F} \tag{17}$$

This equation corresponds to lines of zero intensity or dark fringe lines. Note that for m equal to zero, the fringe line is undeflected. For nonzero values of m, the fringe line is deflected by m fringe lines. Thus, the parallel fringe pattern is deflected at locations where there is a difference in optical paths in the test section. A hypothetical fringe pattern illustrating this case is shown schematically in Figure 5.

By measuring the fringe shift m from the undeflected fringe pattern and rewriting Equation (5), the difference in the index of refraction at locations traversed by ray x and ray y may be determined. This difference is given by

$$\Delta n = \frac{m\lambda}{L} \tag{18}$$

Since the separation distance between ray x and ray y is very small, the gradient of the index of refraction may be closely approximated by

$$\frac{\partial n}{\partial x_s} \simeq \frac{\Delta n}{\Delta x_s} \tag{19}$$

By combining Equations (4), (18), and (19), an equation for

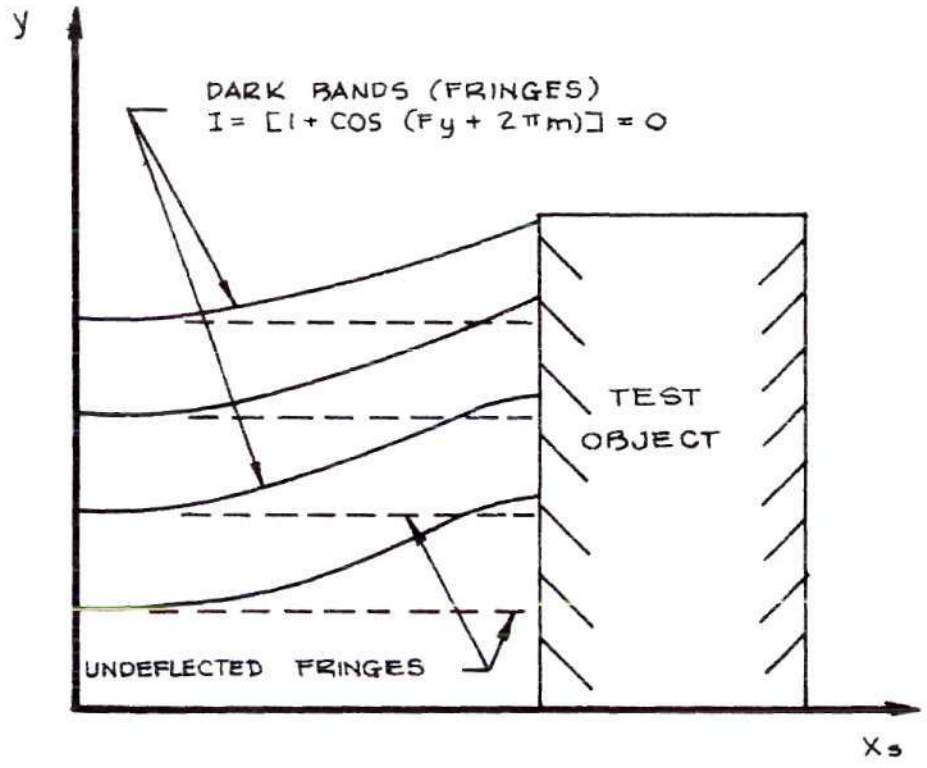

Figure 5. Hypothetical Fringe Pattern at Eyepiece for a Heated Test Object in the Test Section

the gradient of the index of refraction is obtained in terms of fringe shift m

$$\frac{\partial n}{\partial x_s} = \left[\frac{\lambda}{2Lg(n_e-n_o)\tan\theta}\right]m \qquad (20)$$

Therefore, once the single measurement of the fringe shift is made, Equation (20) may be used to calculate the x_s component of the gradient of the index of refraction in the medium surrounding the test object.

The first Wollaston prism and polarizer may be rotated so that the plane containing ray x and ray y can be made to intersect the test section at any arbitrary angle. Rotation of the plane containing the two rays gives rise to the possibility of measuring the gradient in the index of refraction in the test section at any arbitrary direction. Whenever the first Wollaston prism and polarizer are rotated, the second Wollaston prism and analyzer must also be rotated in the same direction through an equal angle to insure the action of the first prism is exactly reversed by the second.

In addition to the parallel fringe pattern produced by the differential interferometer when the third Wollaston prism is placed in the system, an infinite fringe pattern can be produced by removing the third Wollaston prism. Figure 6, which shows a heated vertical plate in still air, is an

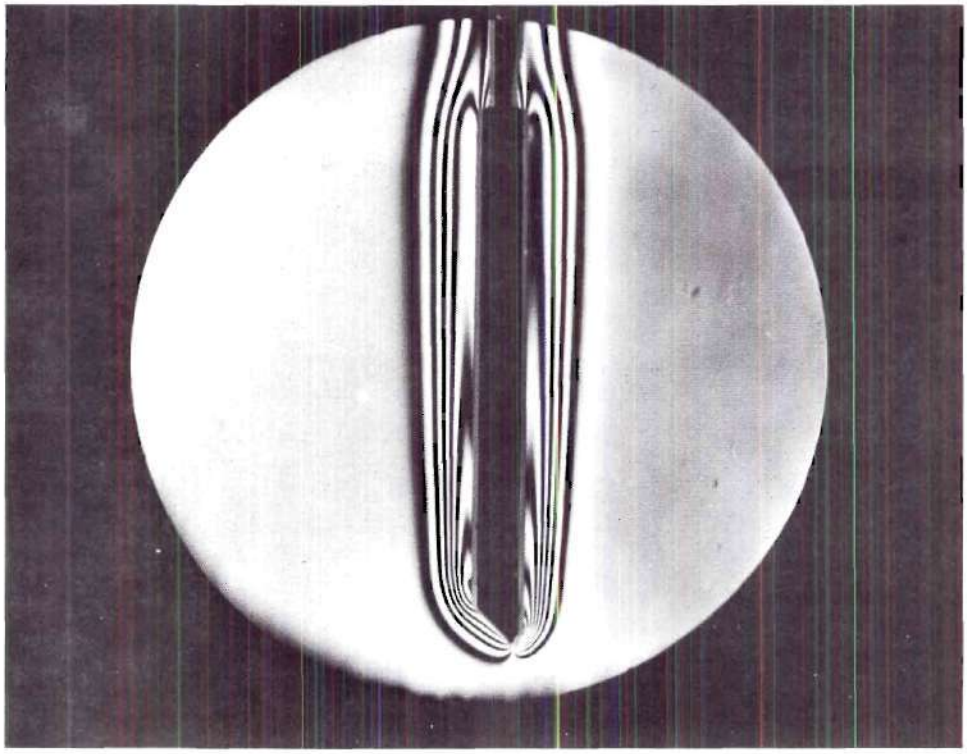

Figure 6. Infinite Fringe Lines Corresponding to a Constant Gradient of n Perpendicular to Plate

example of an infinite fringe interferogram. With the third Wollaston prism absent ($\Delta\phi_{WP3} = 0$), the only phase difference between ray x and ray y is produced in the test section. Equation (13) reduces to

$$\Delta\phi_{total} = \Delta\phi_{ts} = 2\pi m \tag{21}$$

The resulting interferogram is analogous to the infinite fringe produced by a Mach-Zehnder interferometer. The differential interferometer, when adjusted to the infinite fringe condition, produces a fringe line which corresponds to a line of constant gradient of index of refraction.

The double image of the heated plate and threaded support shown in Figure 6 is inherent within the system and can be explained with the aid of Figure 7. The double image is caused by the elimination of one of the components of an incident ray while the other component misses the plate and passes through the test section. In Figure 7, the ray y component of three incident rays within Δx_s distance of the plate misses the plate and passes through the test section, but the ray x component of incident rays 2 and 3 is blocked by the plate. When the ray y components of rays 2 and 3 enter the second Wollaston prism, they cannot combine with their companion component because its passage has been blocked by the test object. The ray y, which is closest to the test

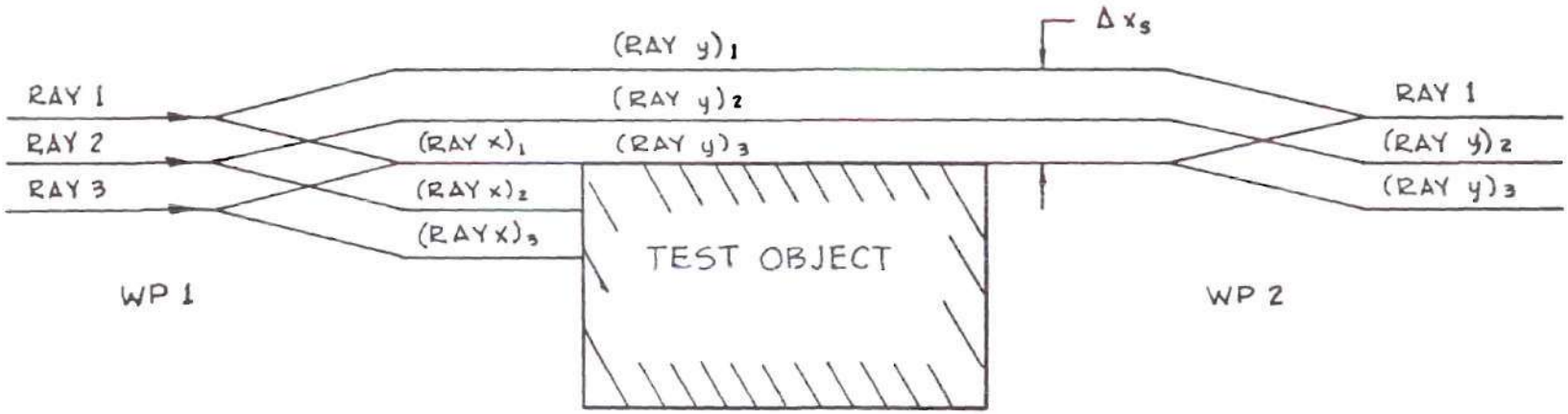

Figure 7. Ray Separation and Blockage Causing the Double Image on the Test Object

section and able to combine with its companion component, passes a distance Δx_s from the test object (ray y)$_1$ shown in Figure 7). The result is a gray area of reduced illumination surrounding the test section which has a thickness of Δx_s on all surfaces which are perpendicular to the plane containing ray x and ray y.

Application of the Differential Interferometer to Heat-Transfer Problems

In this section, an expression relating the heat-transfer coefficient to the fringe shift is derived. This expression forms the basis for the heat-transfer study discussed here.

The heat flux q(y) from the surface of a body to a fluid is given by Fourier's equation

$$q(y) = -k_s \left(\frac{\partial T}{\partial x_s}\right)_s \tag{22}$$

where $\left(\frac{\partial T}{\partial x_s}\right)_s$ is the temperature gradient in the x_s direction evaluated at surface of test object, k_s is the thermal conductivity of the air evaluated at the surface temperature, T_s, x_s is the coordinate normal to the surface of the body, and y is the coordinate parallel to the surface of the body. Thus, three quantities, k_s, T_s, and $\left(\frac{\partial T}{\partial x_s}\right)_s$, must be known in order to calculate the heat flux at the surface. The thermal

conductivity of air has been accurately measured as a function of temperature, and the surface temperature can be readily measured, but an accurate measurement of $(\frac{\partial T}{\partial x_s})_s$ is much more difficult to obtain. Thermocouples mounted in the flow field are often used to provide a measure of the temperature gradient, but this procedure is subject to considerable error. On the other hand, the differential interferometer is uniquely suited for making a fast and accurate measurement of this quantity.

As shown in the analysis above, the differential interferometer can produce a fringe pattern that is a measure of the gradient of the index of refraction in a direction perpendicular to the test section. The index of refraction gradient may be related to a temperature gradient by the analysis which follows. The analysis first requires the relationship between the index of refraction and the density. Next, the density is written in terms of the pressure and temperature by using an equation of state for the convective fluid. The result is an equation relating the fringe shift and the temperature gradient in the fluid.

The relationship between the index of refraction, n, and the density, ρ, of a fluid is given by the Lorenz-Lorentz equation

$$\frac{n^2-1}{n^2+2}\frac{1}{\rho} = \frac{(n+1)(n-1)}{n^2+2}\frac{1}{\rho} = K_1 \qquad (23)$$

where K_1 is a constant. Since $\frac{n+1}{n^2+2}$ is virtually constant (equal to 1.5) for air, Equation (23) can be written as

$$n-1 = 1.5K_1\rho = G\rho \tag{24}$$

where G is the Gladstone-Dale coefficient which for air is a function of the wavelength of light used and the partial pressure of the water vapor in the air. The expression used for G is given in Appendix D.

At atmospheric pressure, air can be considered an ideal gas which obeys the equation of state

$$P = \rho R_a T \tag{25}$$

where P is the absolute pressure, and R_a is the gas constant for air. Substitution of Equation (25) into Equation (24) gives

$$n-1 = \frac{GP}{R_a T} \tag{26}$$

Taking the partial derivative of the index of refraction with respect to x_s and noting that P can be considered a constant for free convection over a small body results in the expression

$$\frac{\partial n}{\partial x_s} = - \frac{GP}{R_a T^2} \left(\frac{\partial T}{\partial x_s}\right) \tag{27}$$

Equation (27) can be combined with Equation (20) to give an expression for $\frac{\partial T}{\partial x_s}$ in terms of fringe shift

$$\frac{\partial T}{\partial x_s} = - \left[\frac{\lambda R_a T^2}{2GPLg(n_e - n_o)\tan\theta}\right] m \tag{28}$$

The local heat flux can now be written in terms of fringe shift at the surface of the test section, m_s, by substituting Equation (28) into Equation (22). This relationship is

$$q(y) = \left[\frac{k_s R_a T_s^2 \lambda}{2GPLg(n_e - n_o)\tan\theta}\right] m_s \tag{29}$$

The relationship between the convective heat-transfer coefficient and the heat flux given by Newton's law of cooling is

$$h = \frac{q(y)}{T_s - T_\infty} \tag{30}$$

where T_∞ is the ambient temperature of the air surrounding

the test body. By combining Equations (29) and (30), an expression for the convective heat-transfer coefficient can be written in terms of known constants, measurable quantities, and the number of fringe shifts from an undisturbed position at the surface of the test section. The resulting expression for h is

$$h = \left[\frac{k_s R_a T_s^{\,2} \lambda}{2GPLg(n_e - n_o)(\tan\theta)(T_s - T_\infty)}\right] m_s \qquad (31)$$

This expression is the connecting link between the observed optical fringe shift, m_s, and the heat-transfer coefficient, h. The simplicity of this equation has proved to be extremely valuable, because for a plane surface, a single optical measurement provides a relatively simple and direct measurement of the heat-transfer coefficient that is usually difficult to obtain.

CHAPTER IV

SCOPE OF THE EXPERIMENT

Flat Plate

A preliminary investigation involving the measurement of local, steady state, free convective heat-transfer coefficients from a vertical, flat, copper plate was carried out. There were two main objectives of this preliminary study. The first was to check the accuracy of the differential interferometer in measuring local heat-transfer coefficients. The second was to become familiar with both the operation of the differential interferometer and the problems involved in its application. The tests consisted of measurements for a plate surface temperature of 100 degrees F above ambient room temperature. Three sensitivities of the instrument corresponding to three settings of the first two Wollaston prism angles of 1, 3, and 8 degrees were used.

Horizontal Cylinder

An investigation of the effect of horizontal, mechanical vibration on the heat-transfer rate from a heated, isothermal, horizontal cylinder to air in free convection was conducted. A differential interferometer was used to measure instantaneous, local heat-transfer coefficients throughout the cycle of oscillation.

The experimental measurements were subdivided into two phases. First, local heat-transfer coefficients for a nonvibrating, heated, isothermal cylinder losing heat to air by free convection were measured and then compared with published values. These tests were repeated several times to establish a reliable basis for comparison with vibratory tests.

The second phase consisted of the measurement of instantaneous, local heat-transfer coefficients under vibratory conditions. A series of tests were conducted at the same Grashof numbers as those of the stationary cylinder tests but at various amplitude to cylinder diameter ratios, $\frac{A}{D}$, and average Reynolds numbers, Re_A.

The ranges of parameters investigated were:

$$2.44 \times 10^4 \leq Gr \leq 7.60 \times 10^4 \tag{32}$$

$$0 \leq \frac{A}{D} \leq 1.78 \tag{33}$$

$$0 \leq Re_A \leq 660 \tag{34}$$

The lower limit of the Grashof number corresponds to an excess temperature of 25 degrees F while the upper limit value corresponds to an excess temperature of 100 degrees F. The Reynolds number stated here uses the average velocity

(four times the Af product) as a characteristic velocity. The upper limit on the Reynolds number corresponds to an Af product of 4.32 inches per second.

The parameter ranges were selected for the following reasons: 1.) a lack of data existed in these regions; 2.) the Af product was chosen to span the critical value of Af where $\overline{Nu}_V$ varies appreciably from $\overline{Nu}_F$; and 3.) the range of $\frac{A}{D}$ was determined by the interferometric field of view and by the fact that the size of the cylinder had to be large enough to allow sufficient resolution to provide local values of the heat-transfer coefficient.

The tests conducted are summarized in Table 1. Several tests were conducted at higher Re_A than those indicated in Table 1 but were not reduced because the resolution of the system was not sufficient to determine the position of the deflected fringes at the cylinder surface.

Table 1. Summary of Test Conditions

Test No.	$\frac{A}{D}$	ΔT °F	Af inch/sec
01	1/8	25	1
02	1/8	50	1
03	1/8	100	1
04	1/4	25	1
05	1/4	25	2
06	1/4	50	1
07	1/4	50	2
08	1/4	100	1
09	1/4	100	2
10	3/8	25	1
11	3/8	25	2
12	3/8	25	4
13	1/2	25	1
14	1/2	25	2
15	1/2	25	2
16	1/2	25	4
17	1/2	50	1
18	1/2	50	2
19	1/2	50	4
20	1/2	100	1
21	1/2	100	2
22	1	25	1
23	1	25	2
24	1	25	4
25	1	50	1
26	1	50	1
27	1	50	2
28	1	50	4
29	1	100	1
30	1	100	2
31	1-3/4	25	1
32	1-3/4	25	2
33	1-3/4	25	4
34	1-3/4	50	1
35	1-3/4	50	2
36	1-3/4	50	4
37	1-3/4	100	1
38	1-3/4	100	2

CHAPTER V

APPARATUS

Flat Plate

Local, steady state, free convective heat-transfer coefficients from a vertical flat plate were measured during preliminary tests. The plate used in these tests was copper and had a cross section of 0.22 by 2.86 inches and a length of 12 inches. The plate was machined to provide a sharp leading edge and ground on all vertical surfaces to provide a very smooth surface. An oven was used to preheat the plate and a ten-gauge copper constantan thermocouple was used to measure the temperature of the plate.

Cylinder

The copper test cylinder used for both the stationary and vibratory free convective tests is shown in Figure 8. The cylinder was 0.982 inches in diameter and 11.96 inches long.

The cylinder was machined from a 1.125 inch diameter cylindrical copper stock. A center hole was drilled, bored, and reamed so that a tubular heating element could be inserted. Both ends of the hole were enlarged and tapped for supports to attach the cylinder to the yoke of the vibrational equipment. Thermocouple holes were drilled in one end

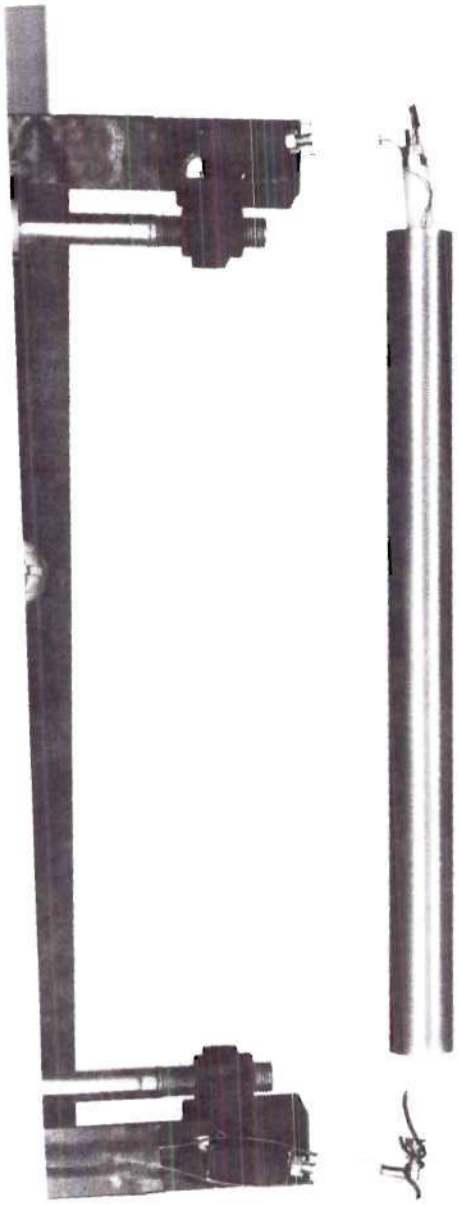

Figure 8. Test Cylinder

of the cylinder. The positions of the holes are shown in Figure 9.

Since the cylinder was to be used in the differential interferometer where the light would pass over the outer surface in an axial direction, the uniformity of the outside diameter of the cylinder was very critical. An attempt to turn down the surface uniformly on a lathe was unsuccessful. After this operation had been performed, the outside diameter of the cylinder varied by as much as 0.002 inches from one end to the other. This variation was reduced to less than $\pm$0.0001 by centerless grinding.

The surface of the cylinder was gold plated. Gold was selected as the plating material because it has a low emissivity and because it is one of the most inert materials known. A low emissivity is desirable in order to reduce radiant losses from the cylinder, and inertness of the surface is required so that the surface properties will not change with time.

The supports which attached the cylinder to the yoke of the vibrational equipment were made of nylon. Stainless steel attachments were used to connect the nylon supports to the aluminum yoke. The stainless steel attachments had to be designed sufficiently thin so that blockage of the end view of the cylinder was minimized since the end of the cylinder had to be observed through the differential interferometer. In addition to being thin, the supports had to

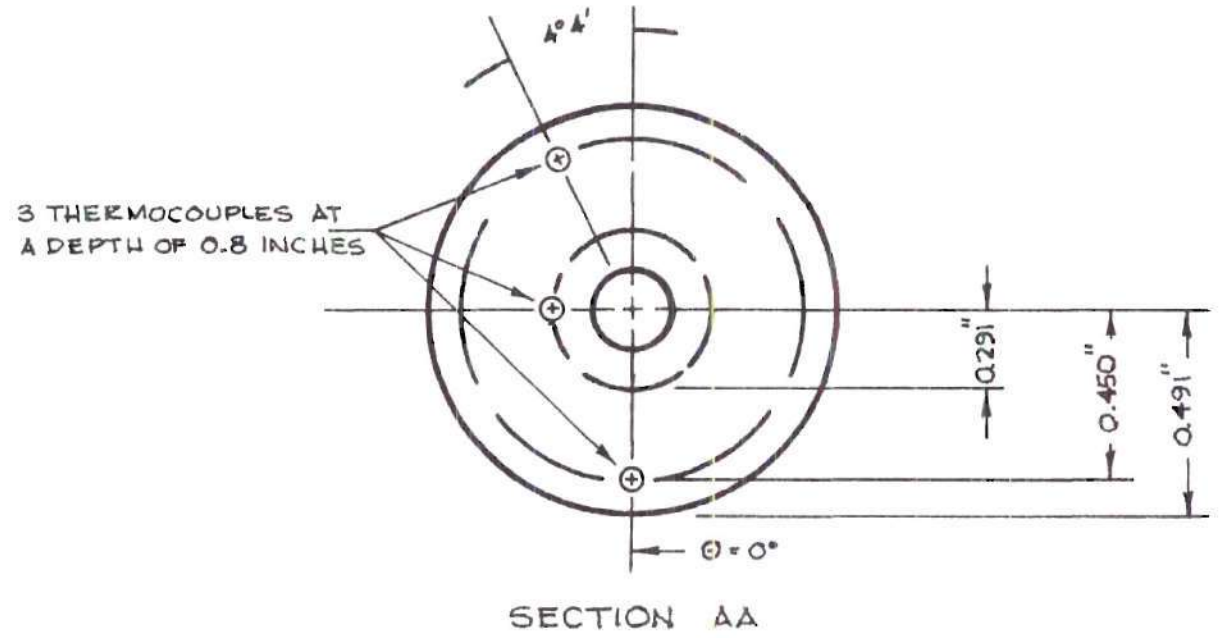

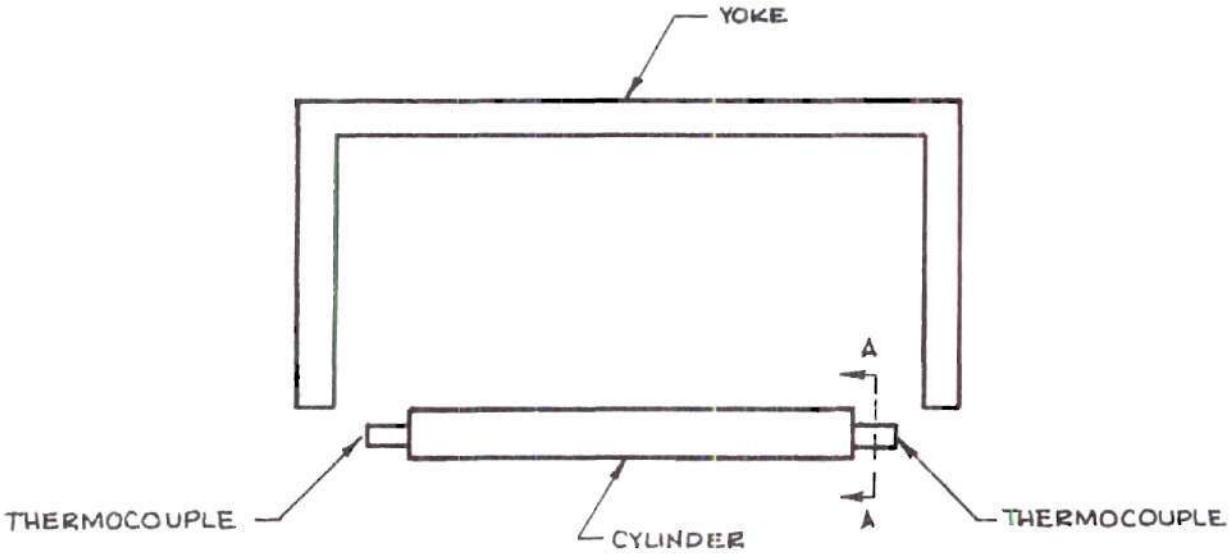

Figure 9. Locations of Cylinder and Support Thermocouples

be strong to support the cylinder under the vibrational conditions. The support materials were selected because of their relative strength and low values of thermal conductivity which minimized conductive losses through the supports.

A Chromalox Cartridge Tubular Heating Element, Type CI, was used to heat the cylinder. The surface of the heating element was turned down on a lathe until a very snug sliding fit existed between the element and the cylinder.

Copper constantan thermocouples were inserted into one end of the cylinder and into the ends of both nylon supports. The positions of the thermocouples are shown in Figure 9. Small thermocouple wires 0.005 inches in diameter (36-gauge) were used so that any transients in the cylinder temperature could be sensed. The thermocouples were calibrated using a silicon constant temperature bath and a calibrated thermometer. All but the tips of the thermocouples were sprayed several times with Silicone Corona Dope in an attempt to reduce the possibility of error in temperature measurements. The cylinder thermocouples were covered with epoxy and embedded in the cylinder.

The Differential Interferometer and Shield

The interferometer used in this study was a Model D1 manufactured by Winfried Schrader of Germany. A shield which surrounded the interferometer was constructed to minimize the effects of any room air currents (Figure 10). The

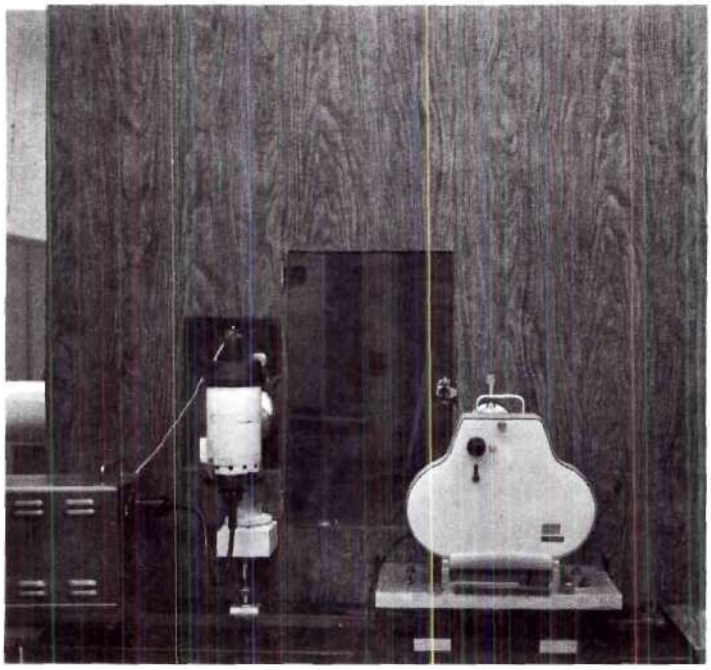

Figure 10. The Differential Interferometer and Shield

inside of the shield was painted with black paint with an emissivity of 0.97. The bottom of the shield contained a porous packing material which dampened extraneous air currents but still allowed air to freely feed the heated cylinder. The top of the shield was left open so that the buoyant convective plume was able to leave the shield unobstructed.

Vibrational Equipment

The vibrational heat-transfer tests required a device capable of producing a fairly large-amplitude (0.12 to 1.78 inches), fairly low-frequency (0.57 to 12 cycles per second), horizontal, sinusoidal motion of the test cylinder. An electronic shaker could not be used because of the amplitude requirements. A scotch yoke mechanism which transforms constant speed angular motion into simple harmonic motion was designed for the vibrational tests because it met all of the vibrational requirements. The mechanism utilized rotating counterbalance weights to counteract the inertial forces of the yoke and cylinder. The counterbalance weights were placed on two circular plates which rotated in opposite directions from each other and at the same frequency as the vibrating cylinder. The motion of the counterbalance weights produced forces which cancelled the inertial forces of the cylinder and its support. Without the counterbalance weights, vibrations within the apparatus were objectionable, particularly at high frequencies.

The final design of the vibrational system is shown in Figure 11. A 3/4 horsepower direct current motor was used to drive the system. Below 12 cycles per second, the system performed well with a minimum of extraneous vibration. Tests were not conducted above 12 cycles per second because the system vibration (due to the driving motor, pulleys, flywheels, etc.) was excessive. Below 12 cycles per second, frequency control was accomplished in two ways. A variable ratio pulley system was used so large variations in frequency could be obtained with the driving motor running near 3/4 of its rated speed. The direct current motor allowed fine adjustments of the frequency.

The amplitude of oscillation was varied by changing the position at which the crank rod was attached to the face plate. Holes were drilled and tapped in the face plate at 1/8 inch increments corresponding to vibrational amplitudes of 1/8 to 1-3/4 inches.

Photography and Interferogram Analysis

The interferograms for the local, steady state, free convective heat-transfer measurements from a vertical flat plate were taken with a 135 mm Graflex Optar Camera. The interferograms were recorded on Kodak Tri-X Pan 4 by 5 inch negatives. The negatives were analyzed using a microscope with a magnification factor of 20. Integer fringe shifts were obtained by linear interpolation using the distance

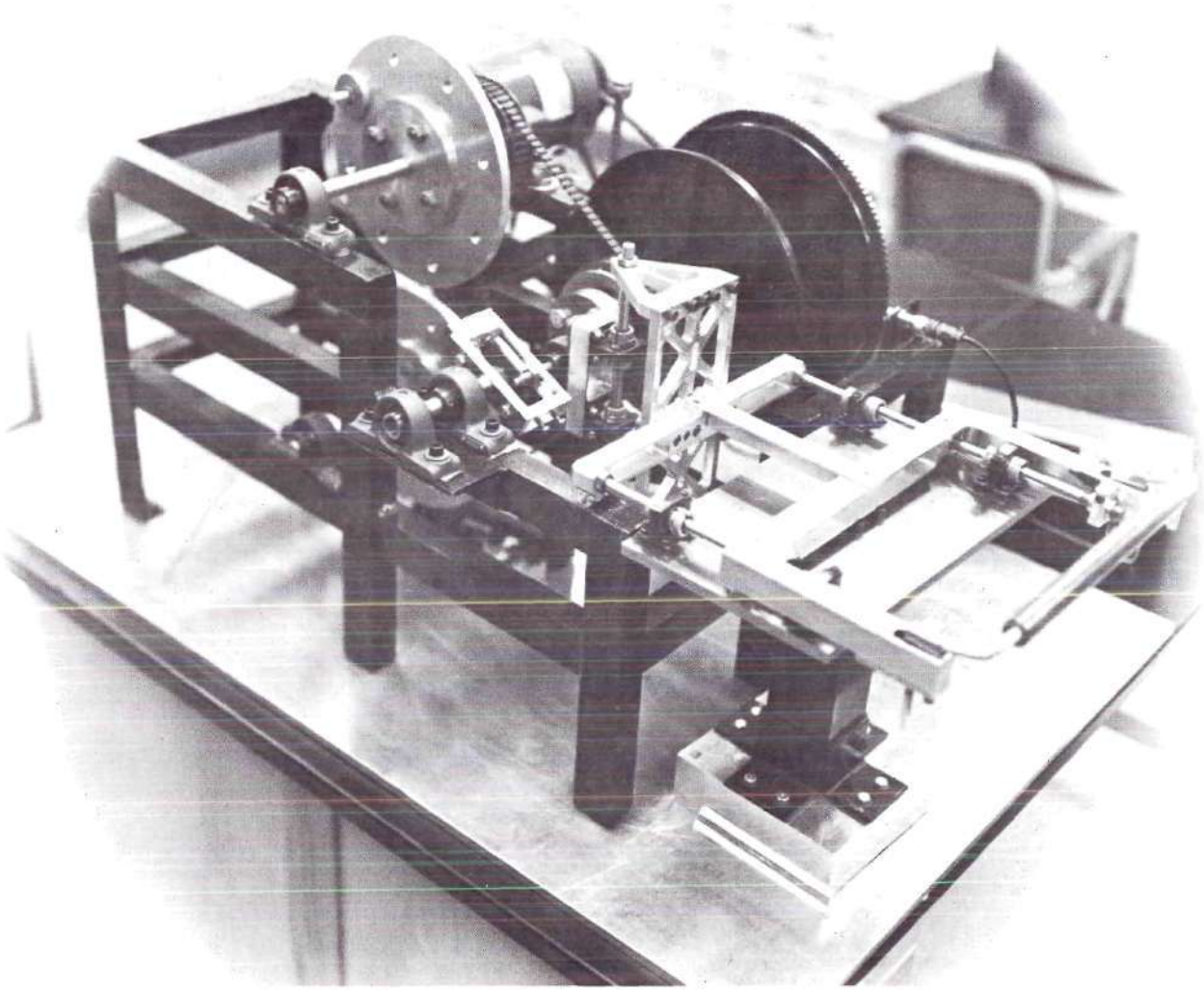

Figure 11. Vibrational System

between the undeflected fringe and the two nearest deflected fringes. Problems with aligning the negative and with the uncertainty of the path of the undeflected fringe made this method extremely tedious so a different method was used for the cylinder tests.

The interferograms for both the stationary and oscillating cylinder tests were taken with a Red Lake Laboratories Hycam 16 mm High Speed Camera. The camera was operated at a frame speed of 300 to 2000 frames per second depending on the frequency of oscillation of the cylinder. The interferograms were recorded on 16 mm high speed motion picture film (Kodak Reversal 7277 film). The interferograms were magnified approximately ten times by projection onto a screen where measurements could be made. Fringe shifts were obtained by comparing the projected deflected fringe pattern with an undeflected fringe pattern drawn on the screen. A measurement of the film magnification was facilitated by placing dividers in the test section so that their image appeared on each frame of the film. Two dividers set at a known separation distance were used. One was oriented horizontally and the other vertically. A plumb bob in the test section was used as a zero horizontal reference for the location of the cylinder.

Supporting Equipment

The frequency of vibration was measured with a

magnetic pickup (see Figure 11) and an electronic counter. The magnetic pickup was adjusted to count the number of teeth on a flywheel which rotated with the Scotch yoke mechanism.

During each test the cylinder temperature was measured by means of thermocouples placed at locations shown in Figure 9. In addition, the ambient air temperature was measured by two thermocouples placed below the cylinder. All thermocouples were calibrated in a constant temperature silicon bath.

The power input to both the heater within the test cylinder and the motor driving the scotch yoke mechanism was recorded. The power to the heater was used in an energy balance on the cylinder as a check on the average heat-transfer coefficient while the power required to drive the vibration motor was used to determine the energy input necessary to increase the heat transfer from the cylinder.

The atmospheric pressure and the relative humidity were recorded for each test using a barometer and a sling psychrometer, respectively.

CHAPTER VI

EXPERIMENTAL PROCEDURE AND DATA REDUCTION

Flat Plate

For the flat plate tests, both infinite fringe and parallel fringe patterns were recorded. Infinite fringe patterns (see Figure 6) were used to visualize the laminar nature of the heated air surrounding the plate and to provide a measure of the boundary-layer thickness. Parallel fringe interferograms with the undisturbed fringes perpendicular to the plate were used for the heat-transfer measurements. Parallel fringe interferograms with the fringes oriented vertically were used to verify the assumption that the plate was isothermal at any instant of time.

All tests were conducted for a plate temperature that was 100 degrees F above the room temperature. The plate was heated in an oven and then positioned in the test section of the differential interferometer. The heat transferred from the plate was supplied by the internal energy of the plate; however, according to a criterion by Gebhart [85-89], the thermal capacity of the plate was sufficiently high so that at any instant of time, the heat-transfer process could be considered to be steady state. The Biot number of the plate was approximately 0.03 so the plate temperature was considered

to be uniform. Both the plate temperature and the room temperature were continually monitored with thermocouples. As the plate temperature reached 100 degrees F above the room temperature, a 4 by 5 inch photograph of the interferogram was taken. The interferogram was analyzed using a microscope to obtain fringe shifts along the surface of the plate. The fringe shift measurements were used in Equation (31) of Chapter III to calculate local heat-transfer coefficients. The results of these measurements are shown in Figure 15 of Chapter VII.

Stationary Horizontal Cylinder

The stationary cylinder tests were conducted for cylinder temperatures of 25, 50, and 100 degrees F above room temperature. The cylinder was heated by a heating element that was located axially in the cylinder. The input to the heating element was adjusted until the temperature difference between the cylinder and the room stabilized at a value very close to the desired value. After the temperature difference was stable for at least 15 minutes, interferograms were recorded with a high speed camera. Both infinite fringe and parallel fringe interferograms were photographed for gradients in the vertical and horizontal directions. The power input to the cylinder, the cylinder temperature, the room temperature, the atmospheric pressure, and the relative humidity were measured.

Interferograms for both vertical and horizontal gradients were photographed so that the heat-transfer coefficient could be calculated at any point around the cylinder. For example, if the heat-transfer coefficient at point P in Figure 12 is required, the temperature gradient normal to the wall at point P must be obtained. The temperature gradient normal to the wall (r direction) written in terms of the temperature gradient in the vertical direction (η direction) and the temperature gradient in the horizontal direction (ζ direction) is

$$\frac{\partial T}{\partial r} = \frac{\partial T}{\partial \zeta}\cos\gamma_R + \frac{\partial T}{\partial \eta}\sin\gamma_R \qquad (35)$$

By combining Equation (35) with Equations (22), (28), and (30), the expression for the heat-transfer coefficient at point P may be derived. This expression is given by Equation (31) where

$$m_s = m_\zeta \cos\gamma_R + m_\eta \sin\gamma_R \qquad (36)$$

where m_ζ is the fringe shift due to the horizontal gradient, and m_η is the fringe shift due to the vertical gradient. Thus, the heat-transfer coefficient at any point on the cylinder surface can be calculated once fringe shifts for both vertical

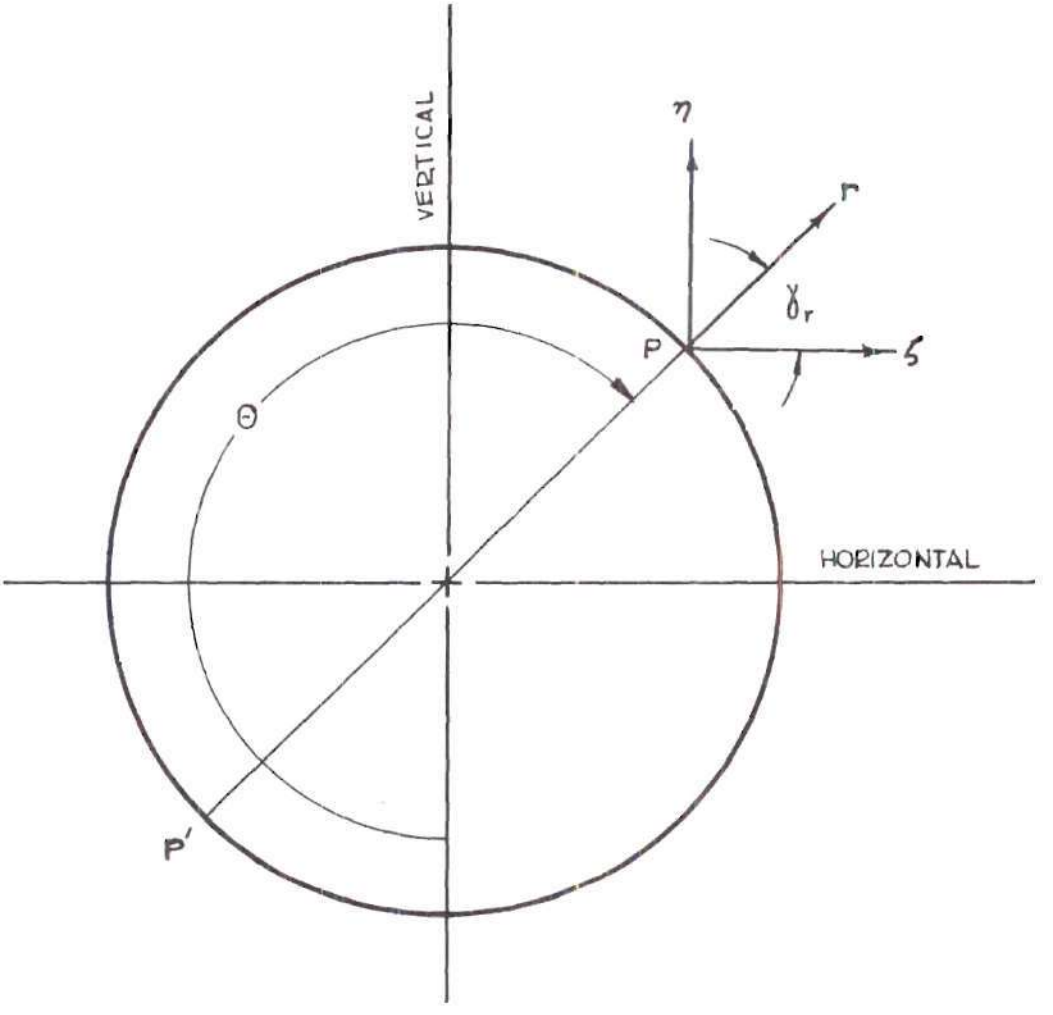

Figure 12. Determination of the Normal Component of Temperature Gradient on a Curved Surface

and horizontal gradients are obtained.

The method of measuring the fringe shifts for both vertical and horizontal gradients will be discussed next. This method was applied to the vibratory cylinder tests as well as the stationary cylinder tests.

The interferograms were projected on a screen which had an undeflected fringe pattern drawn on it. The undeflected fringe pattern was carefully aligned with the deflected fringe pattern. The magnification of the projected interferogram was determined from the pair of dividers located in the test section. The diameter of the projected cylinder, D_{proj}, was calculated from the magnification, M, and the actual diameter of the cylinder, D, or

$$D_{proj} = DM \tag{37}$$

Using the center of the cylinder found by construction, a circle of diameter D_{proj} was drawn on the screen.

The angular position, θ, around the cylinder of the intersection of a fringe lines with the cylinder surface was measured from the zero location at the geometric bottom of the cylinder (Figure 12). The magnitude of the fringe shift at the cylinder surface was measured by first relating the intersection of the undeflected fringe pattern and the cylinder surface with θ. Next the angular position of the intersection of the deflected fringe pattern and the cylinder

surface was determined. Fringe shift measurements were determined by comparing the angular intersection of the undeflected and deflected fringe patterns with the cylinder surface.

The undeflected fringe lines were numbered consecutively from bottom to top in the horizontal pattern and from right to left in the vertical pattern. The fringe numbers, $N_u(\theta)$, of horizontal, straight, and equidistant fringe lines (Figure 13) that intersect the cylinder surface may be related to the angular variable θ through the expression

$$N_u(\theta) = a_f - b_f \cos\theta \tag{38}$$

where a_f is the fringe number at the center of the circle, and b_f is the radius of the circle in fringes. For the hypothetical fringe pattern shown in Figure 13,

$$a_f = (i+5) + \frac{M3}{M4} \tag{39}$$

and

$$b_f = \frac{(i+9+\frac{M1}{M2}) - (i+1+\frac{M5}{M6})}{2} \tag{40}$$

Similarly, the fringe number of an undeflected vertical fringe pattern is given by

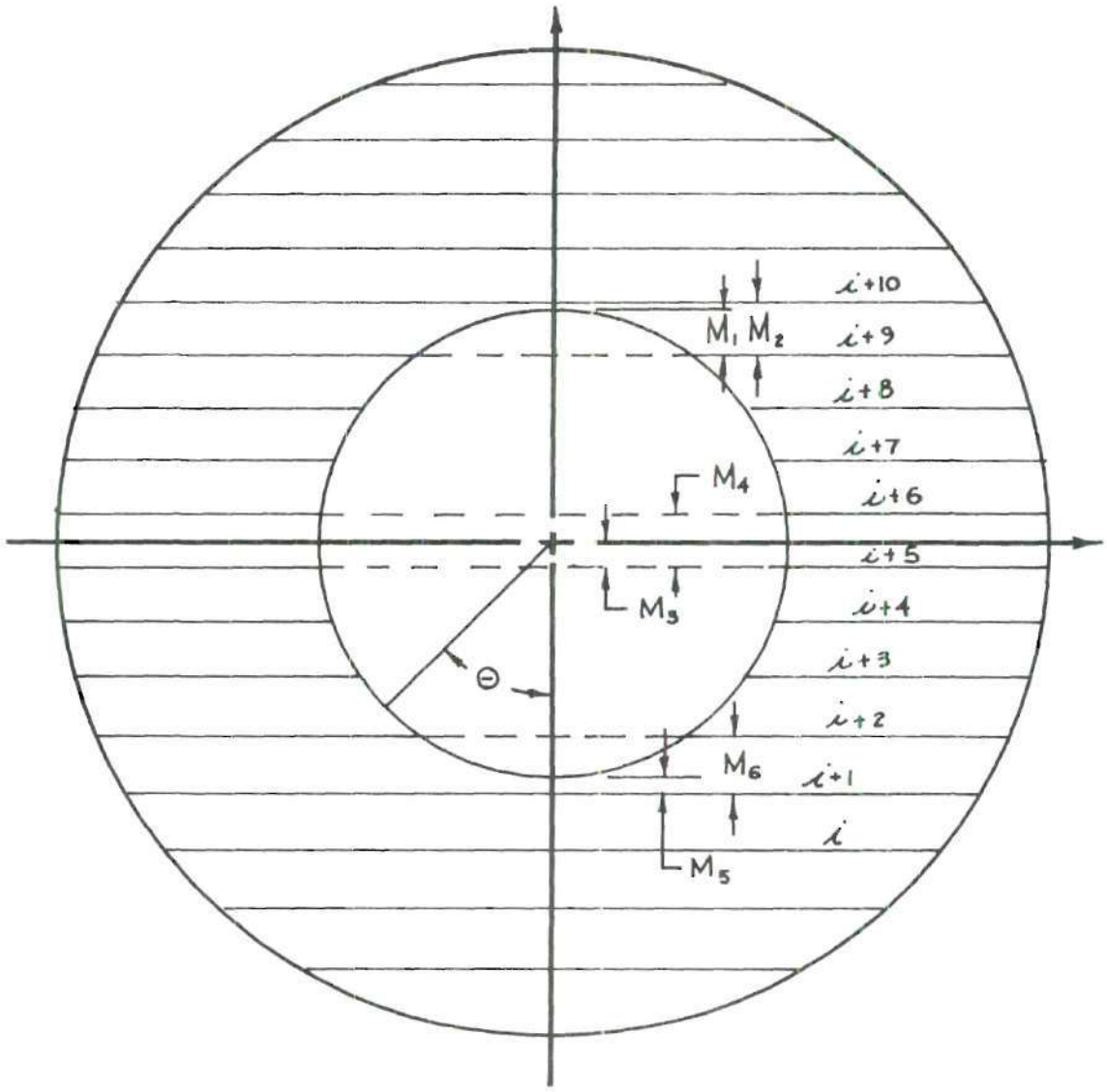

Figure 13. Hypothetical Undeflected Horizontal Fringe Pattern

$$N_u(\theta) = a_f + b_f \sin\theta \tag{41}$$

The accuracy of Equations (38) and (41) in predicting the position of undeflected fringes was checked since the actual undeflected fringe pattern was neither perfectly straight nor equally spaced. The cylinder outline was drawn on the undeflected fringe pattern at various locations and the θ position for each fringe intersecting the cylinder outline was recorded. Values of a_f and b_f were measured, and the fringe numbers were calculated for the θ positions recorded by using Equations (38) and (41). The average difference between the calculated and measured fringe numbers was 0.025 fringes. Since this difference was small, the intersection of the undeflected fringe pattern with the cylinder was determined by the measurement of a_f and b_f and the use of Equations (38) and (41).

Fringe shift measurements at the surface of the cylinder were determined once the θ intersection of all deflected fringes had been measured. The fringe shift $m(\theta)$ was then

$$m(\theta) = N_d(\theta) - N_u(\theta) \tag{42}$$

where $N_d(\theta)$ is the deflected fringe number, and $N_u(\theta)$ is calculated from Equation (38) for horizontal measurements and from Equation (41) for vertical measurements. Since it was

desirable to measure local heat-transfer coefficients for equal increments in θ, an interpolation scheme was used to provide fringe shift measurements for every 15 degree increments in θ.

Local heat-transfer coefficients, $h(\theta)$, were calculated using Equations (31) and (36) for 15 degree increments in θ. An average heat-transfer coefficient, $\bar{h}$, was obtained by averaging the local values over the entire cylinder surface

$$\bar{h} = \frac{1}{2\pi} \int_0^{2\pi} h(\theta) d\theta \qquad (43)$$

The integration was performed numerically using Simpson's rule.

An energy balance was performed on the test cylinder as a check on the accuracy of the average heat-transfer coefficient. The energy input to the heater mounted inside the cylinder was measured and was reduced by non-convective and end losses. Radiative losses from the cylinder, convective end losses, conductive losses through the nylon supports, conductive thermocouple lead losses, and conductive electrical lead losses were calculated. The remaining energy was assumed to be convected from the surface of the cylinder and used to calculate an average heat-transfer coefficient. Therefore, the input to the heater provided a check on the average heat-

transfer coefficient measured from the fringe shifts. Details of this calculation are discussed in Appendix E.

All of the heat-transfer coefficient data was converted to Nusselt number data by using the equation

$$Nu = \frac{hD}{k} \tag{44}$$

where h is the heat-transfer coefficient, D is the cylinder diameter, and k is the thermal conductivity of air at the film temperature. The stationary data results are presented in Chapter VII.

Vibrating Horizontal Cylinder

Measurements for the vibrating cylinder were conducted in a manner similar to those for the stationary tests. Additional measurements of the frequency of oscillation and the power to the vibrational equipment were recorded. For all vibrational tests, the amplitude of oscillation was measured using the interferograms as explained below.

The motion of the cylinder was sinusoidal with the left extreme position of oscillation denoted as the location where ψ equals 0 degrees. The symbol ψ was used to denote the position of the cylinder in degrees from the zero position. Over an entire cycle of oscillation, the second half of the cycle was symmetrical with the first half if the front

half of the cylinder (θ from 0 to 180 degrees) and the back half of the cylinder (θ from 180 to 360 degrees) reverse roles at ψ equal to 180 degrees. This can be seen with the aid of the schematic diagram of one oscillation of the cylinder shown in Figure 14.

It may appear that symmetry also exists around values of ψ of 90 degrees and 270 degrees. For example, values of ψ of 30 degrees and 150 degrees may appear to be equivalent since the instantaneous velocities for these positions are equal. However, there is a difference between these two positions due to the fact that the effect of the previous cycle of oscillation is much greater at 30 degrees than at 150 degrees. Observation of infinite fringe interferograms indicated that for ψ equal to 30 degrees the cylinder was passing through previously heated air, but at ψ equal to 150 degrees, the previously heated air appeared to have time to rise out of the cylinder's path. Thus, the effect of the previous oscillation was much less at 150 degrees, and ψ equal to 90 degrees was not a position of symmetry.

Since the second half of one cycle of oscillation is symmetrical with the first half, only the first half of a cycle was analyzed. Seven positions corresponding to ψ equal to 0, 30, 60, 90, 120, 150, and 180 degrees were analyzed. This required the analysis of 14 interferograms for each test since both vertical and horizontal gradients had to be determined. The end positions (ψ equal to 0 and 180 degrees) were

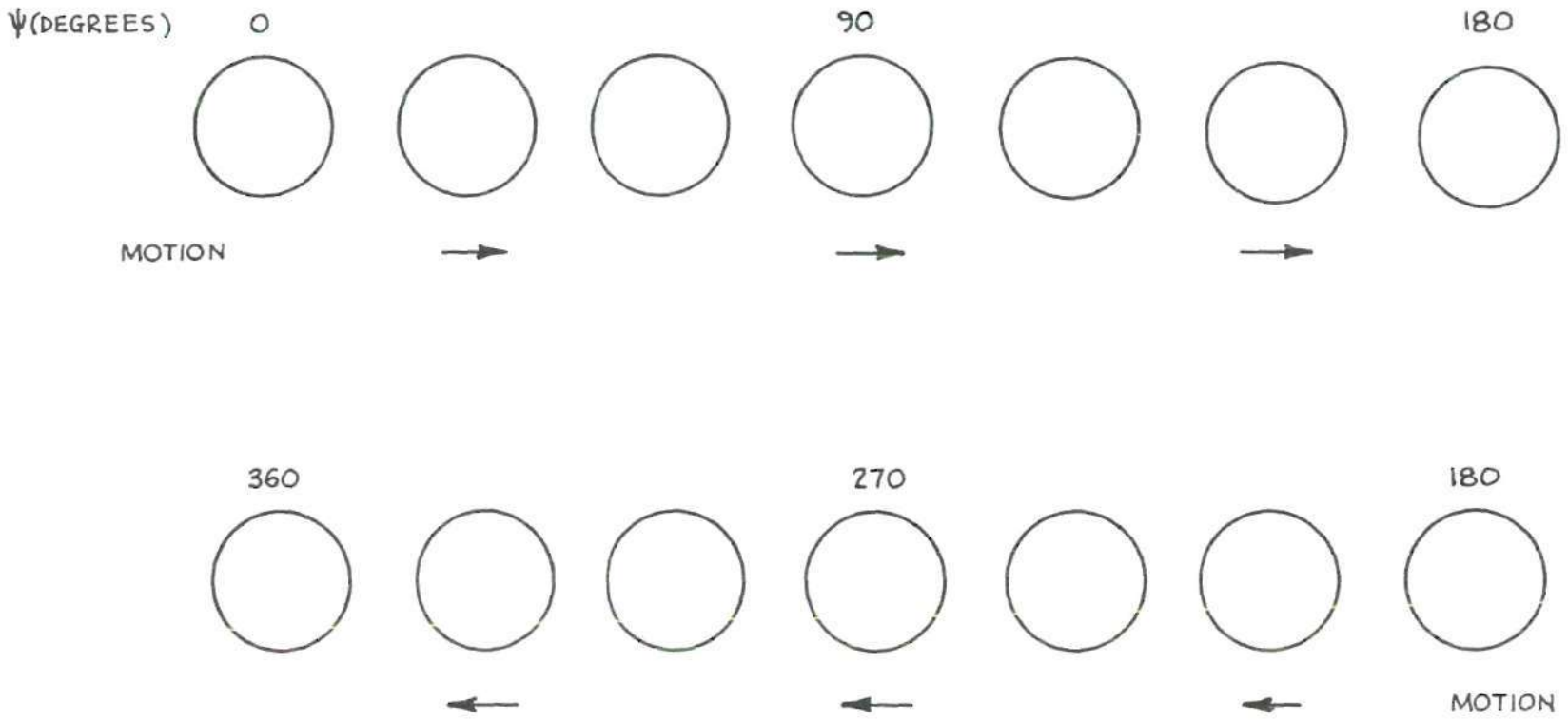

Figure 14. Schematic Diagram of One Oscillation of the Cylinder

located first. The amplitude of oscillation was calculated using the equation

$$A = \frac{D_{pb}(\psi=0°)-D_{pb}(\psi=180°)}{2M} \tag{45}$$

where D_{pb} is the distance measured from the right side of the cylinder to the plumb bob (measurements to the left of the plumb bob are taken as positive), and M is the magnification of the projected interferogram determined from the dividers in the test section.

The distance from the cylinder to the plumb bob is given by the expression

$$D_{pb}(\psi) = D_{pb}(\psi=0°)-AM(1-\cos\psi) \tag{46}$$

This equation was used to determine the cylinder positions for the five intermediate values of ψ. Since a film frame could not always be found which corresponded to the exact desired ψ position, the frame with the cylinder nearest the desired position was analyzed. The actual ψ position analyzed was determined by rewriting Equation (46) to give

$$\cos\psi = \frac{D_{pb}(\psi)-D_{pb}(\psi=0°)+AM}{AM} \tag{47}$$

The fringe shifts at the desired θ positions were obtained by interpolation from the seven measured positions.

For the seven positions of ψ, instantaneous, local Nusselt numbers, $Nu_v(\theta,\psi)$, were calculated from the fringe shift data using Equations (31), (36), and (44). These calculations were made for 15 degree increments in θ. At each position of ψ, an instantaneous, average Nusselt number, $Nu_v(\psi)$, was calculated by averaging the instantaneous, local values over the surface of the cylinder (integrated over θ). Similarly, an average, local Nusselt number, $Nu_v(\theta)$, was calculated at each θ position by averaging the instantaneous, local values over an entire cycle of oscillation (integrated over ψ). An overall average Nusselt number, $\overline{Nu}_v$, was calculated by averaging the instantaneous, average values over the entire cycle of oscillation. Simpson's rule was used to perform all of the numerical integrations. Similar to the stationary tests, a check on the interferometric measurement of the overall average Nusselt number was obtained by performing an energy balance on the cylinder.

All of the calculations for both the stationary and vibratory tests discussed above were performed by a computer program. A discussion of the computer program and calculations is presented in Appendix F. The heat-transfer results of the cylinder tests are presented in Chapter VII.

CHAPTER VII

RESULTS AND HEAT-TRANSFER CORRELATION

Stationary Tests

Introduction

The experimental tests that were conducted with the differential interferometer were organized in increasing complexity. Two steady state tests were performed before the transient measurements were made with the vibrating cylinder. The first steady state test was on a vertical flat plate while the second was on a stationary horizontal cylinder. These measurements were used to evaluate the accuracy, reproducibility, and reliability of the interferometer and the validity of the equations relating the fringe shift and heat-transfer coefficient. The two tests selected were ones for which heat-transfer coefficients are commonly measured so that published data was readily available on both. Successful duplication of these data in the two preliminary tests eventually verified the usefulness of the differential interferometer.

Flat Plate

The first steady state measurements were of the variation in the convective heat-transfer coefficient over a vertical flat plate which loses heat by free convection to

air. The variation of the free convective heat-transfer coefficient with distance x from the bottom edge of a vertical plate was calculated from measured fringe shifts. A plot of this variation is shown in Figure 15. The measurements shown were made for three different ray separation distances corresponding to Wollaston prism angles of 1, 3 and 8 degrees. These data indicate the reproducibility for different sensitivities of the system. Comparison is made with the analytical results of Ostrach [90]. Experimental results [39] obtained with a Mach-Zehnder interferometer for this case provided a correlation of local Nusselt numbers which is identical in form but less than 3 per cent below the theoretical results of Ostrach. The experimental values obtained with the differential interferometer show a maximum deviation of 5 and 8 per cent from the theoretical and experimental values, respectively.

Horizontal Cylinder

A series of free convective tests were performed with a stationary, horizontal cylinder to provide a basis for studying the effects of vibration on free convection. For each Grashof number, each test was repeated several times. The heat-transfer results of these tests were averaged to provide values for comparison with the vibrational tests. The variation of the convective heat-transfer coefficient around the cylinder was obtained in 15 degree increments in θ beginning with 0 degrees at the geometric bottom of cylinder.

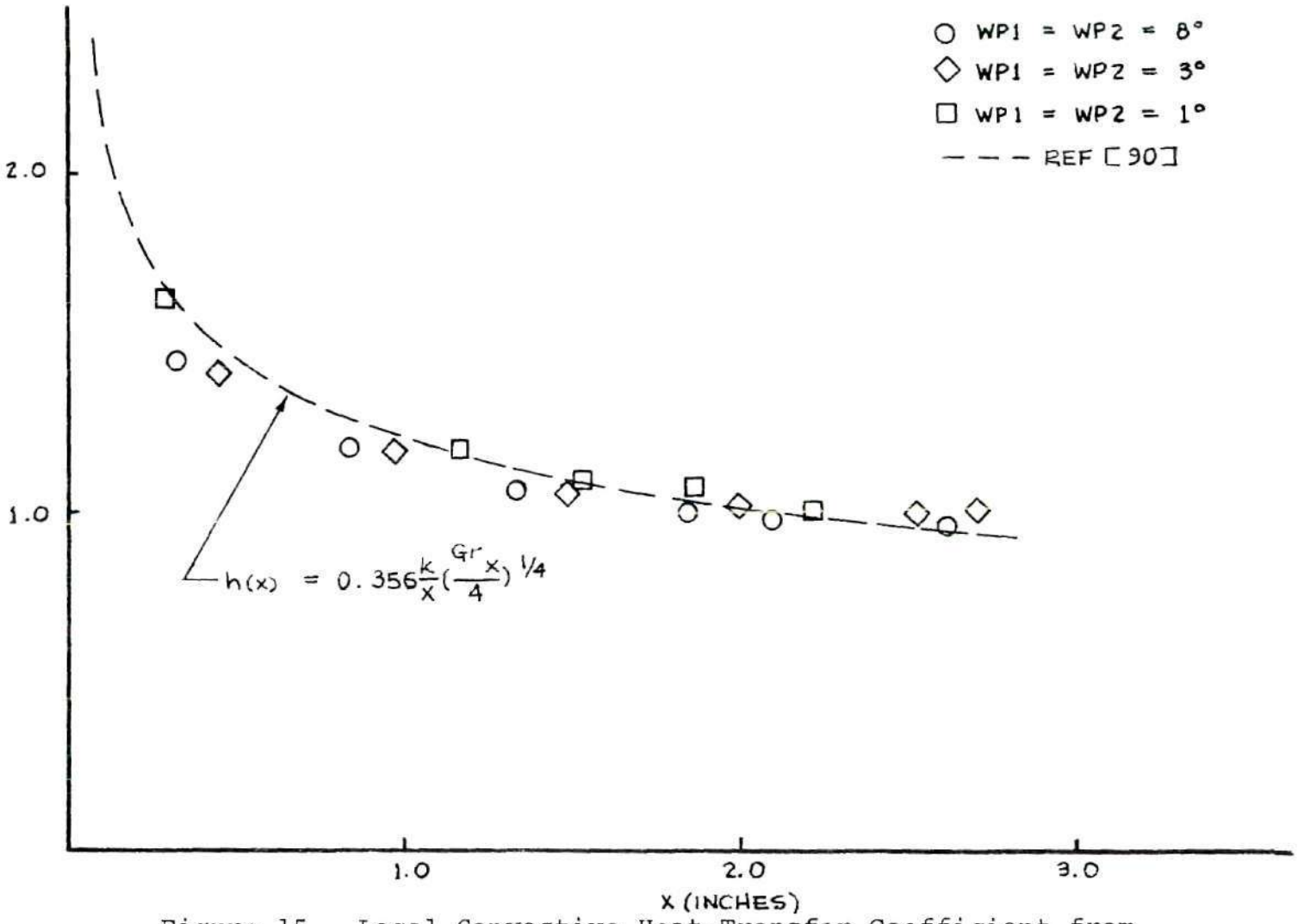

Figure 15. Local Convective Heat-Transfer Coefficient from a Vertical Isothermal Plate

The results of the stationary tests are plotted in Figure 16.

In Figure 17, the free convective results of one test are compared with the theoretical prediction of Herman [91] and the experimental results of Eckert and Soehngen [39]. The maximum deviation between the data and the results of Eckert and Soehngen is 10 per cent, but this difference occurs near the top of the cylinder where the heat flux is rapidly approaching a small value. Excluding this region the deviation is no more than 3 per cent.

The discrepancy between the data and the theoretical curve of Herman may be explained by the fact that theory assumes a boundary-layer thickness which is small compared to the diameter of the cylinder [39]. This assumption is not valid for the test plotted in Figure 17. The boundary-layer thickness measured from the infinite fringe photographs was found to be between one-quarter and one-third of the cylinder diameter for values of θ between 0 and 135 degrees.

Vibratory Tests

Important Dimensionless Numbers

For oscillatory flow imposed upon free convection, the Nusselt number is considered a function of several dimensionless parameters usually including Pr, Gr, and two other dimensionless groups which describe the vibration of the cylinder.

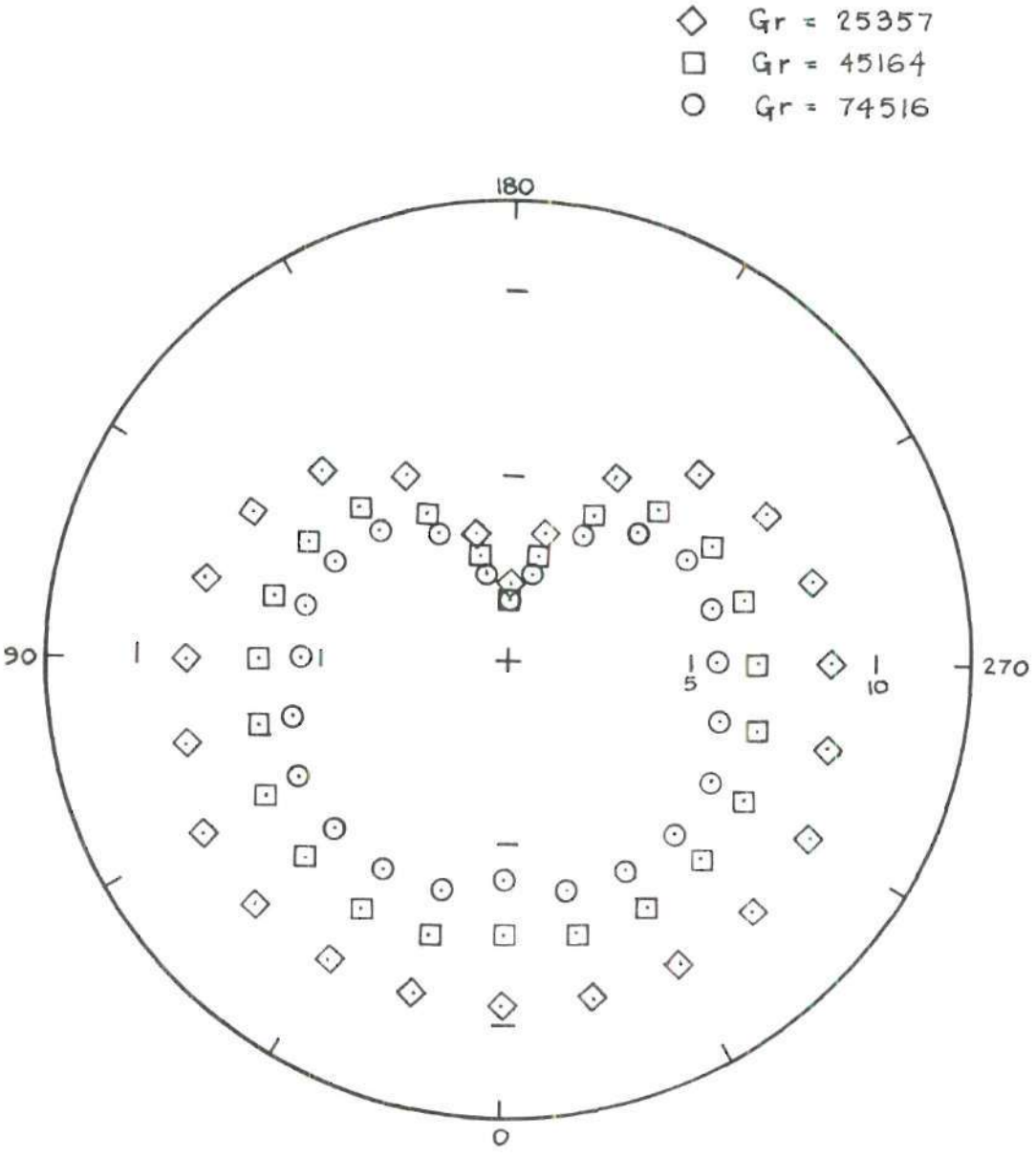

Figure 16. Local Variation of Nusselt Number for Stationary Tests

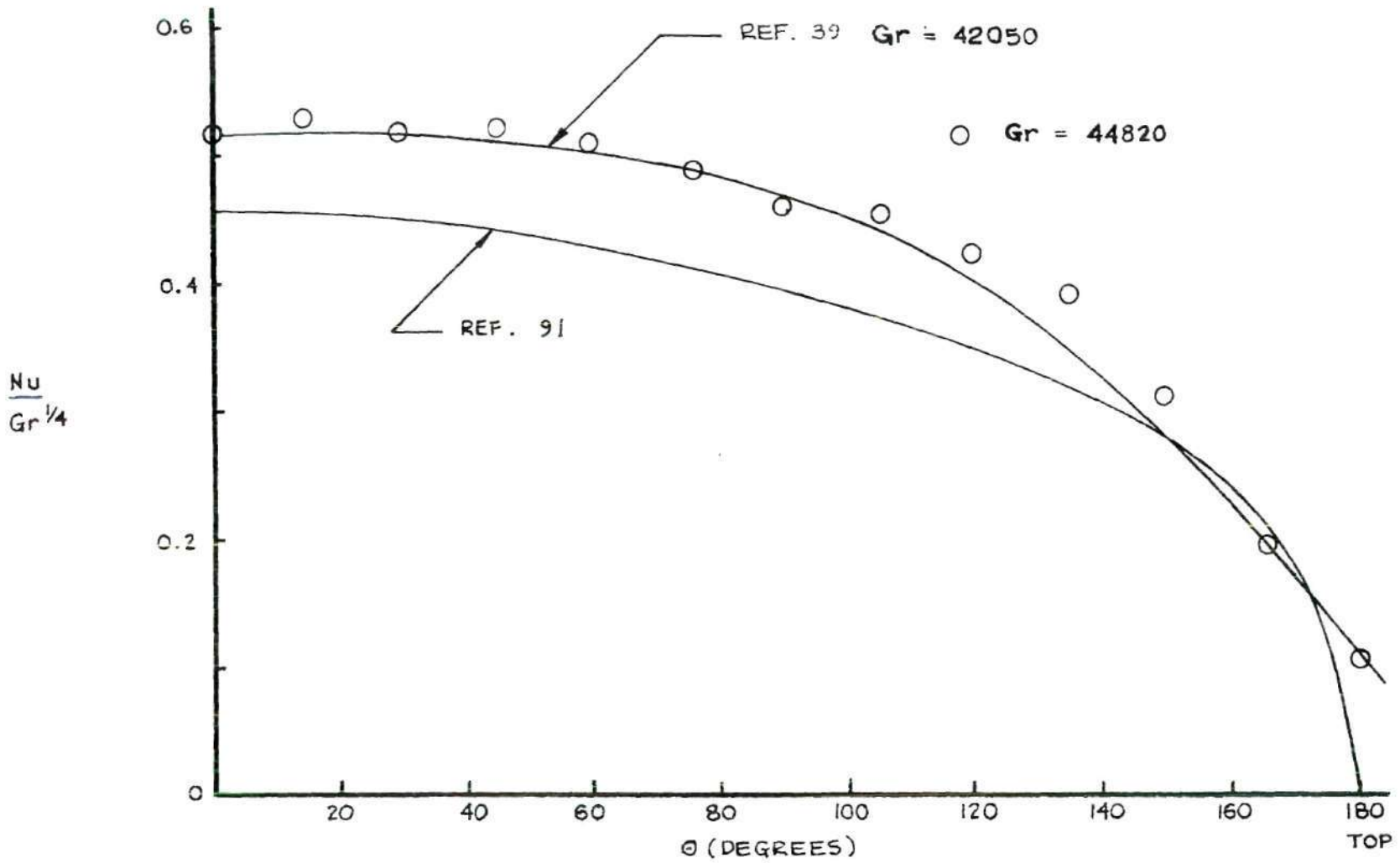

Figure 17. Local Free Convective Heat-Transfer Coefficient from a Horizontal Cylinder

$$Nu = Nu\ (Pr,\ Gr,\ 2\ \text{vibrational parameters}) \qquad (48)$$

The two dimensionless groups important in free convection which are common to most analyses are Pr and Gr. The Prandtl number can be considered a fluid parameter, and the Grashof number which is a ratio of buoyancy to viscous forces can be considered a temperature parameter.

The remaining two dimensionless groups describe the type of flow encountered when vibration is imposed on a free convective situation. Usually these parameters vary depending upon the investigation, but frequently one of the parameters selected is the ratio of amplitude of vibration to cylinder diameter, $\frac{A}{D}$, because this ratio is very significant in indicating the type of flow present during vibration.

The second dimensionless number is usually a Reynolds number; however, as many as four different forms of the Reynolds number have been suggested. An average Reynolds number, Re_A, that uses the average magnitude of the cylinder velocity, 4Af, as the characteristic velocity and the diameter of the cylinder, D, as the characteristic length has been suggested as one parameter.

$$Re_A = \frac{4AfD}{\nu} = \frac{2A\omega D}{\pi\nu} \qquad (49)$$

Similarly, an oscillatory Reynolds number, Re_{osc}, can be

formed using the root mean square magnitude of the cylinder velocity, $\frac{A\omega}{\sqrt{2}}$, as the characteristic velocity, and D as the characteristic length.

$$Re_{osc} = \frac{A\omega D}{\nu\sqrt{2}} \tag{50}$$

In oscillatory flow, motion exterior to the boundary layer is generated by Reynolds stresses associated with the primary boundary-layer flow. The magnitude of the velocity of the exterior flow is $\frac{A^2\omega}{D}$ [7] and can be used to form a third Reynolds number called the streaming Reynolds number, Re_s,

$$Re_s = \frac{(\frac{A^2\omega}{D})D}{\nu} = \frac{A^2\omega}{\nu} \tag{51}$$

A fourth Reynolds number used in vibrational heat transfer is a pure frequency parameter called the frequency Reynolds number

$$Re_{freq} = \frac{\omega D^2}{\nu} \tag{52}$$

The significance of Re_{freq} can be explained by using the a.c. boundary-layer thickness, δ_{ac}, which is the boundary-layer thickness associated with oscillatory flow. When a fluid oscillates relative to a solid surface, the fluid viscosity causes a region immediately adjacent to the solid in which the

velocity is different from the surrounding fluid. The thickness of this region is called the a.c. boundary-layer thickness, δ_{ac}, which is given by the expression [7]

$$\delta_{ac} = (\frac{\nu}{\omega})^{1/2} \tag{53}$$

where ν is the fluid kinematic viscosity, and ω is the circular frequency. Equation (52) for Re_{freq} can be rewritten as

$$Re_{freq} = [\frac{D}{(\frac{\nu}{\omega})^{1/2}}]^2 = (\frac{D}{\delta_{ac}})^2 \tag{54}$$

The streaming Reynolds number can also be interpreted in terms of the a.c. boundary-layer thickness. Equation (51) can be rewritten as

$$Re_s = (\frac{A}{\delta_{ac}})^2 \tag{55}$$

The four forms of the Reynolds number are related to each other through constants and powers of $\frac{A}{D}$. The average Reynolds number, Re_A, is related to the other Reynolds numbers by the equations

$$Re_A = \frac{2}{\pi} \frac{A}{D} Re_{freq} \tag{56}$$

$$Re_A = \frac{2}{\pi} \frac{D}{A} Re_s \tag{57}$$

$$Re_A = \frac{2\sqrt{2}}{\pi} Re_{osc} \tag{58}$$

Other dimensionless groups that have been used for describing the type of flow encountered when vibration is imposed on free convection can be formed by combining the Grashof number with the Reynolds number. One of these dimensionless numbers is $\frac{Re_s}{Gr^{1/2}}$. This parameter is a measure of the ratio of Reynolds stresses to buoyancy stresses [8]. Another is $(\frac{Re_{freq}}{Gr^{1/2}})^{1/2}$. The significance of this parameter can be shown by using Equation (54) to substitute for Re_{freq}.

$$(\frac{Re_{freq}}{Gr^{1/2}})^{1/2} = (\frac{(\frac{D}{\delta_{ac}})^2}{Gr^{1/2}})^{1/2} = \frac{\frac{D}{Gr^{1/4}}}{\delta_{ac}} \tag{59}$$

Since $\frac{D}{Gr^{1/4}}$ is a measure of the natural boundary-layer thickness, $(\frac{Re_{freq}}{Gr^{1/2}})^{1/2}$ is a measure of the ratio of the natural convective boundary-layer thickness to the a.c. boundary-layer thickness.

Combinations of Parameters

Lemlich [17] performed a dimensional analysis to show that the Nusselt number for a vibrating cylinder in free convection is a function of four dimensionless groups

$$Nu = Nu\ [Pr,\ Re_A,\ Gr,\ \frac{A}{D}] \tag{60}$$

Dougall et al. [92] have investigated this problem by writing the governing equations and boundary conditions in dimensionless form. Their analysis (see Appendix G for details) showed that the product Af is an important parameter for determining the magnitude of changes produced in the steady flow solution by the presence of harmonic oscillations. Examination of the dimensionless governing equations has shown that four dimensionless groups are needed to fully describe the flow. Four possible sets of parameters are presented in Table 7 in Appendix G. Since one set of these parameters contains the product Af, this set of dimensionless numbers is recommended as a promising combination. This combination of dimensionless numbers is identical with the set suggested by Lemlich [17] or

$$Nu = Nu\ [Pr,\ Gr,\ \frac{A}{D},\ Re_A] \tag{61}$$

Richardson [7] has discussed the controlling variables in oscillatory flow. The general oscillatory parameters presented were $\frac{A}{D}$, $\frac{1}{Re^2_{freq}}$, Re_{osc}, and Re_s. For oscillatory flow with natural convection, two additional parameters were recommended. These are $(\frac{Re_{freq}}{Gr^{1/2}})^{1/2}$ and $\frac{Re_s}{Gr^{1/2}}$.

Since the dimensionless groups suggested in references 17 and 92 are the parameters most often encountered in the literature, these parameters will be used in the discussion of the heat-transfer results in the following sections.

$$Nu = Nu(Pr, Gr, \frac{A}{D}, Re_A) \tag{62}$$

Instantaneous, Local Heat-Transfer

Instantaneous, local heat-transfer measurements (local values at one instant of time) were made for all of the vibrational tests. The results of these measurements are discussed in this section. First, the instantaneous, local measurements are compared with the corresponding free convective local measurements. Next, the effects of several parameters on the heat-transfer rate are discussed.

For each of seven ψ positions of 0, 30, 60, 90, 120, 150, and 180 degrees, the instantaneous, local Nusselt number, $Nu_V(\theta,\psi)$, was calculated at 15 degree increments in θ. All of the values of $Nu_V(\theta,\psi)$ were compared with the corresponding free convective local Nusselt number, $Nu_F(\theta)$, at the same θ position and Grashof number, and the percent difference between $Nu_V(\theta,\psi)$ and $Nu_F(\theta)$ was computed. Maximum and minimum per cent differences are tabulated in Table 2 for several representative tests. Each data point presented in Table 2 is for a single run and is subject to the reproducibility error discussed in a later section. For given values

Table 2. Maximum and Minimum Per Cent Changes in $Nu_V(\theta,\psi)$ Relative to $Nu_F(\theta)$

MAXIMUMS

Re_A	Gr	$\frac{A}{D}$	θ	ψ	Per Cent Change
137	74429	0.5132	195	120	200
147	46183	1.7693	180	30	280
155	25517	1.7818	180	60	350
278	74602	0.5203	180	90	430
296	46419	1.7764	180	30	700
316	25761	1.8146	180	60	570
586	44989	0.5102	180	90	1260
660	24956	0.4121	180	90	1400

MINIMUMS

Re_A	Gr	$\frac{A}{D}$	θ	ψ	Per Cent Change
129	73551	0.1216	150	150	-53
141	25321	0.1179	150	150	-68
147	46183	1.7693	270	0	-82
264	74074	0.9910	150	90	-71
279	45025	0.2431	135	150	-76
316	25715	0.3941	135	120	-60
586	45643	1.7764	60	60	-50
660	24956	0.4121	60	120	-54

of Re_A and Gr, the largest positive and negative per cent differences between $Nu_V(\theta,\psi)$ and $Nu_F(\theta)$ are given along with the values of $\frac{A}{D}$, θ, and ψ. The largest instantaneous, local increase was approximately 1400 per cent, and the largest instantaneous, local decrease was approximately 82 per cent.

In Figure 18, plots of the local Nusselt number as a function of θ for forced convection reported by Eckert and Soehngen [42] are shown so that trends in the variation of the local Nusselt number produced by a forced flow can be compared with the variation in local Nusselt number due to sinusoidal vibration of the cylinder in still air.

The results of several tests are presented in Figures 19 through 26 to illustrate the effect of vibration on $Nu_V(\theta,\psi)$. Each figure consists of eight plots illustrating the variation of $Nu_V(\theta,\psi)$ with position around the cylinder surface. Seven of the plots correspond to seven different ψ locations while the eighth plot shows the local Nusselt number for a stationary cylinder.

$\frac{A}{D}$ Effect. Figures 19, 20, and 21 show the effect of varying $\frac{A}{D}$ on $Nu_V(\theta,\psi)$ for a Grashof number of approximately 2.5×10^4 and an average Reynolds number of approximately 150. By comparing the seven vibratory plots with the single stationary plot in Figure 19, it can be seen that the effect of vibration on $Nu_V(\theta,\psi)$ was very small for $\frac{A}{D}$ of 0.1179, and the $Nu_V(\theta,\psi)$ curves resemble very closely the free convective curve both in shape and magnitude particularly at $\psi = 60$

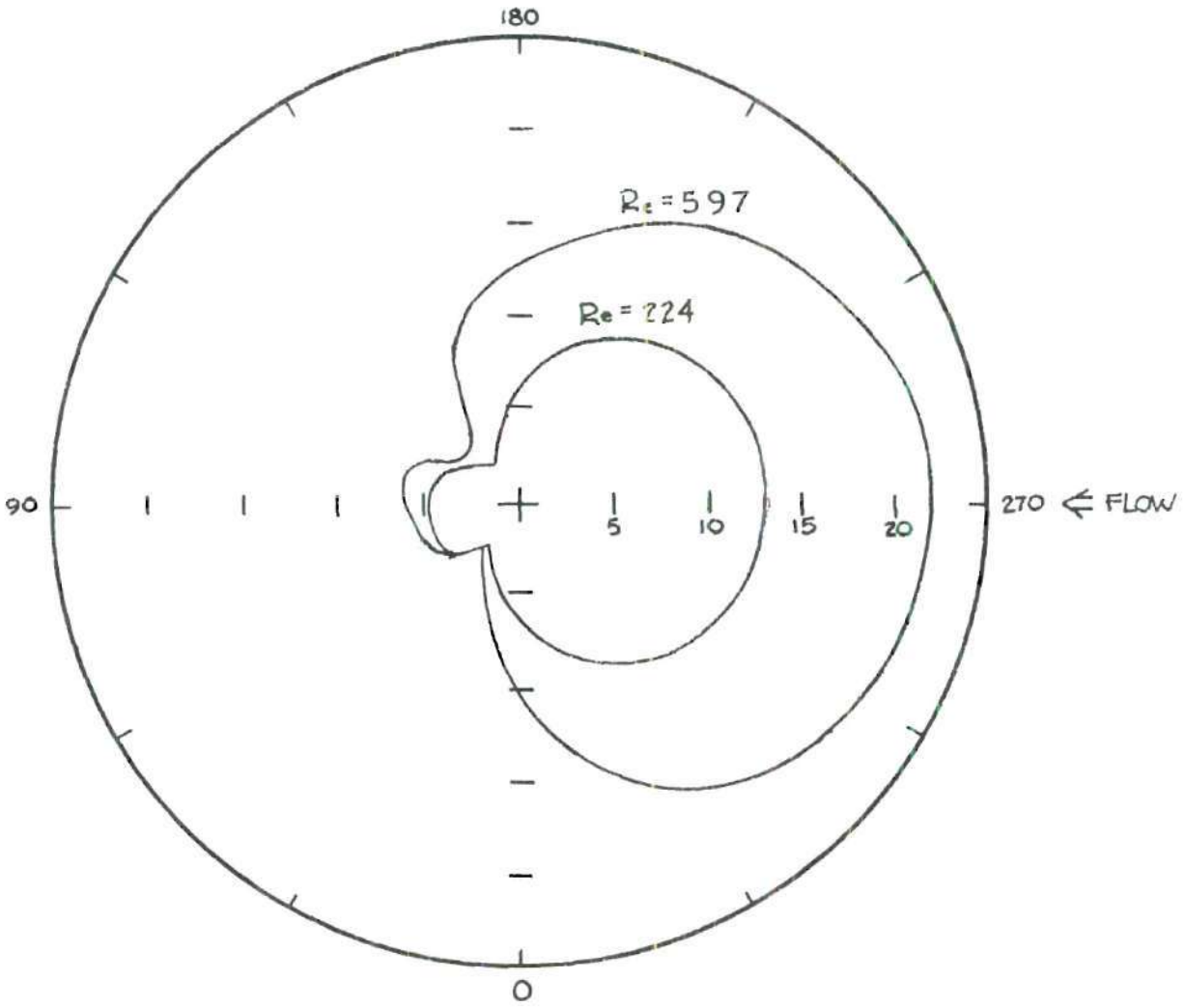

Figure 18. Distribution of Local Nusselt Number Around Circumference of Circular Cylinder for Forced Convection [42]

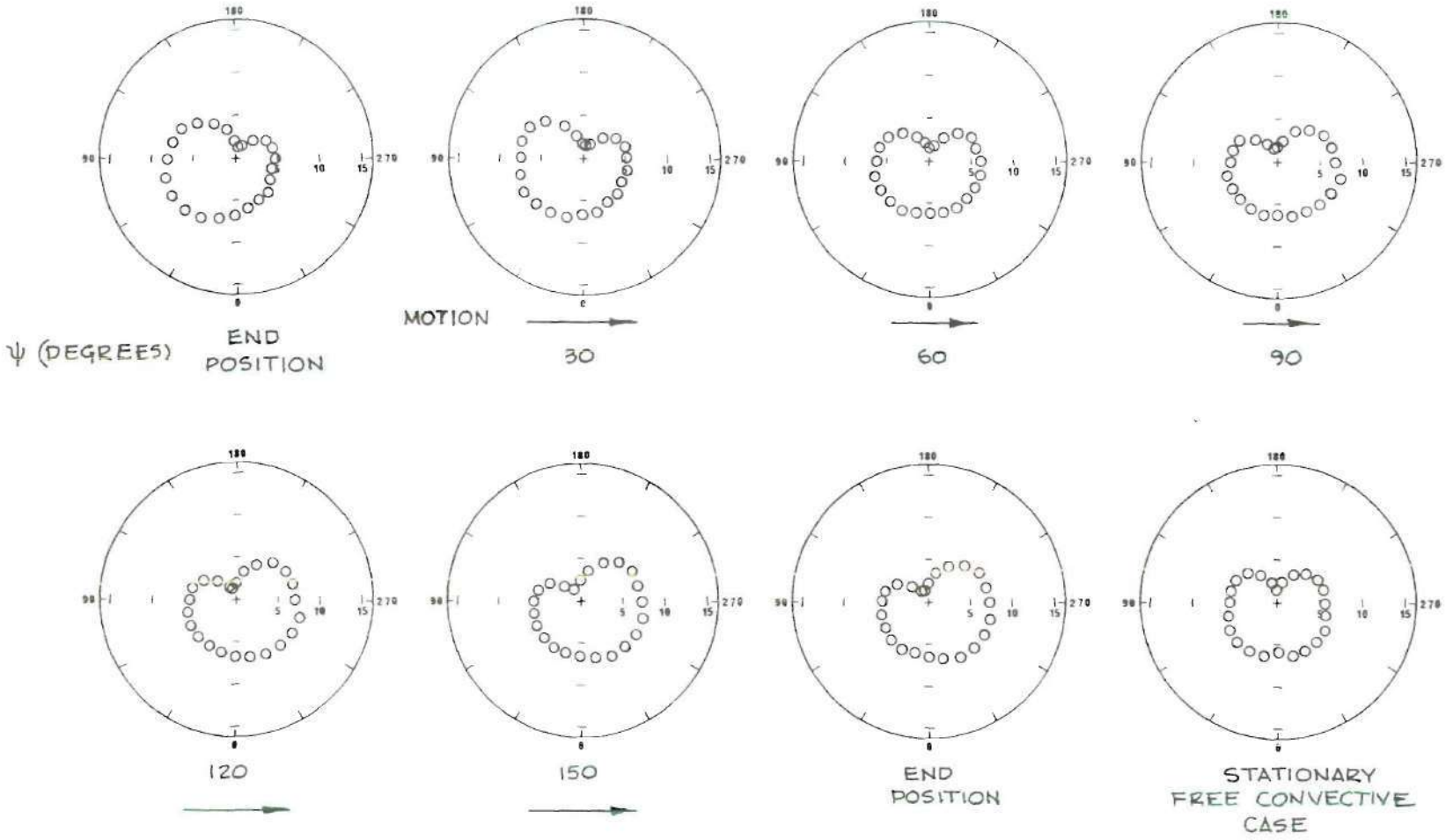

Figure 19. Distribution of $Nu_v(\theta,\psi)$ with θ for $\frac{A}{D} = 0.1179$, $Re_A = 141$, and $Gr = 25,321$

degrees. At other ψ positions, the $Nu_v(\theta,\psi)$ curves are similar to the free convective curve but appear to have been rotated slightly with θ. At a ratio of amplitude to diameter of 0.2368, the effect due to vibration was also insignificant.

In Figure 20, the effect of vibration at $\frac{A}{D}$ of 0.5007 is much more pronounced. The shapes of the $Nu_v(\theta,\psi)$ plots resemble the forced convective plots (Figure 18) for all ψ positions except 30 and 60 degrees. At ψ equal to 30 degrees, the shape of the plot resembles the free convective plot. At ψ equal to 60 degrees, the plot has both free and forced convective characteristics since the shape of the curve resembles the shape of the free convective curve, but similar to forced convection, $Nu_v(\theta,\psi)$ on the leading half of the cylinder is larger than $Nu_v(\theta,\psi)$ on the trailing half.

The plots for $\frac{A}{D}$ of 1.7818 are shown in Figure 21. The main difference between the plots for $\frac{A}{D}$ of 0.5007 and 1.7818 is at ψ positions of 30 and 60 degrees. For $\frac{A}{D}$ of 1.7818 and ψ of 60 degrees, the polar plot of $Nu_v(\theta,\psi)$ resembles the forced convective plots. The $Nu_v(\theta,\psi)$ plot at ψ of 30 degrees has both free and forced convective characteristics similar to the $Nu_v(\theta,\psi)$ plot for $\frac{A}{D}$ of 0.5007 at ψ of 60 degrees.

The differences in the plots of $Nu_v(\psi)$ at ψ = 30 and 60 degrees are due to the fact that the frequency of oscillation is higher for the test run at $\frac{A}{D}$ = 0.5007, and the acceleration of the cylinder is higher. Thus, the cylinder

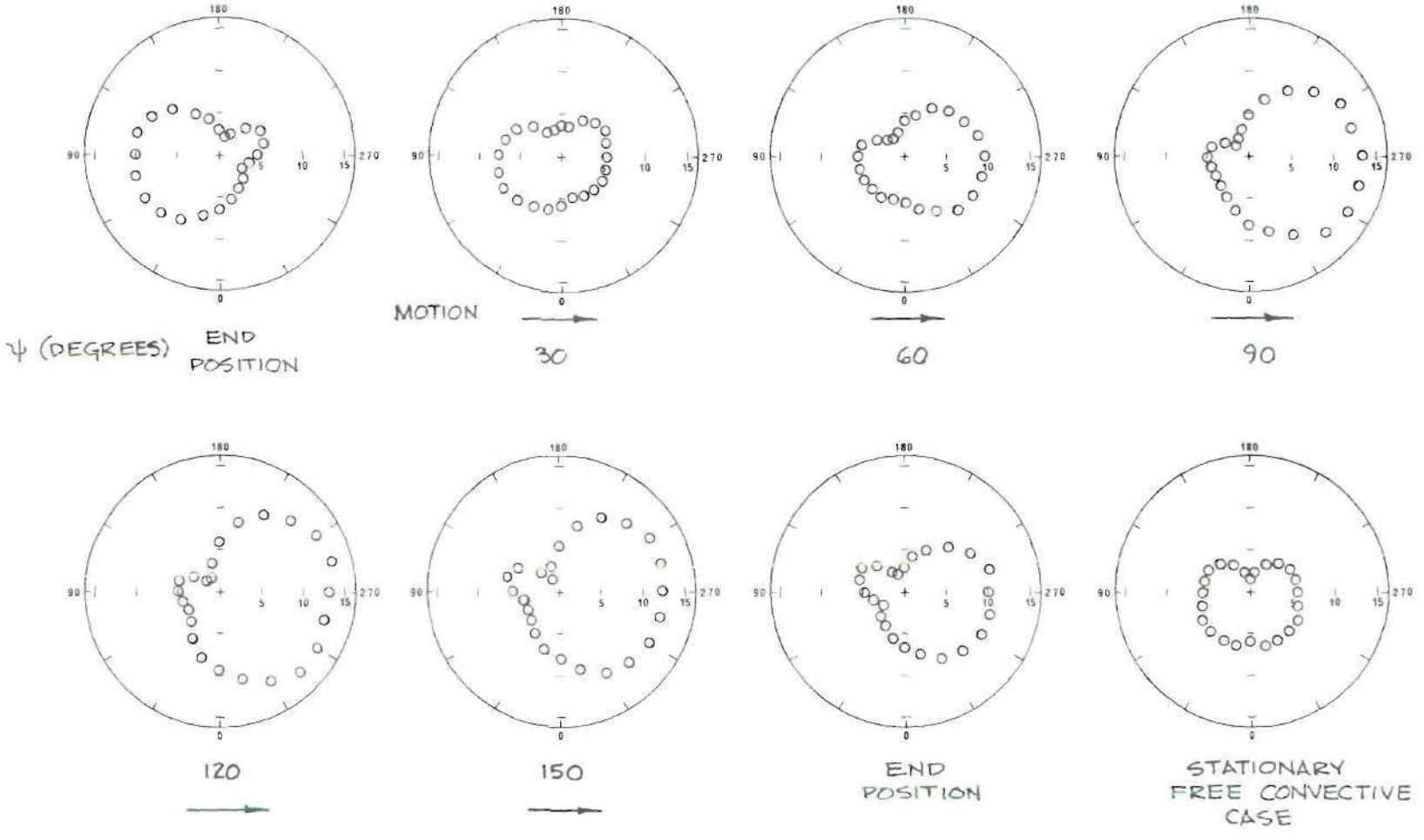

Figure 20. Distribution of $Nu_v(\theta,\psi)$ with θ for $\frac{A}{D} = 0.5007$, $Re_A = 151$, and $Gr = 25{,}590$

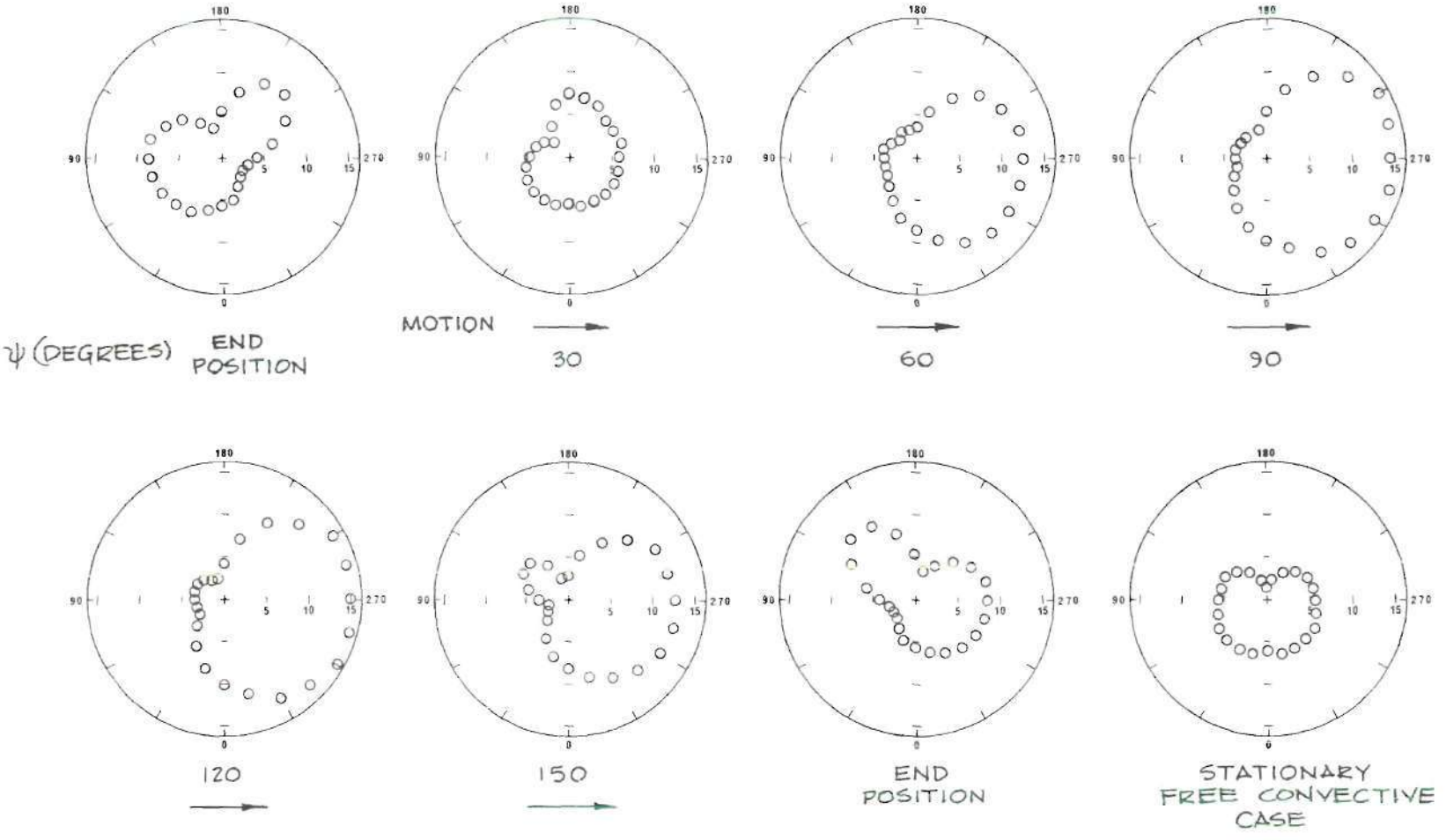

Figure 21. Distribution of $Nu_v(\theta,\psi)$ with θ for $\frac{A}{D} = 1.7818$, $Re_A = 155$, and $Gr = 25{,}517$

changes direction more quickly at the extreme position of oscillation, and the air heated in the previous half cycle of oscillation has less time to rise out of the cylinder's path. Therefore, the heat transfer from the cylinder is more affected by the previous half cycle of oscillation.

Figures 22 and 23 show the effect of $\frac{A}{D}$ at higher average Reynolds numbers (Re_A approximately 615). Notice that the shapes of the $Nu_v(\theta,\psi)$ plots are quite different at the extreme positions and also at ψ = 30 degrees. This is due to the frequency effect discussed previously. For ψ positions toward the center of oscillation, the $Nu_v(\theta,\psi)$ plots resemble forced convective plots for both ratios of amplitude to diameter. Generally, the magnitude of $Nu_v(\theta,\psi)$ is greater for $\frac{A}{D}$ of 1.7760.

Re_A Effect. Figures 20, 22, and 24 show the effect of increasing Re_A from approximately 150 to 600 at a Grashof number of approximately 2.5×10^4 and an $\frac{A}{D}$ of approximately 0.5. The main effect of increasing Re_A was an increase in the magnitude of $Nu_v(\theta,\psi)$. The shapes of the curves for a given ψ position were not drastically altered as Re_A changed even though the magnitude of $Nu_v(\theta,\psi)$ increased with the Reynolds number.

Figures 22 and 24 show clearly that as the cylinder passed through the midpoint in an oscillation (ψ=90 degrees), the Nusselt number in the vicinity of the wake of the cylinder (θ=90 degrees) increased even though the velocity of the

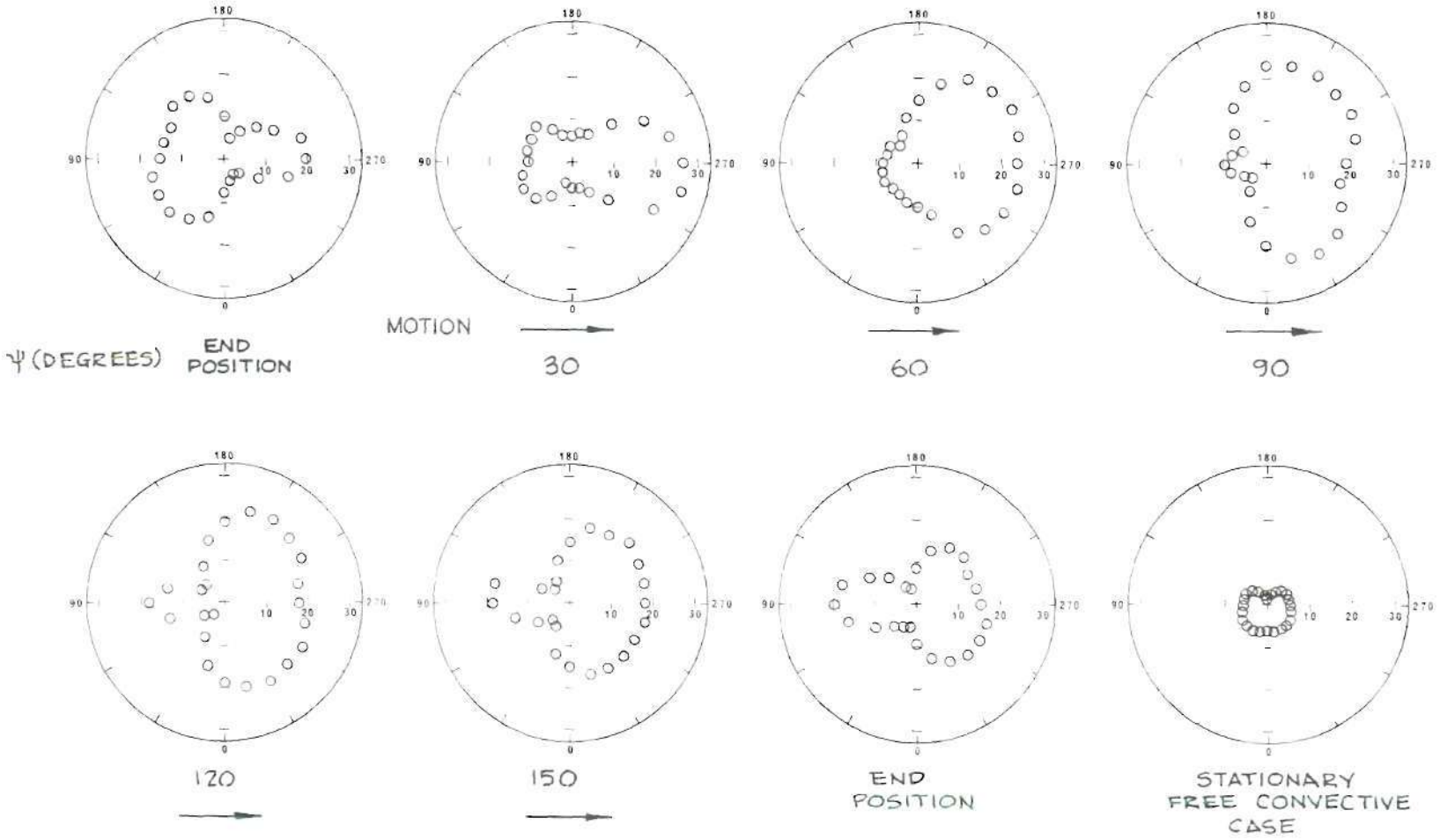

Figure 22. Distribution of $Nu_v(\theta,\psi)$ with θ for $\frac{A}{D} = 0.5182$, $Re_A = 617$, and $Gr = 24{,}902$

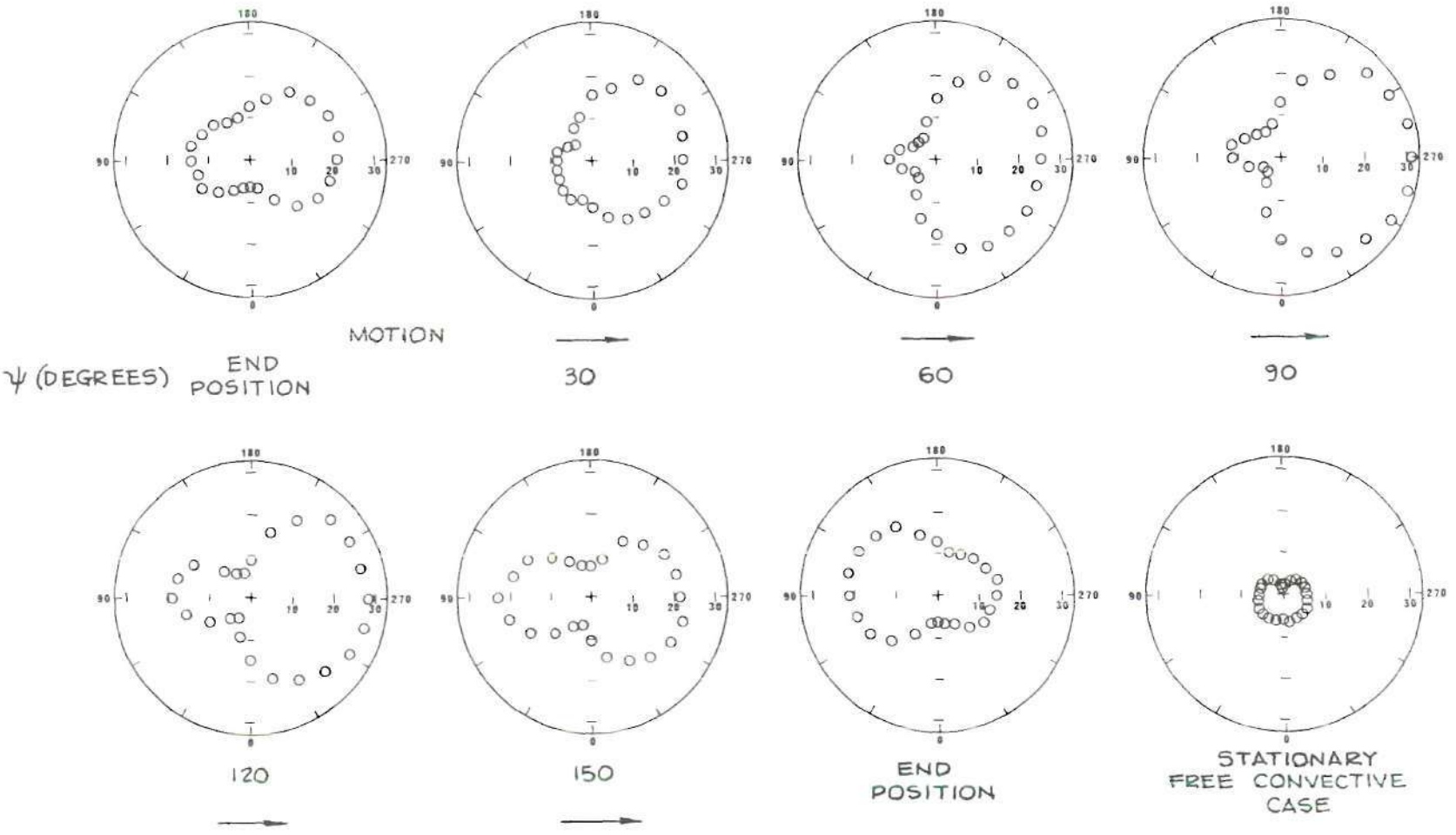

Figure 23. Distribution of $Nu_v(\theta,\psi)$ with θ for $\frac{A}{D} = 1.7760$, $Re_A = 610$, and $Gr = 25{,}469$

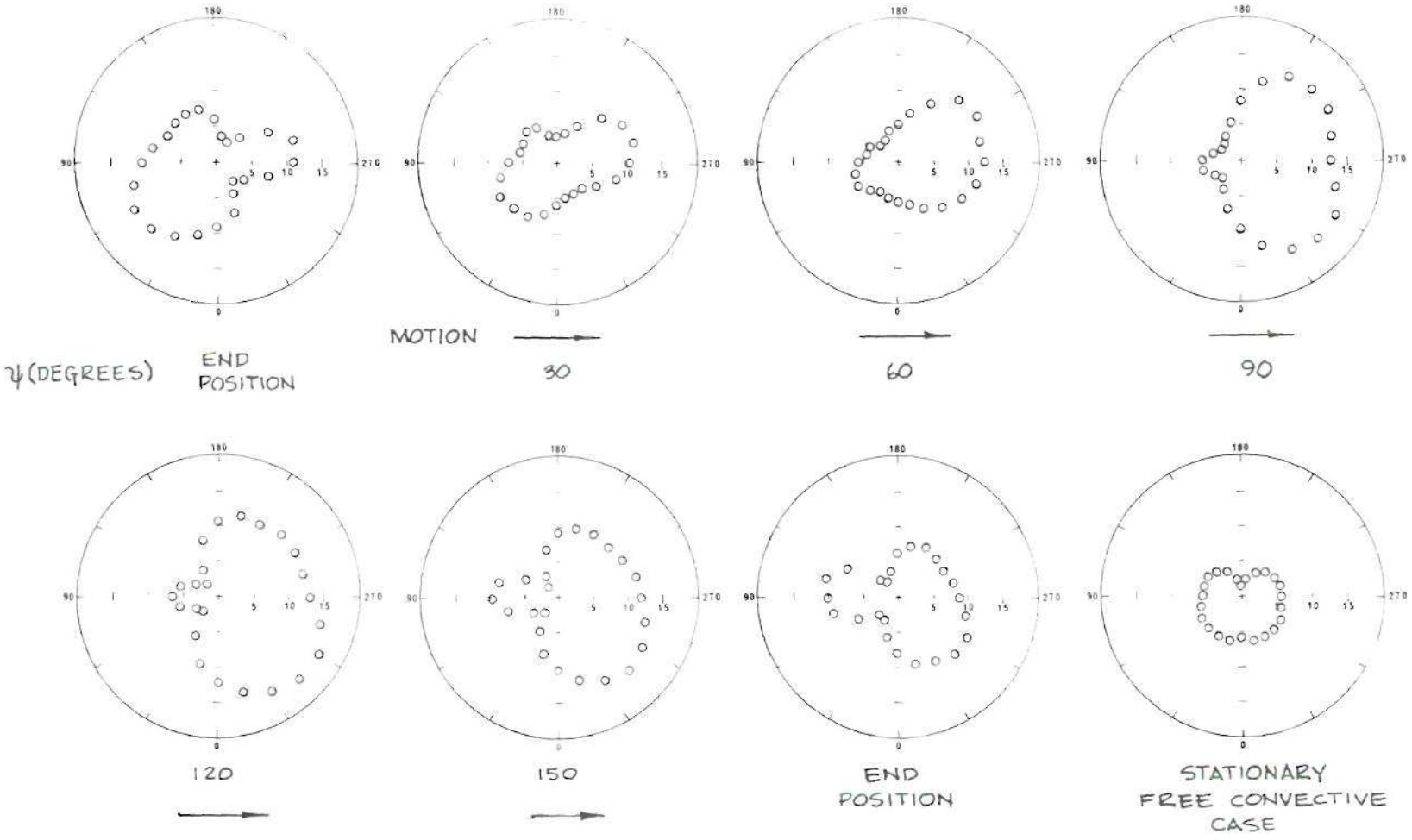

Figure 24. Distribution of $Nu_v(\theta,\psi)$ with θ for $\frac{A}{D} = 0.5071$, $Re_A = 304$, and $Gr = 25{,}207$

cylinder was decreasing. This trend was not expected because in pure forced flow, there is a region of relatively low heat transfer at the rearward side of the cylinder such as shown in Figure 18. Observation of the infinite fringe motion pictures indicated that due to the deceleration of the cylinder at the higher speeds, the flow separations on the trailing side of the cylinder moved toward the cylinder causing vigorous circulation in the wake that increased the heat-transfer rate on the trailing side of the cylinder.

Gr Effect. Figures 20, 25, and 26 demonstrate the effect of increasing Gr from approximately 2.5×10^4 to 7.4×10^4 at a Re_A of approximately 145 and an $\frac{A}{D}$ of approximately 0.5. The magnitude of $Nu_v(\theta,\psi)$ was larger for larger Gr, but the effect of Gr on $Nu_v(\theta,\psi)$ was much larger at the end points (ψ = 0, 180 degrees), as expected, since $\frac{Re^2_v(\psi)}{Gr}$ was zero at these points, and the free convective forces predominated at the end regions. On the other hand, the magnitude effect of Gr was much smaller for the intermediate ψ positions where $\frac{Re^2_v(\psi)}{Gr}$ was greater than zero, and inertial forces were important. Notice that in Figure 25 at ψ equal to 30 degrees, the shape of the curve resembles very closely the free convective curve, but at the center of the oscillation (ψ=90 degrees), the curve resembles the force convective curve.

Instantaneous, Average Heat Transfer

Instantaneous, average Nusselt numbers (average values

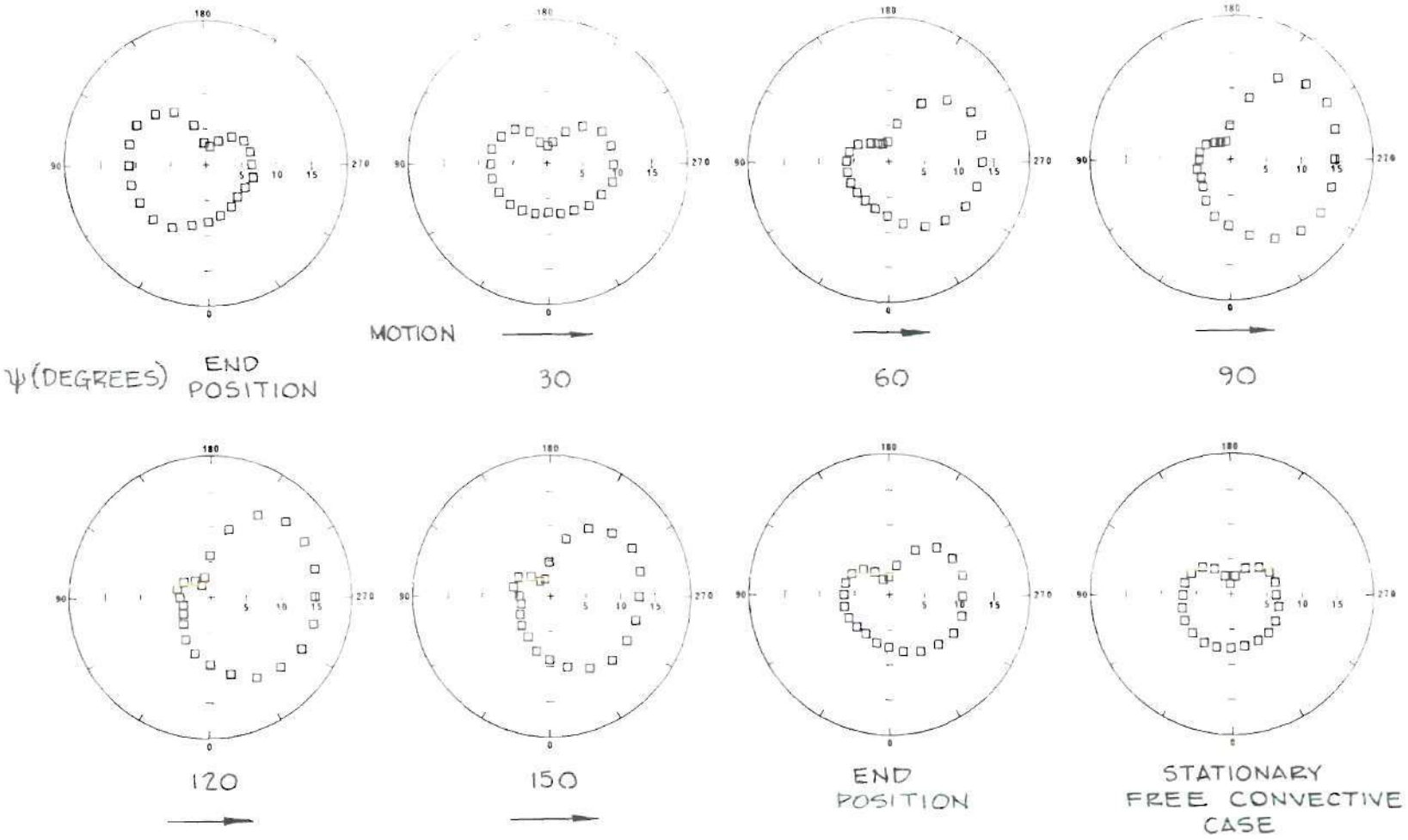

Figure 25. Distribution of $Nu_v(\theta,\psi)$ with θ for $\frac{A}{D} = 0.5198$, $Re_A = 148$, and $Gr = 44{,}025$

Figure 26. Distribution of Nu_v (θ,ψ) with θ for $\frac{A}{D} = 0.5132$, $Re_A = 137$, and $Gr = 74,429$

at one instant of time), $Nu_v(\psi)$, were calculated for all of the vibratory tests by averaging the instantaneous, local Nusselt numbers over the entire cylinder surface. In this section, values of $Nu_v(\psi)$ are compared with the corresponding free convective Nusselt numbers, and then the effects of the parameters, $\frac{A}{D}$, Re_A, and Gr, on $Nu_v(\psi)$ are discussed. Finally, $Nu_v(\psi)$ at the mid point of oscillation (ψ=90 degrees) is compared with forced and mixed free-forced convective Nusselt numbers at the same Reynolds numbers.

Values of $Nu_v(\psi)$ were calculated for the seven values of ψ of 0, 30, 60, 90, 120, 150, and 180 degrees. In order to obtain some measurement as to how effective vibration was in increasing the heat-transfer rate from a cylinder, $Nu_v(\psi)$ was compared with the average free convective Nusselt number, $\overline{Nu}_F$. The per cent difference between $Nu_v(\psi)$ and $\overline{Nu}_F$ was computed, and maximum and minimum per cent differences are tabulated in Table 3 for several representative tests. Each data point presented in Table 3 is for a single run and is subject to the reproducibility error discussed in a later section. The largest instantaneous increase was 240 per cent and the largest instantaneous decrease was 4 per cent.

Several figures showing the variation in the instantaneous average Nusselt number with $\frac{A}{D}$, Gr, and Re_A are presented to demonstrate the effect of these parameters on the instantaneous heat-transfer rates. For the two values of Re_A of approximately 150 and 300 and for the three values of

Table 3. Maximum and Minimum Per Cent Changes in $Nu_V(\psi)$ Relative to $\overline{Nu}_F$

MAXIMUMS

Re_A	Gr	$\frac{A}{D}$	ψ (degrees)	Nu_{inst}	Per Cent Change
147	24525	0.9894	90	9.2	74
145	46888	0.9963	90	9.5	50
137	74429	0.5132	120	10.8	37
294	24505	0.9948	90	11.8	120
288	45827	0.9959	90	14.4	130
264	74074	0.9910	90	13.3	69
610	25469	1.7760	90	17.9	240
580	45315	1.0046	90	18.5	200

MINIMUMS

Re_A	Gr	$\frac{A}{D}$	ψ (degrees)	Nu_{inst}	Per Cent Change
142	25306	0.2368	60	5.3	- 1
136	44820	0.1191	60	6.3	+ 0
137	74988	1.7765	0	7.6	- 4
283	25138	0.2378	60	5.5	+ 3
279	45025	0.2431	60	6.1	- 2
267	74411	0.2508	60	7.9	+ 1
660	24956	0.4121	30	11.9	+120
580	45315	1.0046	30	12.5	+ 99

Gr of approximately 2.5×10^4, 4.4×10^4, and 7.4×10^4, the plots of $Nu_v(\psi)$ showed a distinct variation with $\frac{A}{D}$. The trends in these variations can be seen in Figure 27. At low $\frac{A}{D}$, the minimum values of $Nu_v(\psi)$ were in the vicinity of ψ = 60 degrees, but as $\frac{A}{D}$ increased, the minimum moved toward lower values of ψ until it was between 0 and 30 degrees. The ψ position of the maximum value of $Nu_v(\psi)$ also varied with $\frac{A}{D}$. At low $\frac{A}{D}$, the ψ position of the maximum was between 150 and 180 degrees, but as $\frac{A}{D}$ increased, the ψ position of the maximum moved toward the center of oscillation until the maximum was near ψ = 90 degrees.

The effect of Re_A on $Nu_v(\psi)$ is shown in Figure 28. The value of $Nu_v(\psi)$ increased at all ψ positions as Re_A was increased, and the largest increase in $Nu_v(\psi)$ occurred in the vicinity of ψ of 90 degrees where $Re_v(\psi)$ was near its maximum value. The value of $Nu_v(\psi)$ at ψ = 0 degrees increased with increasing Re_A even though $Re_v(\psi)$ was zero at this position. This increase in heat dissipation was due to the fact that there was relative motion between the air and the cylinder at the end of the stroke of oscillation even though the velocity of the cylinder was zero. The motion of the cylinder throughout the cycle caused air to be carried along the cylinder, and this air moved relative to the cylinder when the cylinder stopped. At high Re_A, this motion appeared to be fairly turbulent.

Figure 29 demonstrates the effect of varying Gr on

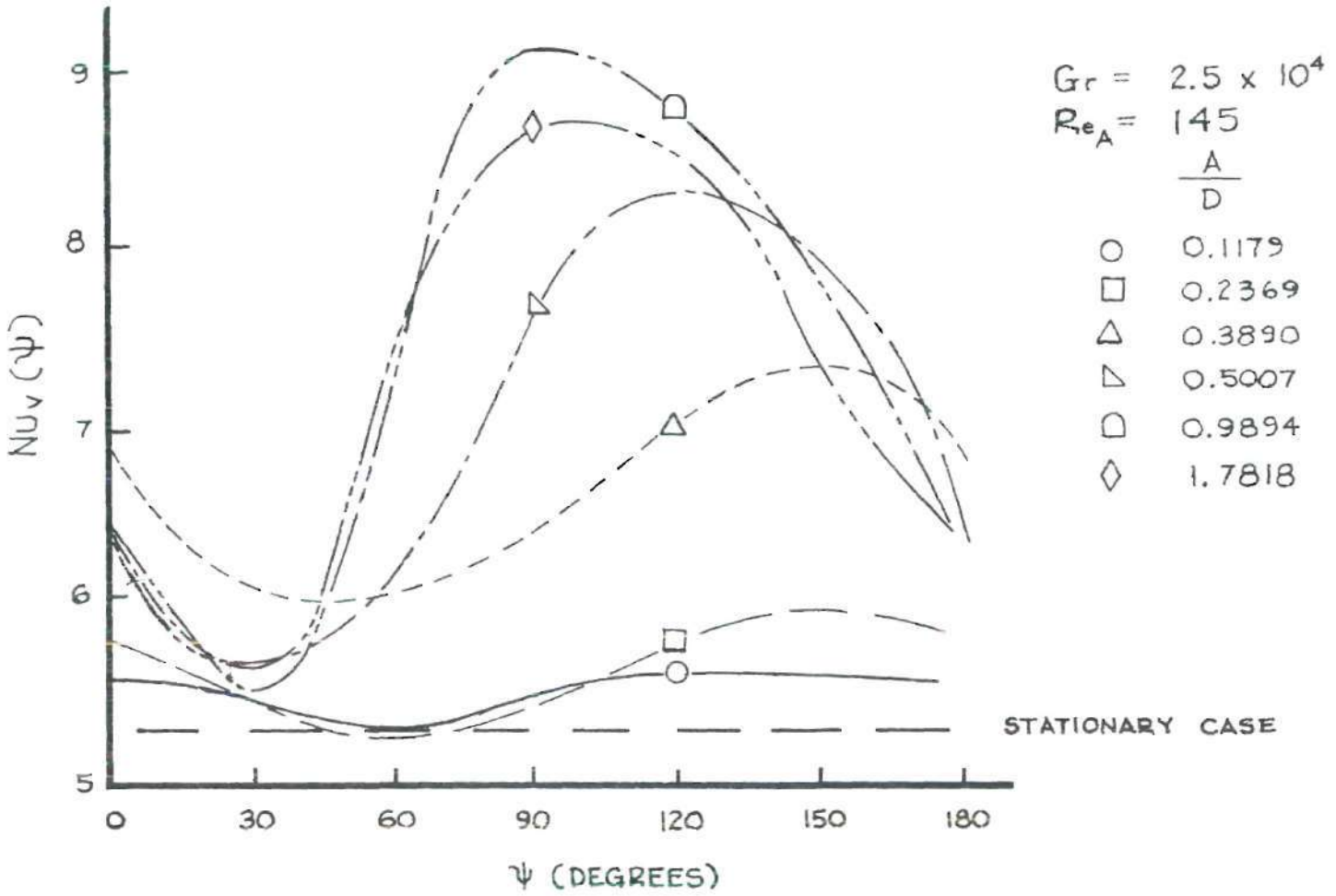

Figure 27. Variation in Instantaneous Average Nusselt Number, $Nu_v(\psi)$, with the Amplitude to Diameter Ratio, $\frac{A}{D}$

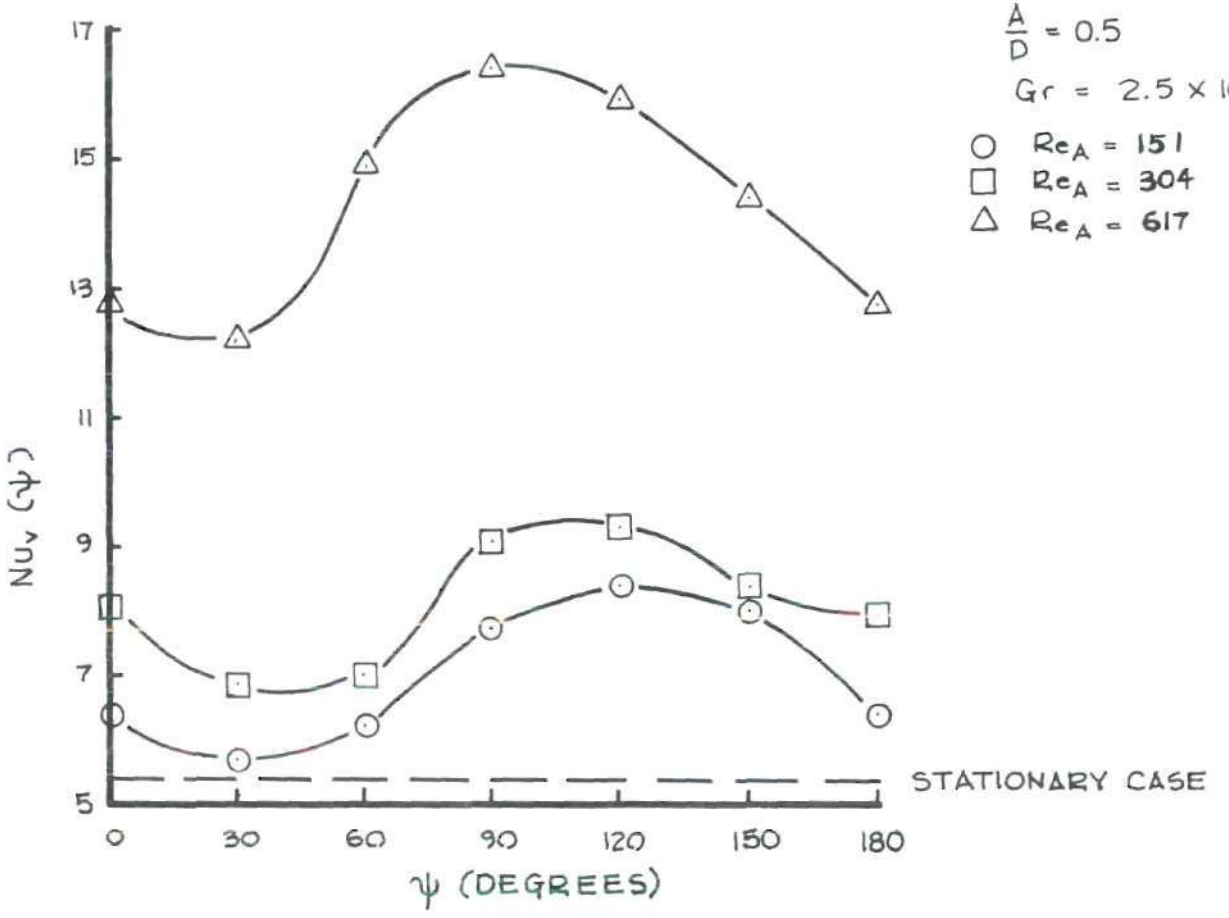

Figure 28. The Effect of Increasing Re_A on $Nu_V(\psi)$

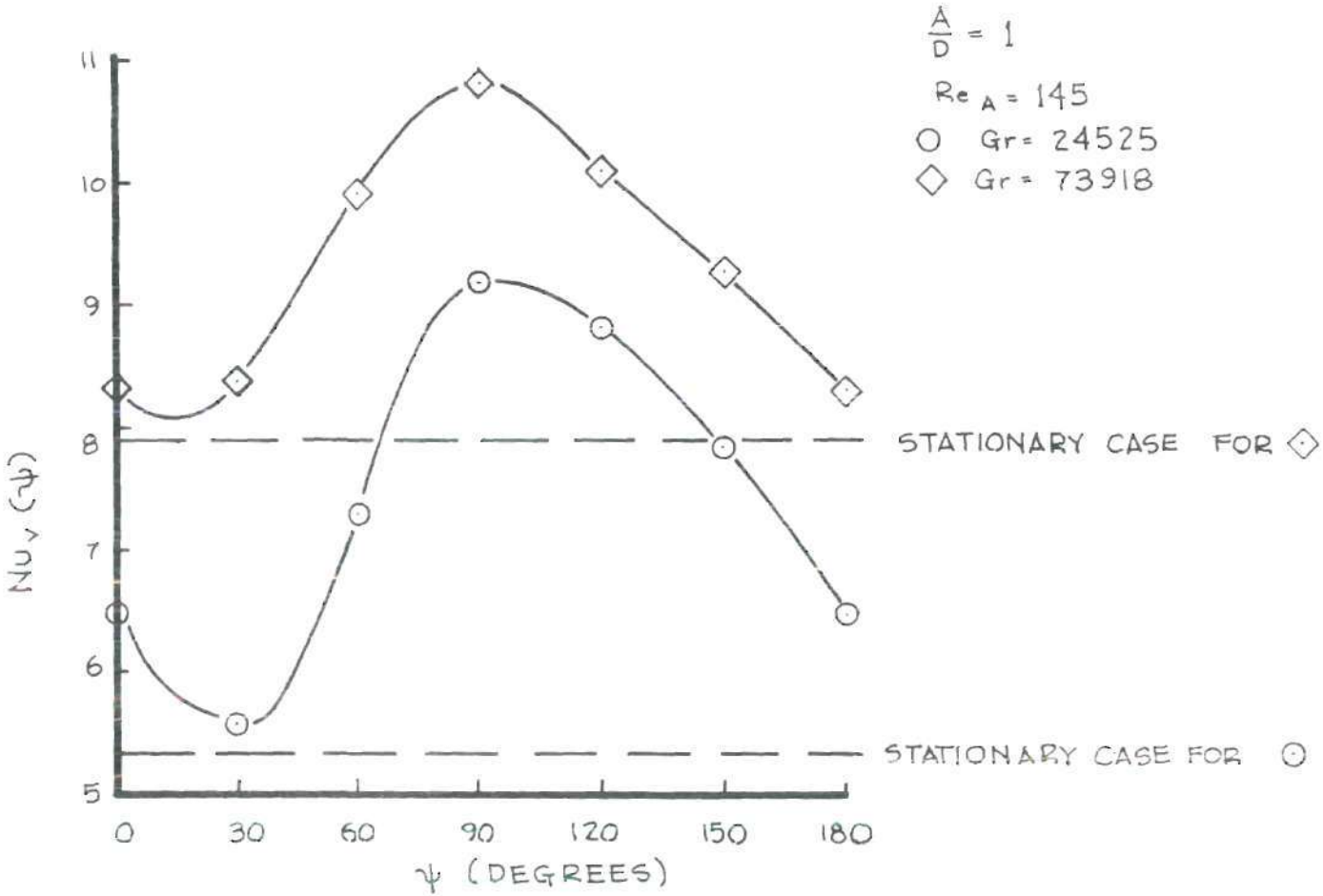

Figure 29. The Effect of Increasing Gr on $Nu_v(\psi)$

$Nu_v(\psi)$. All values of $Nu_v(\psi)$ increased with increasing Gr, but the value of $Nu_v(\psi)$ for Gr equal to 24525 was more affected by vibration than $Nu_v(\psi)$ at the larger Gr. The effect of Gr was smallest in the vicinity of ψ = 90 degrees and was largest in the vicinity of the end points. This effect can be explained by considering the ratio $\frac{Re^2_v(\psi)}{Gr}$ which is a measure of the ratio of vibrational forces to buoyancy forces. The value of $\frac{Re^2_v(\psi)}{Gr}$ was largest at ψ = 90 degrees and was zero at the end points. This indicates that the vibrational forces were strongest at ψ = 90 degrees and weakest at ψ = 0 degrees. Thus, the buoyancy forces predominated at the end points and were less dominant at the center of oscillation.

In Figures 30, 31, and 32, values of $Nu_v(\psi)$ at the center of oscillation (ψ=90 degrees) are compared with both forced convective curves [93, 94] and free-forced convective curves [95]. The Reynolds number used is $Re_v(\psi)$. In general, values of $Nu_v(\psi)$ lie below both correlations for low values of $\frac{A}{D}$. Two exceptions of this general statement appear in Figure 32. For Gr = 7.4×10^4 and $\frac{A}{D}$ = 0.12 and 0.24, the Grashof number is sufficiently large that $Nu_v(\psi)$ lies above the forced convective curve.

Average, Local Heat Transfer

Average, local Nusselt numbers (local values averaged over a representative cycle), $Nu_v(\theta)$, were calculated by averaging 12 instantaneous, local Nusselt numbers over one cycle of oscillation. Two representative tests are shown in

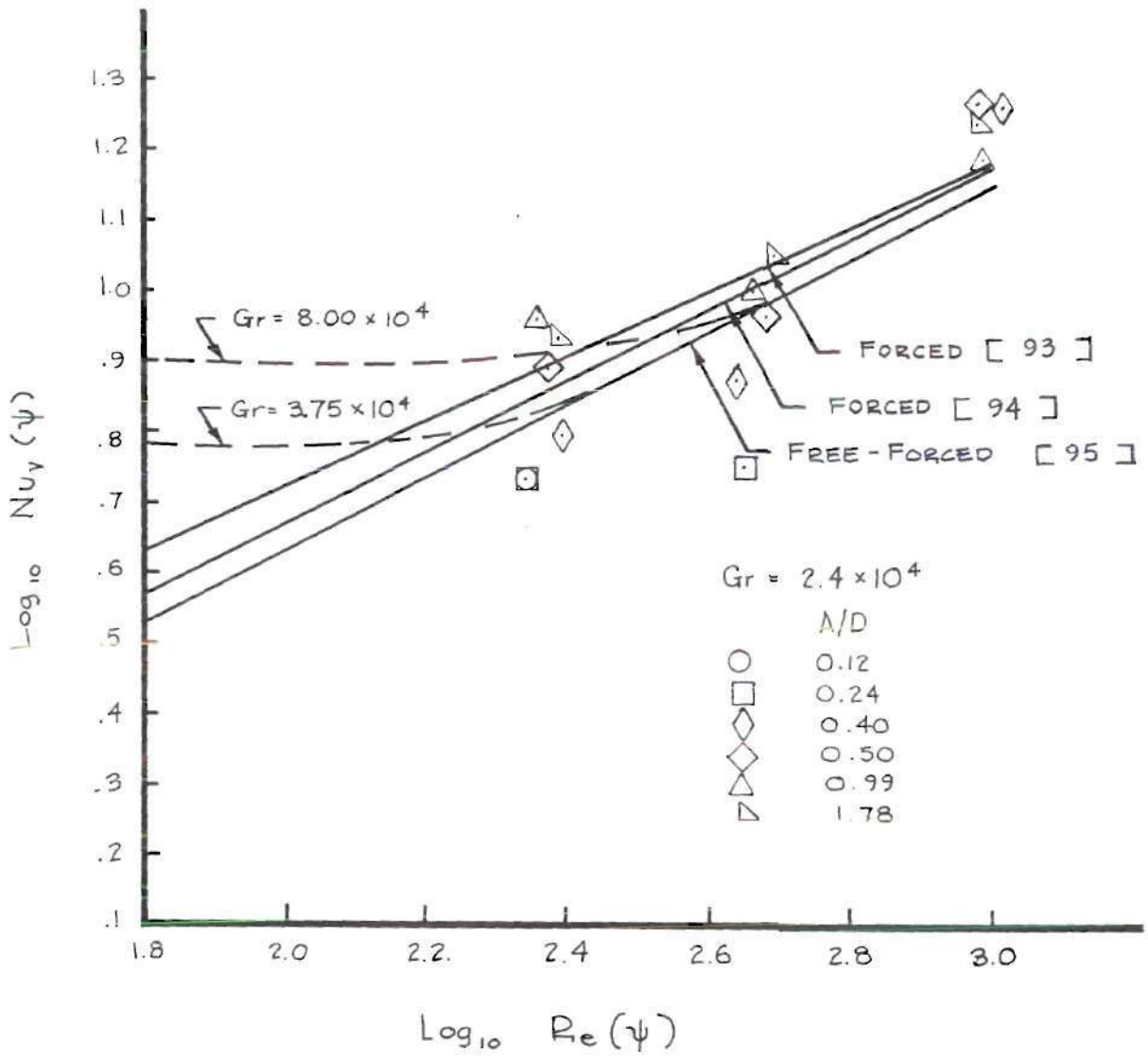

Figure 30. Comparison of $Nu_y(\psi)$ at ψ of 90° with Forced and Mixed Free-Forced Convection for Gr = 2.4 x 10^4

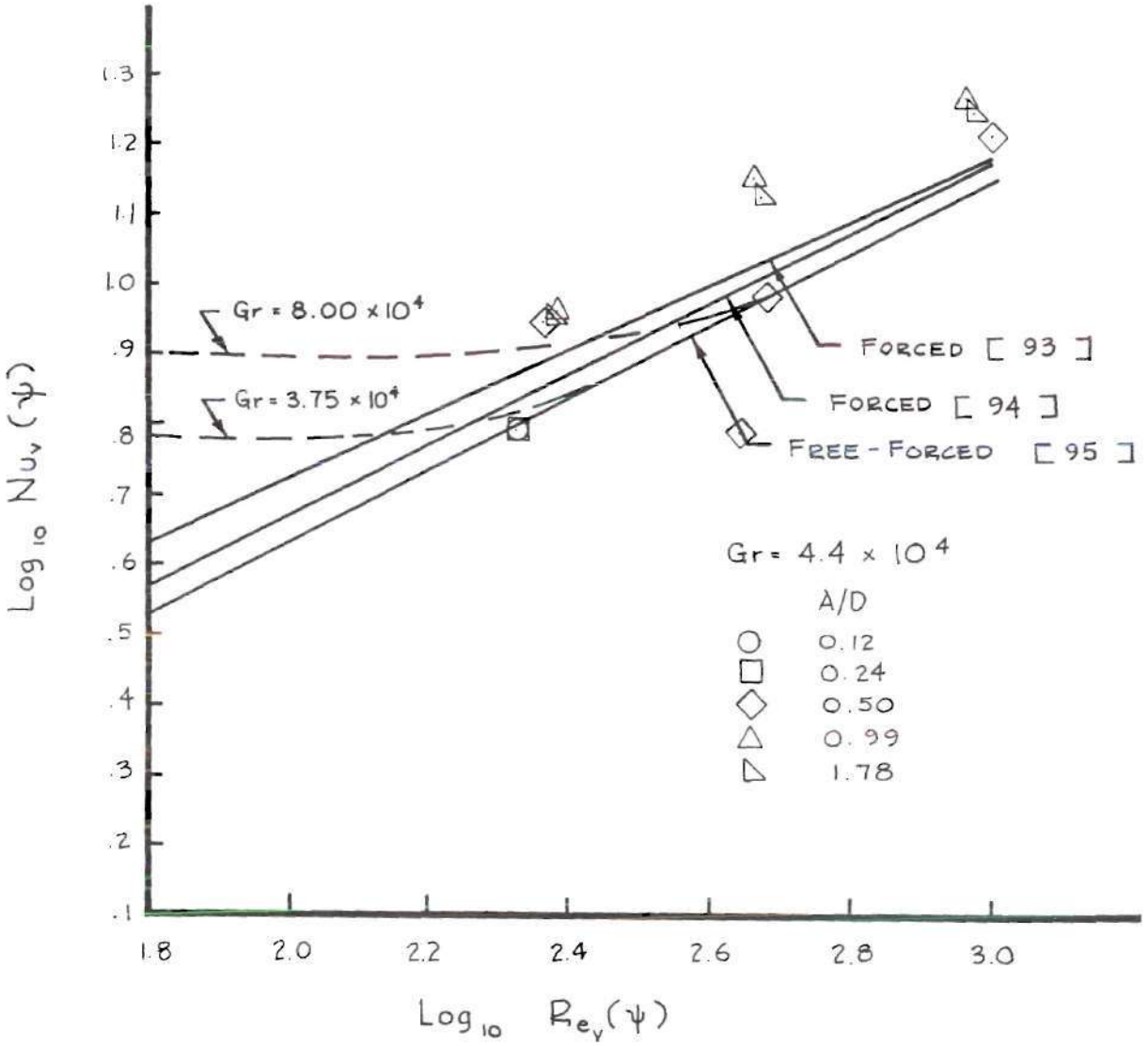

Figure 31. Comparison of $Nu_y(\psi)$ at ψ of 90° with Forced and Mixed Free-Forced Convection for Gr = 4.4 x 10^4

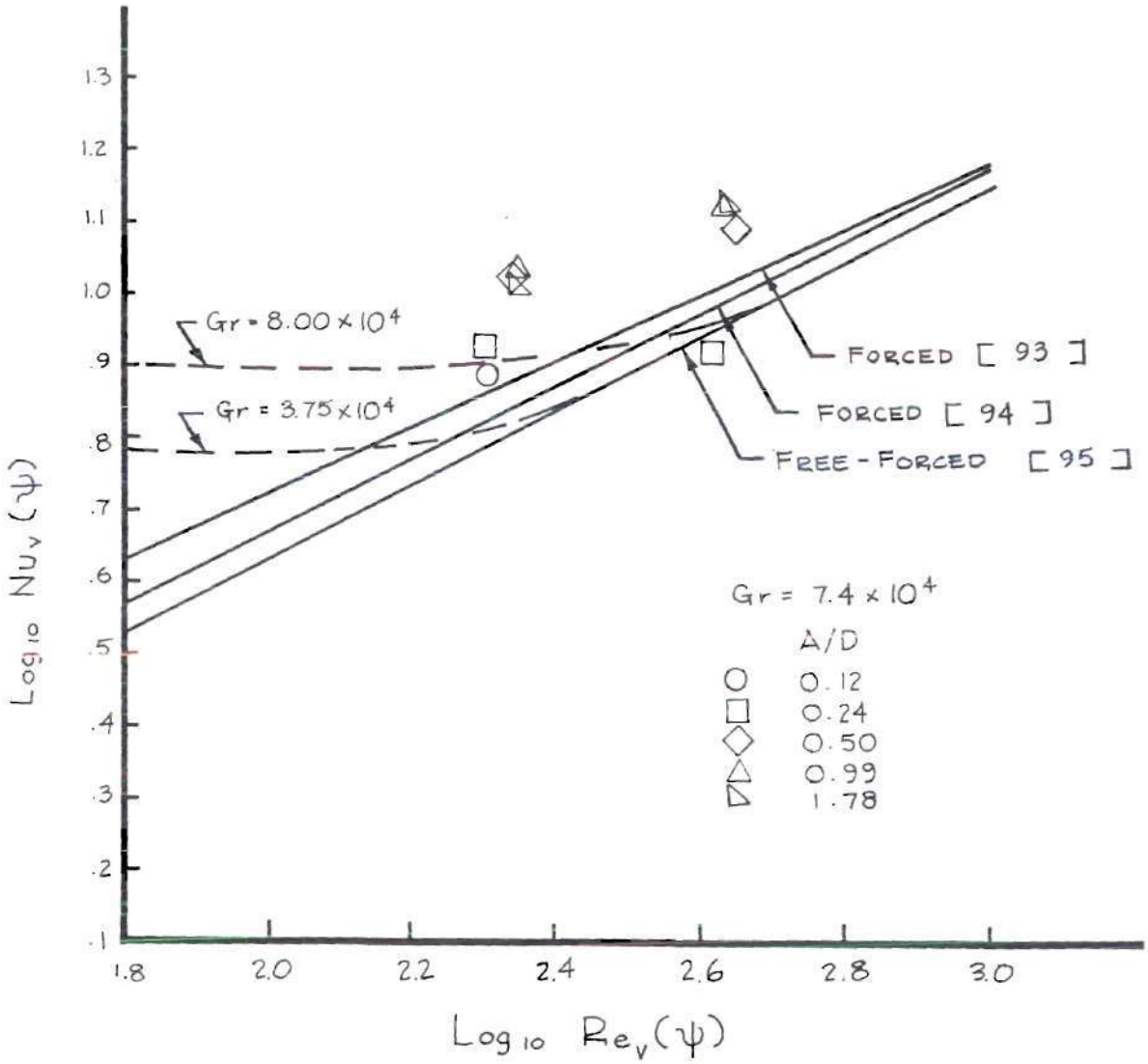

Figure 32. Comparison of $Nu_v(\psi)$ at ψ of 90° with Forced and Mixed Free-Forced Convection for Gr = 7.4 x 10^4

Figures 33 and 34.

In Figure 33, the distribution of $Nu_V(\theta)$ is plotted for $\frac{A}{D} = 0.41$, $Gr = 24956$, and $Re_A = 660$. These dimensionless numbers correspond to a frequency of oscillation of 10.7 cycles per second. Comparison of $Nu_V(\theta)$ with the stationary values in Figure 33 shows that vibration increased the heat transfer at all positions around the cylinder. The plot of $Nu_V(\theta)$ substantiates conclusions drawn in the flow visualization study to be discussed in a later section of this chapter. The flow visualization revealed that, for this case, the vibration of the cylinder caused a phenomenon of boundary-layer shedding both at the bottom and top of the cylinder each time the cylinder changed directions. The free convective chimney was washed off at higher frequencies of oscillation, and a forced convective type flow was observed around the cylinder particularly at positions in the center region of oscillation. Thus, the heat-transfer rate in the region of the top of the cylinder was greatly increased over the free convective value. The symmetry of this plot about a horizontal line through 90 and 270 degrees reveals the fact that the free convective influence was small for this case. The increases of the heat transfer on the sides of the cylinder reveal that the horizontal motion of the cylinder was greater than the free convective boundary-layer thickness. Air was forced around the bottom and top of the cylinder causing the boundary layer to thin on the leading side of the cylinder

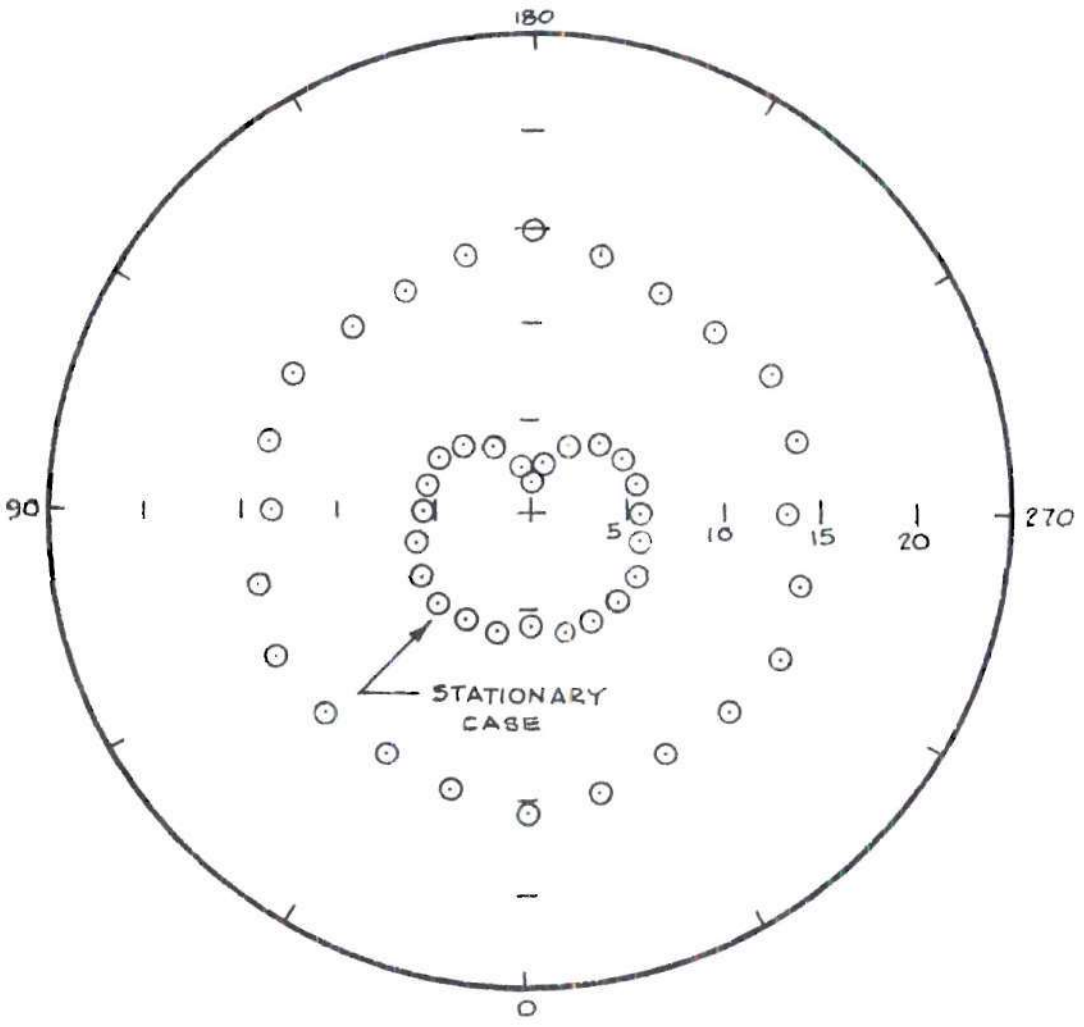

Figure 33. Distribution of $Nu_v(\theta)$ with θ for $\frac{A}{D} = 0.41$, Gr = 24956, and $Re_A = 660$

resulting in an increase in the heat transfer in these regions.

In Figure 34, the distribution of $Nu_v(\theta)$ is plotted for $\frac{A}{D} = 1.78$, $Gr = 25469$, and $Re_A = 610$. These dimensionless numbers correspond to a frequency of oscillation of 2.3 cycles per second. All values of $Nu_v(\theta)$ were larger than the corresponding free convective values. The plot of $Nu_v(\theta)$ corroborates observations made in the flow visualization study which revealed that the increases in the heat transfer for this case were primarily due to the fact that the extended horizontal motion of the cylinder was much larger than the free convective boundary-layer thickness. The large-amplitude motion forced air around the bottom and top of the cylinder causing the boundary layer to thin on the leading side of the cylinder which resulted in an increase in the heat transfer in this region. The free convective influence was still present around the top of the cylinder at $\frac{A}{D} = 1.78$ even at $Re_A = 610$ because the low frequency swaying of the plume was not sufficient to eliminate the plume entirely; however, there was a region on the trailing side of the cylinder that resembled the circulation of vortices. The plume was observed to curl towards the horizontal direction which indicated that air was circulating around the cylinder causing an increase in the heat transfer around the top of the cylinder. In Figure 34, there is a dip in the plot of $Nu_v(\theta)$ in the region around the top of the cylinder revealing the persistence of the free convective chimney and the inability of the

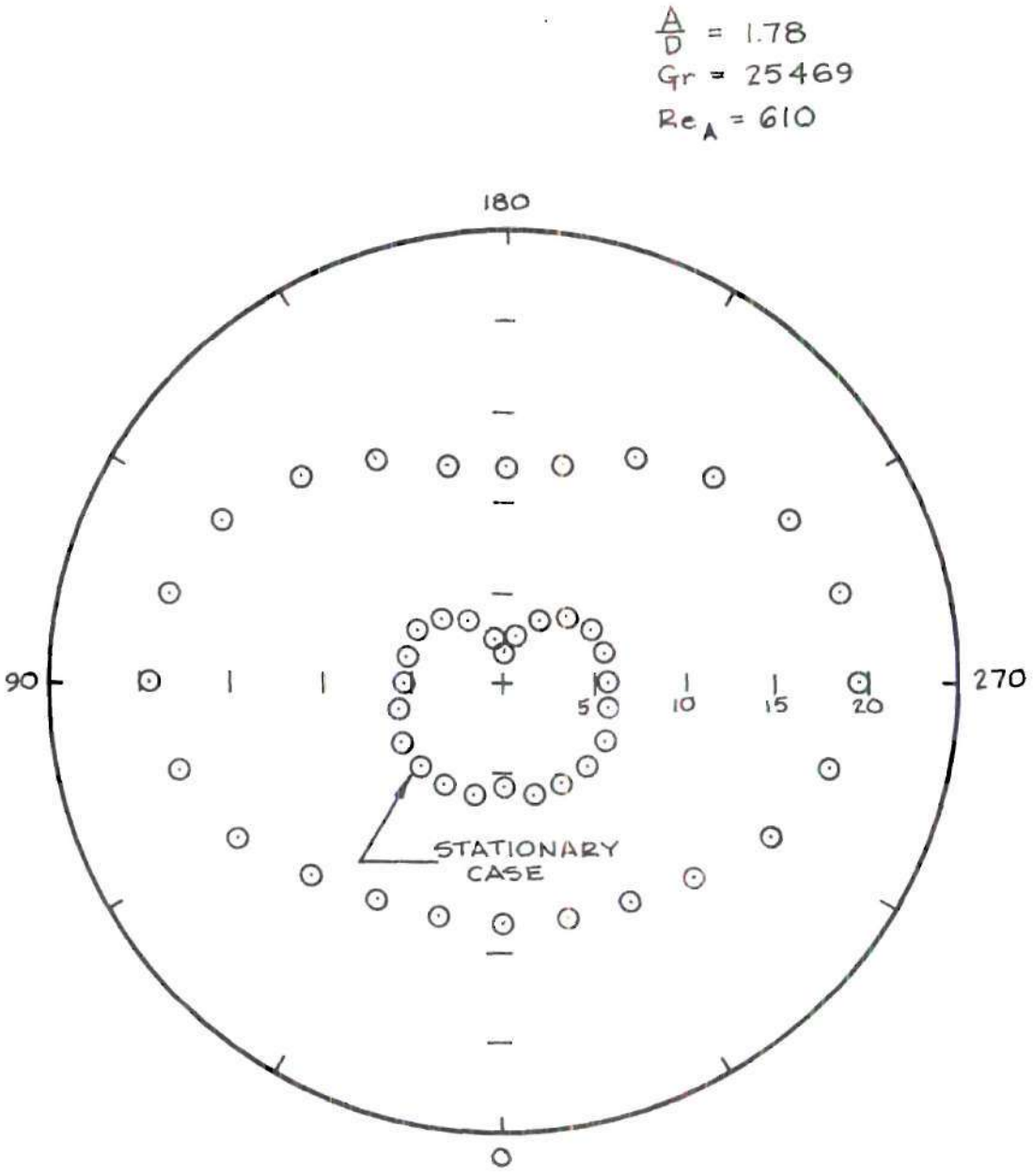

Figure 34. Distribution of $Nu_V(\theta)$ with θ for $\frac{A}{D} = 1.78$, Gr = 25469, and $Re_A = 610$

low frequency oscillation to remove from the cylinder the plume entirely.

The plot of $Nu_v(\theta)$ obtained by Fand et al. [12] is quite different from those shown in Figures 33 and 34. When $Nu_v(\theta)$ was plotted, figure 8-shaped curves (with the pinch in the horizontal direction) were obtained, and regions (near θ=97 and 263 degrees) of locally reduced heat transfer were reported. The investigation reported in reference 12 was made for acoustical vibrations, and the value of $\frac{A}{D}$ was approximately two orders of magnitude smaller than those reported in this study and, therefore, cannot be expected to compare closely with the results of this investigation. The mechanism responsible for the changes in $Nu_v(\theta)$ was reported to be thermoacoustic streaming which was discussed in detail in Chapter II.

Average Heat Transfer

An overall average Nusselt number, $\overline{Nu}_v$, was calculated for all of the vibratory tests by averaging the instantaneous, average Nusselt numbers over the cycle of oscillation. A check of this interferometric measurement of the overall average Nusselt number was made by writing an energy balance on the cylinder. In this section, a comparison of values of the average Nusselt number by the interferometric method and the energy balance method is made. Then the value of $\overline{Nu}_v$ is compared with the stationary free convective value, and the effects of the dimensionless parameters on Nu_v are discussed.

Finally, the value of $\overline{Nu}_V$ is compared with forced and mixed free-forced convective Nusselt numbers.

A comparison was made between the average Nusselt number by the interferometric method, $\overline{Nu}_V$, and the average Nusselt number by the energy balance method, $\overline{Nu}_{bal}$. The per cent difference between $\overline{Nu}_V$ and $\overline{Nu}_{bal}$ was computed and is presented in Table 4 along with the individual values of $\overline{Nu}_V$ and $\overline{Nu}_{bal}$. The average difference between the values for the two methods was 4 per cent.

All values of $\overline{Nu}_V$ were compared with the average Nusselt number, $\overline{Nu}_F$, for the free convecting stationary cylinder at the same Gr. The per cent difference between $\overline{Nu}_V$ and $\overline{Nu}_F$ was computed and is tabulated in Table 5. All values of $\overline{Nu}_V$ were larger than the corresponding value of $\overline{Nu}_F$. The largest difference between $\overline{Nu}_V$ and $\overline{Nu}_F$ was 200 per cent, and the smallest difference was 1 per cent.

The values of $\overline{Nu}_V$ for low $\frac{A}{D}$ (0.12 and 0.24) did not increase much over the value of $\overline{Nu}_F$. This is due to the fact that at low values of $\frac{A}{D}$, the amplitude of oscillation does not extend beyond the thermal-boundary layer established by free convection, and therefore, there is no periodic displacement of fluid across the cylinder to effect a net increase in heat transfer. Natural convection dominates at low vibrational intensities, and significant increases in heat transfer occur only when a critical vibrational intensity is reached. Then, a type of coupling between streaming currents due to vibration

Table 4. Comparison of $\overline{Nu}_v$ and $\overline{Nu}_{bal}$

$\frac{A}{D}$	$Af(\frac{in}{sec})$	ΔT(°F)					
		25		50		100	
		$\frac{\overline{Nu}_v}{\overline{Nu}_{bal}}$	Per Cent Difference	$\frac{\overline{Nu}_v}{\overline{Nu}_{bal}}$	Per Cent Difference	$\frac{\overline{Nu}_v}{\overline{Nu}_{bal}}$	Per Cent Difference
0	stationary	5.3 5.6	5	6.3 6.5	3	7.9 7.4	-5
1/8	1	5.5 5.8	4	6.4 6.6	2	8.0 7.5	-6
1/4	1	5.6 5.8	2	6.8 6.9	2	8.5 8.0	-5
	2	6.1 6.3		6.8 6.9	1	8.7 8.3	-4
3/8	1	6.6 6.9	3				
	2	7.4 7.9	5				
	4	14.3 13.9	-3				
1/2	1	7.1 7.4	5	8.3 8.3	0	9.9 9.2	-7
	2	8.5 8.9	5	9.3 10.0	9	11.6 10.9	-6
	4	14.4 14.4	0	14.9 15.3	3		
1	1	7.7 7.5	2	8.2 8.3	2	9.5 9.0	-5
	2	9.8 9.5	2	11.9 10.4	2	11.7 10.9	-8
	4	14.3 14.2	0	16.0 14.8	-7		
7/4	1	7.4 7.7	4	7.9 8.0	1	9.1 8.6	-6
	2	10.2 10.6	3	11.4 10.6	-7	11.2 10.9	-3
	4	15.9 15.0	-5	15.6 15.6	0		

Table 5. Comparison of $\overline{Nu}_V$ and $\overline{Nu}_F$

Average Nu Results

$\frac{A}{D}$	$Af(\frac{in}{sec})$	$(\frac{\overline{Nu}_V}{\overline{Nu}_F} - 1) \times 100\%$		
		$\Delta T(°F)$		
		25	50	100
0	Stationary			
1/8	1	4	3	1
1/4	1	6	8	8
	2	14	8	10
3/8	1	24		
	2	39		
	4	170		
1/2	1	33	33	25
	2	55	48	46
	4	170	140	
1	1	43	29	19
	2	79	88	49
	4	170	160	
7/4	1	38	26	15
	2	92	81	42
	4	200	150	

and natural convective currents occurs which effects a net increase in enthalpy transport. Due to the limitations of frequency of the vibrational equipment used in this investigation, the critical vibrational intensity could not be reached.

For a given value of Re_A, the increase in the heat-transfer rate was larger at low values of Gr. This was due to the fact that the ratio $\frac{Re^2_A}{Gr}$ was larger at low values of Gr, and since this ratio is a measure of the vibrational forces to buoyancy forces, the vibrational forces were stronger at low values of Gr.

Increasing the value of Re_A with other parameters held constant resulted in an increase in the value of $\overline{Nu}_v$. This was due to the fact that the ratio $\frac{Re^2_A}{Gr}$ was larger for larger values of Re_A, and thus, vibrational forces were stronger.

In Figures 35, 36, and 37, $\overline{Nu}_v$ is compared with both forced convective curves recommended by Holman [93] and Oosthiuzen and Madan [94] and free-forced convective curves by Oosthuizen and Madan [95]. The Reynolds number used for the oscillatory test was Re_A. The general trend in these figures is for $\overline{Nu}_v$ to lie above both the forced and mixed convective curves except at low $\frac{A}{D}$ and medium Re_A (300) where vibration had little effect on heat transfer. At higher Re_A where the oscillatory forces dominated, the value of $\overline{Nu}_v$ appears to be parallel and above the forced convective curve.

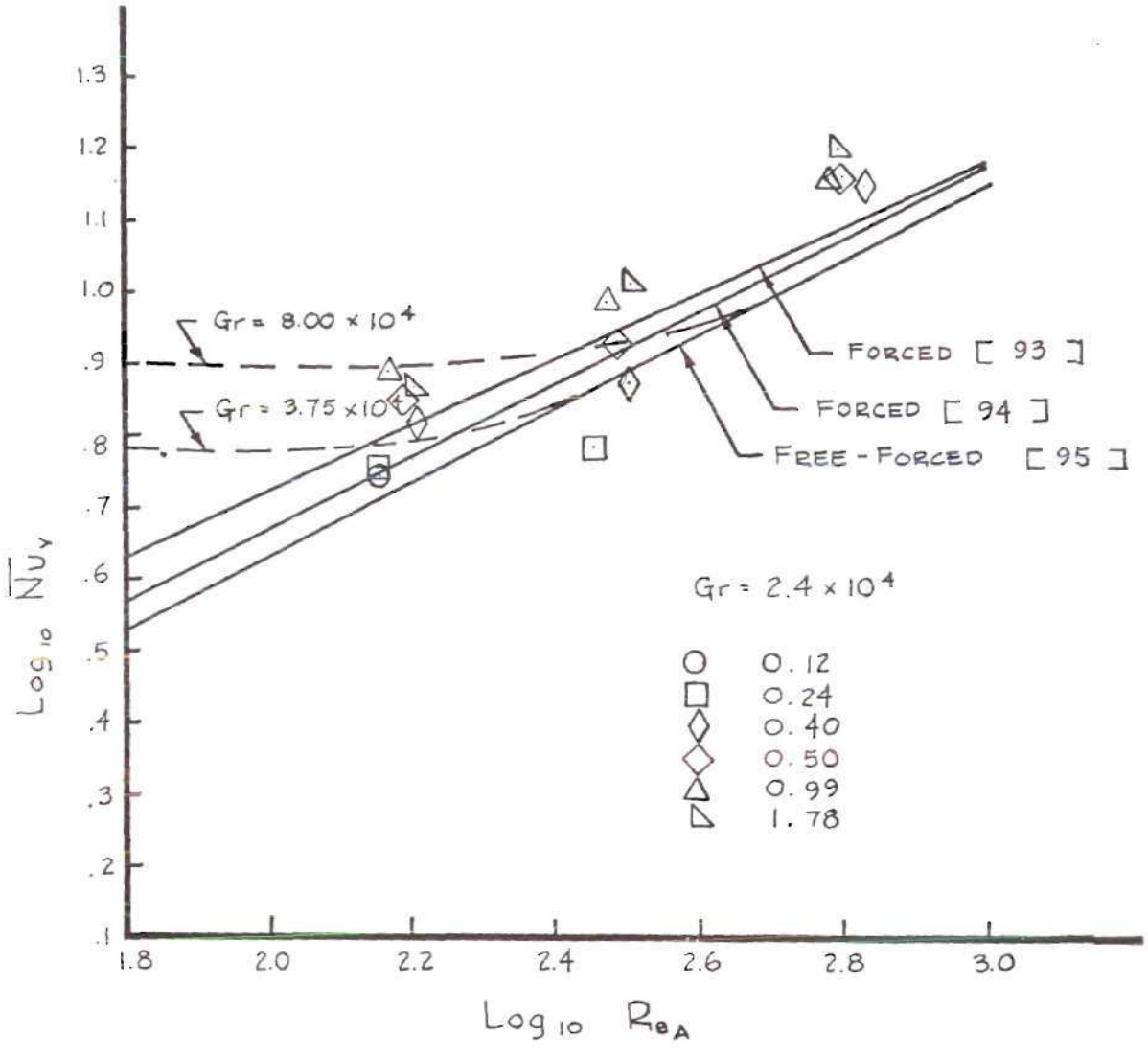

Figure 35. Comparison of $\overline{Nu}_v$ with Forced and Mixed Free-Forced Convection for Gr = 2.4 x 10^4

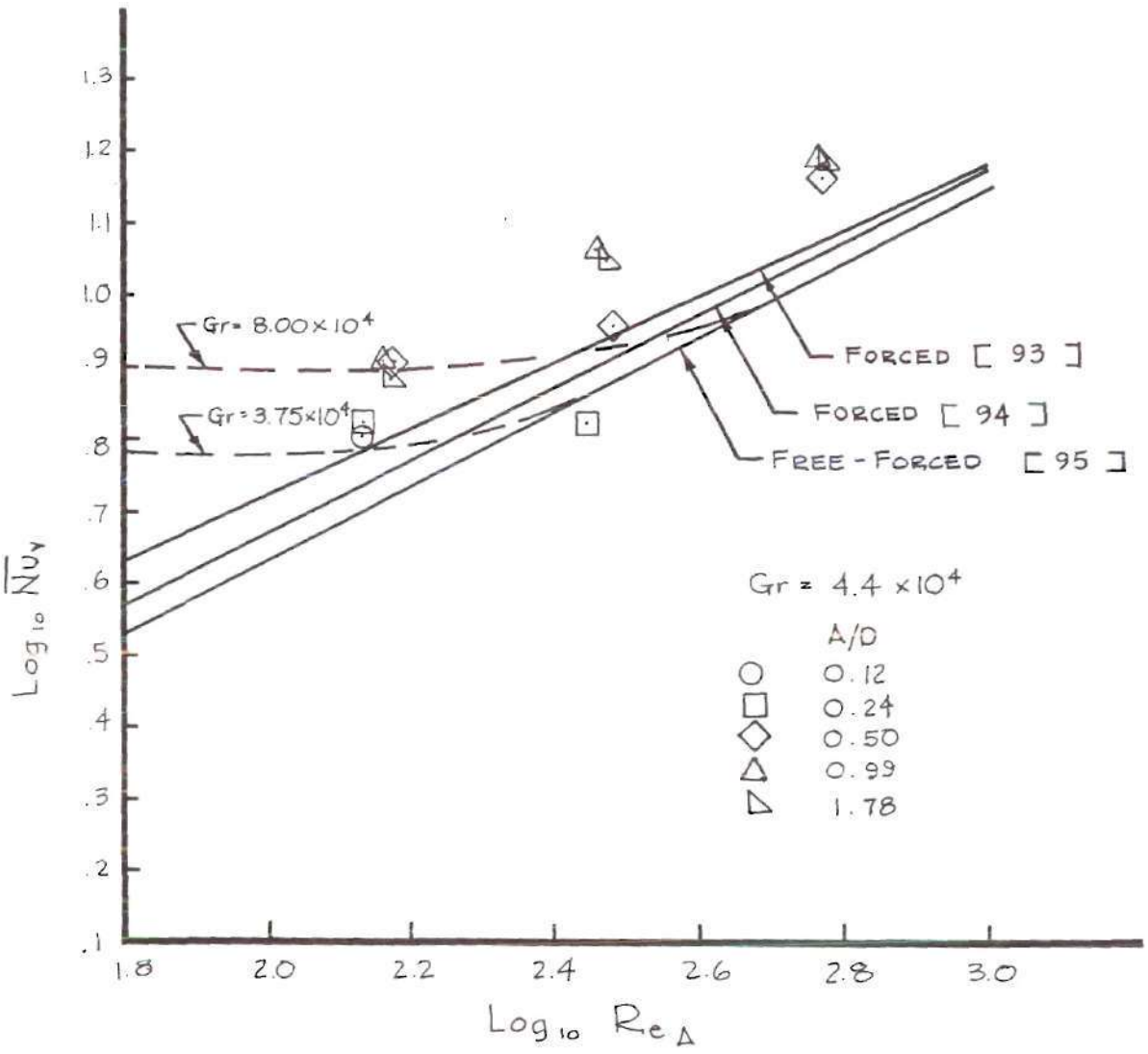

Figure 36. Comparison of $\overline{Nu}_v$ with Forced and Mixed Free-Forced Convection for Gr = 4.4 x 10^4

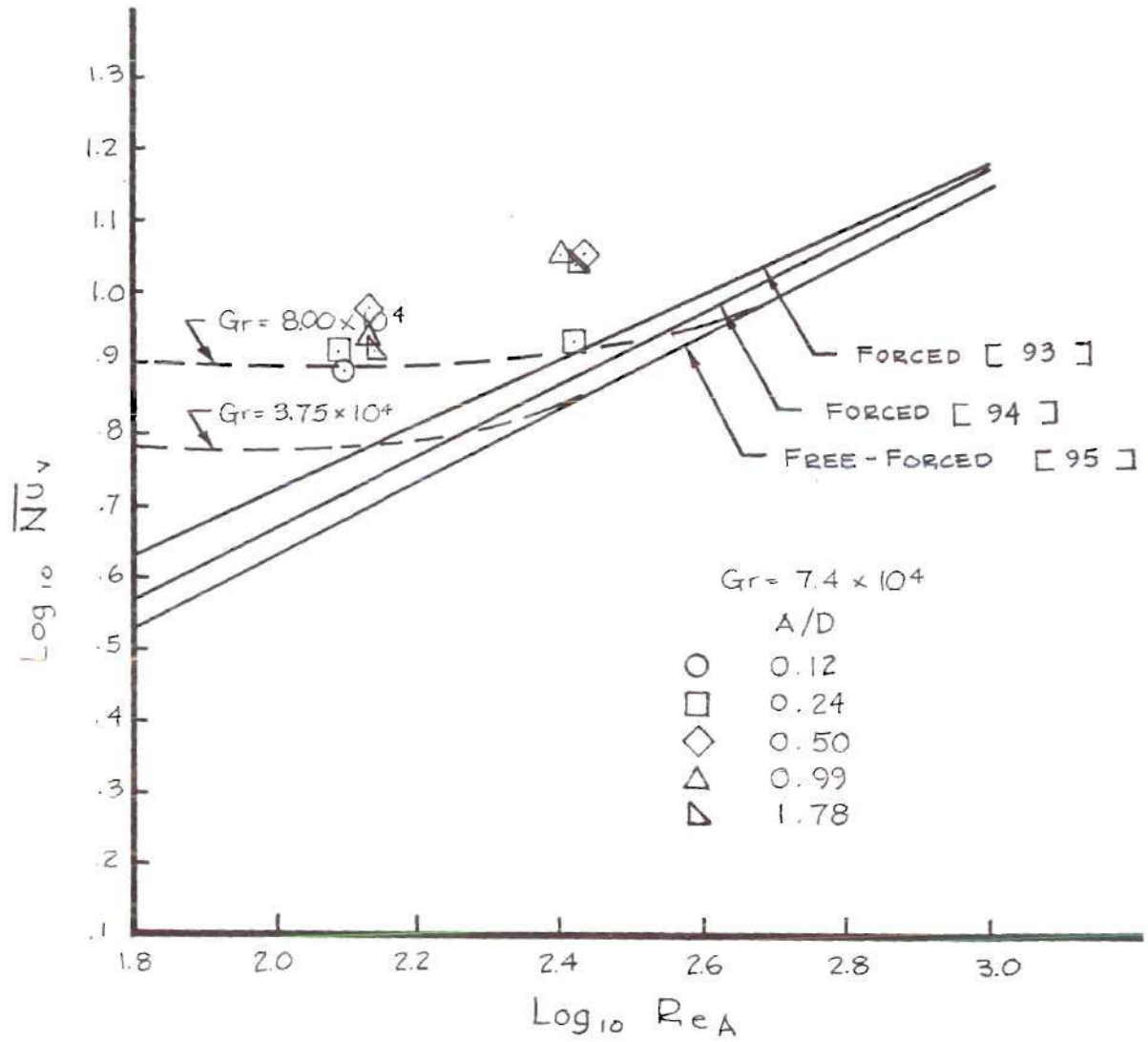

Figure 37. Comparison of $\overline{Nu}_v$ with Forced and Mixed Free-Forced Convection for Gr = 7.4 x 10^4

Correlation for $\overline{Nu}_v$

A correlation for the overall average Nusselt number, Nu_v, has been made by using several combinations of the parameters discussed previously. This correlation and its derivation is discussed in this section.

The assumption was made that $\overline{Nu}_v$ is expressable as a sum of the free convective and oscillatory effects or

$$\overline{Nu}_v = \overline{Nu}_F + \overline{Nu}_{osc} \tag{63}$$

where $\overline{Nu}_F$ is the contribution due to free convection, and $\overline{Nu}_{osc}$ is the contribution due to oscillation. Dividing by $\overline{Nu}_F$ and rearranging Equation (63) gives

$$\frac{\overline{Nu}_v}{\overline{Nu}_F} - 1 = \frac{\overline{Nu}_{osc}}{\overline{Nu}_F} \tag{64}$$

The dimensionless parameters in Equation (62) suggested by previous investigators [17, 92] were used for a first attempt to correlate the data. These parameters were used since they are most often encountered in the literature. The assumed form of the correlation was first selected to be

$$\frac{\overline{Nu}_v}{\overline{Nu}_F} - 1 = \frac{\overline{Nu}_{osc}}{\overline{Nu}_F} = a\left(\frac{A}{D}\right)^b (Re_A)^c (Gr)^d \tag{65}$$

where a, b, c, and d are constants to be determined. The Prandtl number, Pr, was not included because it was virtually a constant for the ranges of temperature and pressures used in this investigation. Studying sets of data for constant values of Gr and Re_A indicated that $\frac{A}{D}$ raised to a constant power was not sufficent to account for the changes in $\frac{\overline{Nu}_{osc}}{\overline{Nu}_F}$ and that the influence of $\frac{A}{D}$ appeared to vary with Re_A. To account for this variation, a second correlation was attempted in the form

$$\frac{\overline{Nu}_{osc}}{\overline{Nu}_F} = a\left(\frac{A}{D}\right)^{(b+cRe_A^{z_c})} Re_A^{d} Gr^{e_c} \tag{66}$$

where a, b, c, d, e_c, and z_c are constant. By taking the logarithm of both sides of Equation (66), the following expression is obtained

$$Log\left(\frac{\overline{Nu}_{osc}}{\overline{Nu}_F}\right) = Log(a)+bLog\left(\frac{A}{D}\right)+cRe_A^{z_c}Log\left(\frac{A}{D}\right) +$$

$$dLog(Re_A)+e_cLog(Gr) \tag{67}$$

Equation (67) can be rewritten as

$$B = A_1X_1 + A_2X_2 + A_3X_3 + A_4X_4 + A_5X_5 \tag{68}$$

or

$$B = \sum_{j=1}^{5} A_jX_j \tag{69}$$

where

$$B = \text{Log}\left(\frac{\overline{Nu}_{osc}}{\overline{Nu}_F}\right) \tag{70}$$

$$A_1 = 1 \tag{71}$$

$$A_2 = \text{Log}\left(\frac{A}{D}\right) \tag{72}$$

$$A_3 = Re_A^{\ z_c}\text{Log}\left(\frac{A}{D}\right) \tag{73}$$

$$A_4 = \text{Log}(Re_A) \tag{74}$$

$$A_5 = \text{Log}(Gr) \tag{75}$$

$$X_1 = \text{Log}(a) \tag{76}$$

$$X_2 = b \tag{77}$$

$$X_3 = c \tag{78}$$

$$X_4 = d \tag{79}$$

$$X_5 = e_c \tag{80}$$

Equation (69) represents an equation with five unknowns X_j for a given set of data and a given z_c. For i sets of data, there are i equations similar to Equation (69) or

$$B_i = \sum_{j=1}^{5} A_{ij} X_j \tag{81}$$

When z_c is specified, Equation (81) represents i simultaneous equations in the five unknowns X_j. The values of X_j to best fit the data for a specified z_c were calculated using a least squares technique which is explained in Appendix H. Values of z_c and X_j which best fit the data were obtained by iteration on z_c. The values of z_c and X_j were used with Equations (76) through (80) to find the coefficient and exponents for the correlation expressed in Equation (66).

Several other combinations of variables were used to correlate the data. These combinations included three sets of parameters suggested in reference 7. The general form of

the correlation was

$$\frac{\overline{Nu}_V}{\overline{Nu}_F} - 1 = \frac{\overline{Nu}_{osc}}{\overline{Nu}_F} = a\left(\frac{A}{D}\right)^{(b+cF_c^{z_c})} F_c^{d} Gr^{e_c} \tag{82}$$

where, as in Equation (66), a, b, c, d, e_c, and z_c are constants. The symbol F_c represents the parameters Re_s, $\frac{Re_s}{Gr^{1/2}}$, $\frac{Re_{freq}}{Gr^{1/2}}$, $\frac{Re_A}{(\frac{A}{D})^{1/2}}$, and $\frac{Re_A}{Gr^{1/2}}$.

For each correlation, the per cent difference between the experimental and the correlative values of $\frac{\overline{Nu}_V}{\overline{Nu}_F}$ was calculated for each data point. The per cent difference was based on the experimental value. An average difference was calculated for each correlation by summing the absolute values of the per cent difference for each data point and dividing by the total number of points.

The smallest per cent difference for the parameter, F_c, was achieved when the form of F_c was the streaming Reynolds number, Re_s. The average difference between the theoretical curve and the experimental data was 6 per cent, and the maximum difference was 14 per cent. The resulting correlation was

$$\frac{\overline{Nu}_V}{\overline{Nu}_F} = 1+0.103\left(\frac{A}{D}\right)^{(-32.3+33.5Re_s^{-0.01})} Re_s^{1.09} Gr^{-0.452} \tag{83}$$

or

$$\frac{\overline{Nu}_V}{\overline{Nu}_F} = 1+\Phi_1 \tag{84}$$

where

$$\Phi_1 = 0.103\left(\frac{A}{D}\right)^{(-32.3+33.5Re_s^{-0.01})} Re_s^{1.09} Gr^{-0.452} \tag{85}$$

A plot of this correlation is shown in Figure 38.

The correlation for $F_c = \frac{Re_s}{Gr^{1/2}}$ in Equation (82) resulted in per cent differences very close to those when F_c equals Re_s. The average difference was 6 per cent, and the maximum difference was 15 per cent.

The correlation of Equation (83) was extended beyond the ranges of nondimensional parameters for which it was derived to check the accuracy to which it could fit the results of Fand and Peebles [25]. In this reference, the heat-transfer results of investigations involving mechanical and acoustical vibration were compared. The ranges of parameters used in their tests were:

Mechanical Vibrations

$$0.0290 \leq \frac{A}{D} \leq 0.143 \tag{86}$$

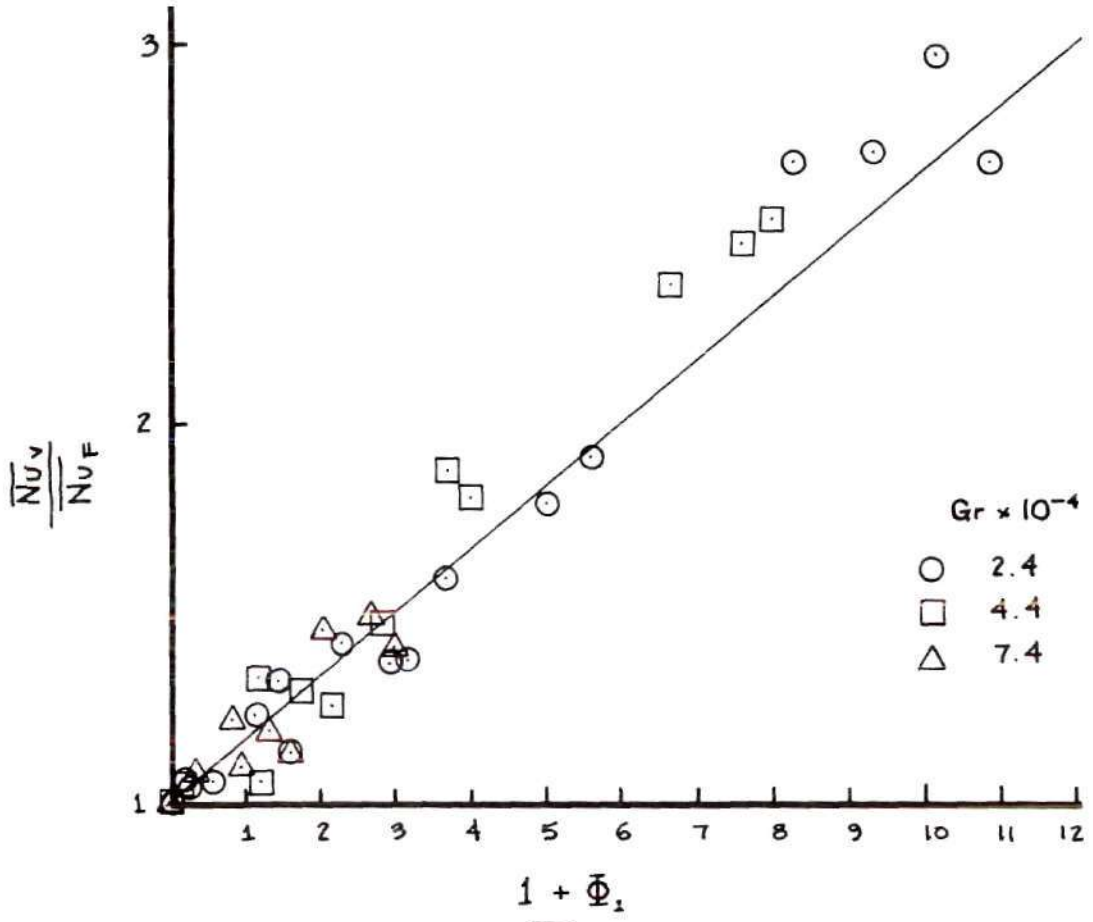

Figure 38. Correlation for $\frac{\overline{Nu}_V}{\overline{Nu}_F}$ Expressed in Equation (83)

$$300 \leq Re_A \leq 1814 \tag{87}$$

$$Gr_1 = 34116 \quad (\Delta T=50°F) \tag{88}$$

$$Gr_2 = 75890 \quad (\Delta T=150°F) \tag{89}$$

Acoustical Vibrations

$$0.0024 \leq \frac{A}{D} \leq 0.0120 \tag{90}$$

$$257 \leq Re_A \leq 1556 \tag{91}$$

$$Gr_1 = 21484 \quad (\Delta T=50°F) \tag{92}$$

$$Gr_2 = 47791 \quad (\Delta T=150°F) \tag{93}$$

A plot of correlative and experimental values of $\frac{\overline{Nu}_V}{\overline{Nu}_F}$ for mechanical vibration is shown in Figure 39. The correlative values are in good agreement with the experimental values except for two points where Re_A is above 1500. The maximum value of Re_A for the tests from which the correlation was derived was 660. If the points for Re_A greater than 1500 are excluded, the average difference between correlative value and experimental value of $\frac{\overline{Nu}_V}{\overline{Nu}_F}$ was 8 per cent.

The correlation given in Equation (83) completely

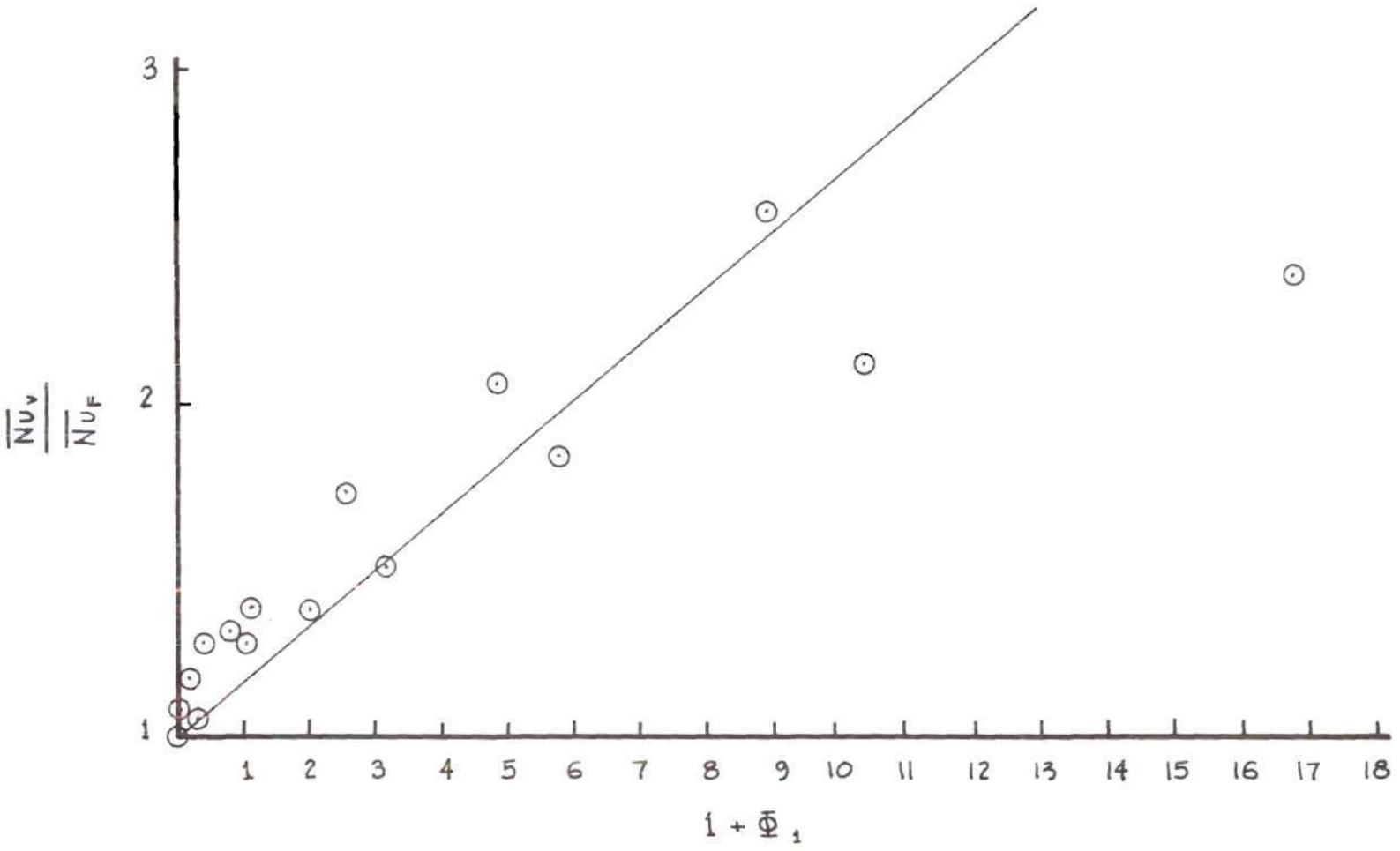

Figure 39. Correlation for $\frac{\overline{Nu}_V}{\overline{Nu}_F}$ (Equation (83)) Applied to Mechanical Vibrational Data of Reference 25

failed in predicting $\frac{\overline{Nu}_V}{\overline{Nu}_F}$ for the acoustical vibration case. This was probably due to the fact that $\frac{A}{D}$ for this case was approximately two orders of magnitude smaller than the $\frac{A}{D}$ for the tests for which the correlation was derived. Fand and Peebles stated that their results indicated that the parameter $\frac{A}{D}$ was not important for the range of data in their investigation; however, for the range of parameters used in this investigation, $\frac{A}{D}$ greatly influenced the value of $\frac{\overline{Nu}_V}{\overline{Nu}_F}$.

An attempt to extend the correlation to the range of parameters used by Lemlich [17] failed, probably due to the fact that Re_A and Gr in Lemlich's tests were smaller by approximately one and four orders of magnitude, respectively, than Re_A and Gr in the tests for which the correlation was derived.

Qualitative Flow Visualization

A flow visualization study of the heated air surrounding the cylinder was made to give insight into the mechanisms involved in oscillatory flow. High speed motion pictures were made of interference patterns produced by the infinite fringe setting of the differential interferometer. The comments that will be made here are based on the careful observation of a large number of 16 mm frames. Several figures, each consisting of eight photographs of the infinite fringe interference pattern, are included to facilitate the discussion of the flow patterns around the cylinder. Seven

of the photographs correspond to seven different ψ locations while the eighth photograph shows the flow pattern for the stationary cylinder. The infinite fringe patterns in the photographs are for the component of the gradient either in the horizontal or vertical direction. The photographs of the horizontal component of the gradient revealed more information regarding the heat-transfer mechanism in regions around the sides of the cylinder because the horizontal component of the gradient is largest in this region, but it is zero at the bottom and top of the cylinder. Similarly, the photographs of the vertical component of the gradient revealed more information in the regions near the top and bottom of the cylinder. Generally, the direction of the component selected was the one which gave the most information concerning the overall flow pattern. For one test, interferograms of both components of the gradient are shown (see Figures 41 and 42).

The results of the flow visualization are discussed in the order of increasing Reynolds number. For low values of Re_A (approximately 150), the observed flow pattern varied greatly with the value of $\frac{A}{D}$ while the influence of the Grashof number on the flow pattern was small. The flow patterns for values of $\frac{A}{D}$ of 0.12 (see Figure 40) and 0.24 were very similar. The flow resembled free convection particularly near the center point of oscillation. The plume remained nearly vertical, but swaying was observed in the plume as the cylinder oscillated. A vortex appeared to be

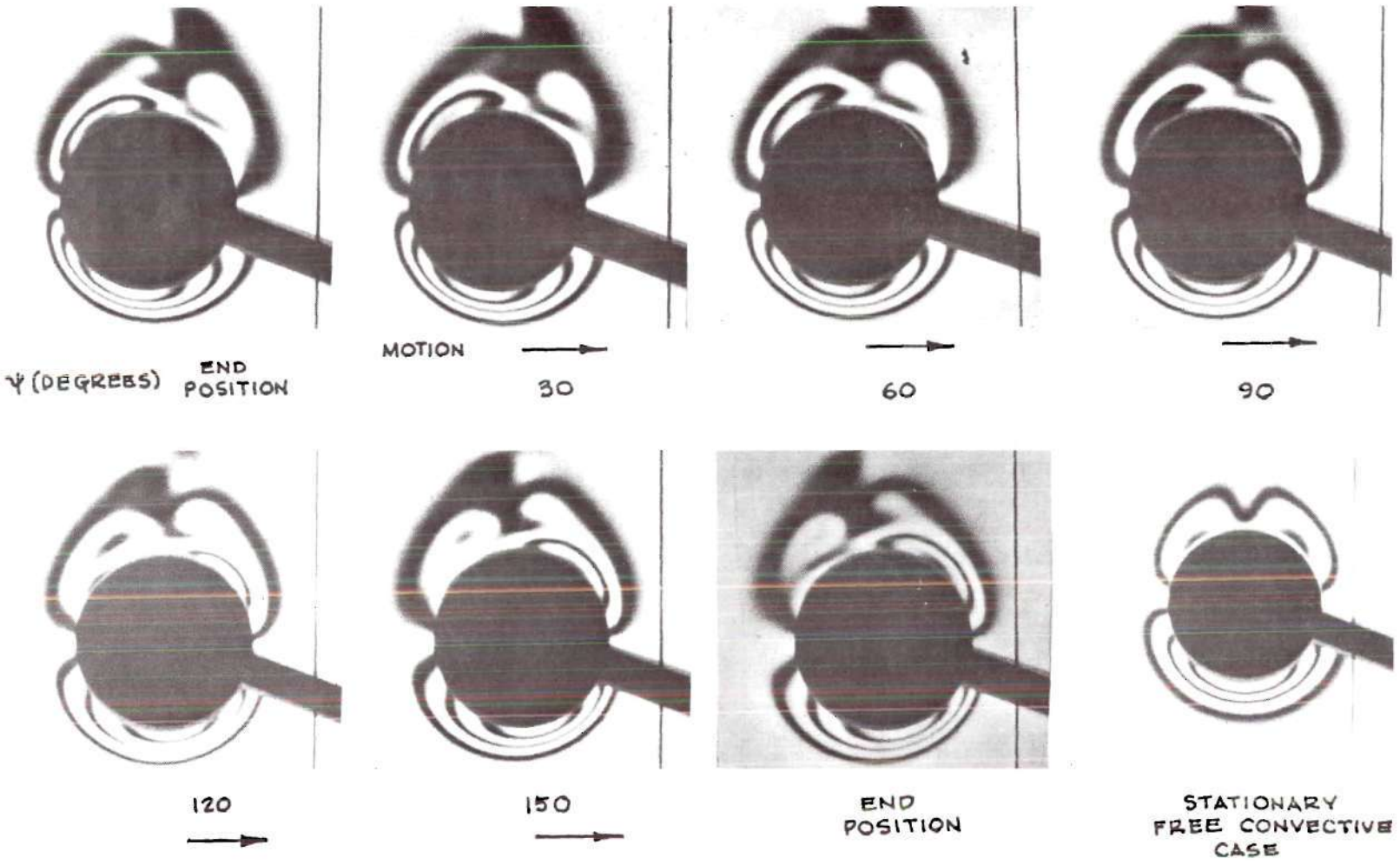

Figure 40. Vertical Infinite Fringe Interferograms for $\frac{A}{D} = 0.12$, $Re_A = 136$, and Gr = 44820

shed on the trailing side of the cylinder in the upper quadrant of the cylinder, and the side on which the shedding occurred alternated with the direction of motion of the cylinder. The flow at the bottom of the cylinder did not appear to be greatly affected. The boundary layer on the bottom half of the cylinder thinned locally near the leading side and thickened on the trailing side, but the flow was not drastically altered. Even though vortex shedding was present, the free convective forces were dominant.

At low values of $\frac{A}{D}$ (0.12 and 0.24), the amplitude of oscillation was smaller than the free convective boundary-layer thickness which was approximately 1/3 of the cylinder diameter, and the oscillatory motion did not cause the cylinder to traverse outside the boundary layer. The stretched film discussed by Lemlich [17] where a film surrounds the entire vibrating path appears to have existed at low values of $\frac{A}{D}$, but at higher $\frac{A}{D}$, the boundary layer oscillated with the cylinder and the stretched film did not exist.

For higher values of $\frac{A}{D}$ (0.39 to 1.77) and for Re_A of approximately 150, the flow pattern was definitely dependent upon $\frac{A}{D}$. The flow patterns for values of $\frac{A}{D}$ from 0.39 to 1.77 had similarities although progressive changes existed throughout this range of values of $\frac{A}{D}$. At low values of $\frac{A}{D}$, the heated wake near the top of the cylinder was restricted in size and more closely resembled the wake in forced flow, but at higher values of $\frac{A}{D}$, the heated wake near the top of the

cylinder was larger and more closely resembled a plume in free convection. The flow patterns for $\frac{A}{D} = 0.52$ and 1.77 are briefly described.

Figures 41 and 42 show the flow patterns around the cylinder for $\frac{A}{D} = 0.52$ and $Re_A = 148$ which correspond to a frequency of oscillation of two cycles per second. When the cylinder was positioned at the extreme left position, the flow on the left side of the cylinder had forced flow characteristics. However, the right side and top show the influence of combined free and forced flow. Flow resembling a free convective plume left the upper right quadrant of the cylinder. Vortex motion was observed in the flow field on the upper right side of the cylinder.

As the cylinder moved to the right in Figure 41, several changes were noticed in the flow pattern. The heated air resembling a plume swayed over the top of the cylinder, and when it reached the middle of the upper left quadrant of the cylinder, it was sheared off and left behind the cylinder. As the cylinder continued to move to the right, the boundary layer on the leading side resembled a forced convective boundary layer.

The boundary layer on the left side of the cylinder as viewed in the photograph of Figure 41 was affected by the motion of the cylinder. The flow field separated near the middle of the upper quadrant of the cylinder, and began to trail the cylinder slanted upward. Vortex-type flow was

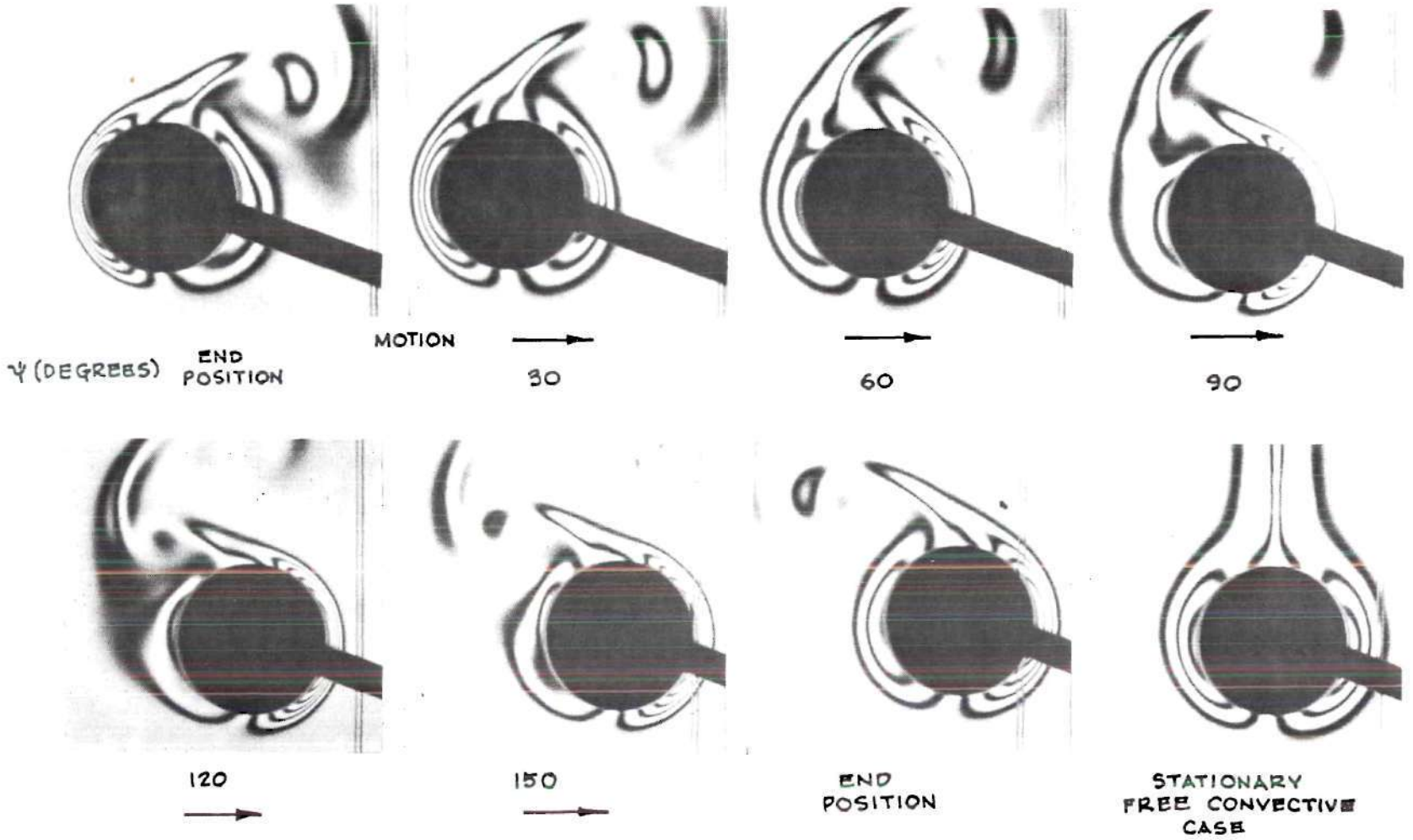

Figure 41. Horizontal Infinite Fringe Interferograms for $\frac{A}{D} = 0.52$, $Re_A = 148$, and Gr = 44025

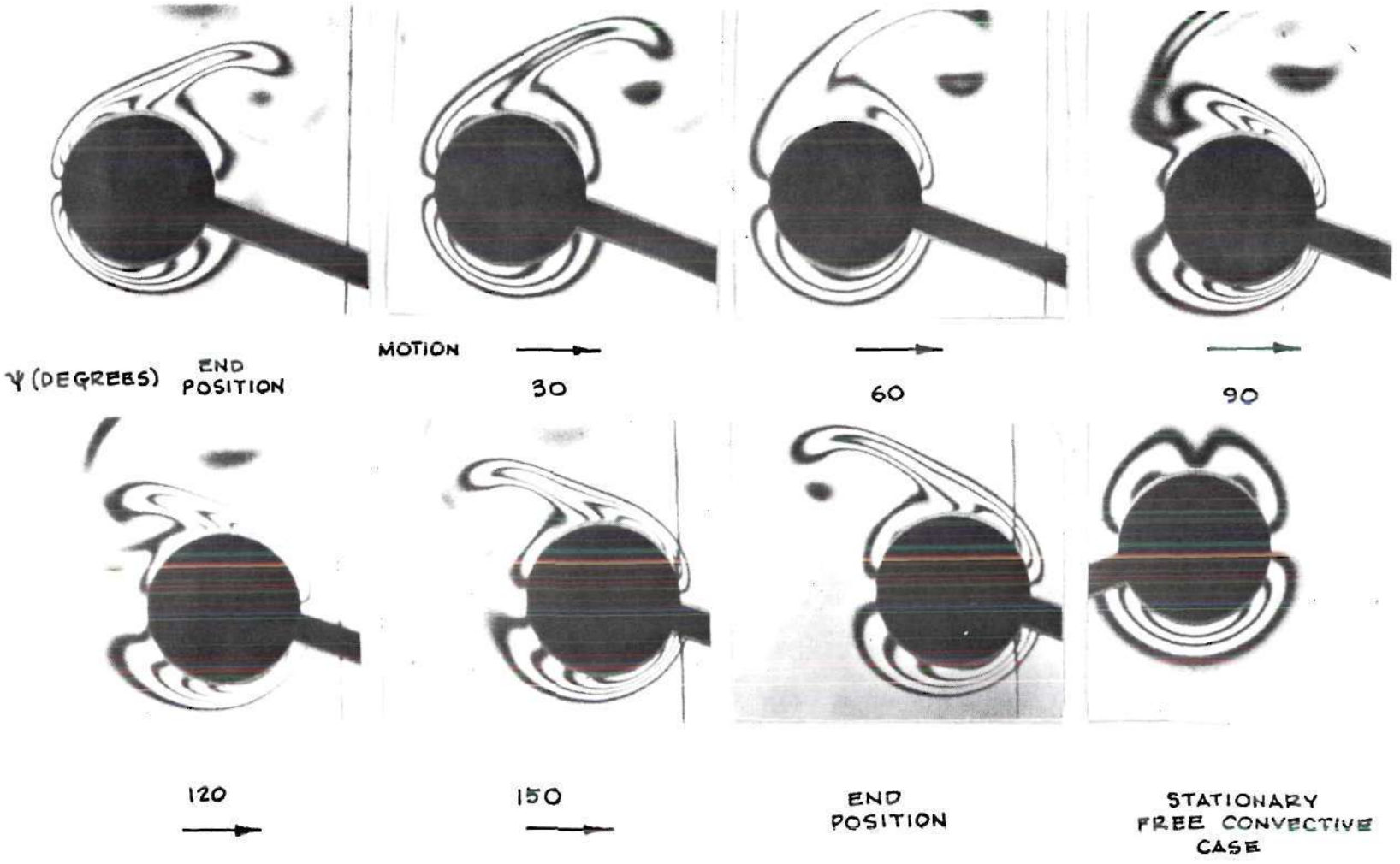

Figure 42. Vertical Infinite Fringe Interferograms for $\frac{A}{D} = 0.52$, $Re_A = 148$, and Gr = 44025

observed in the outermost regions of the flow field. As the cylinder decelerated, the circulation on the trailing side became less evident. As the cylinder stopped at the extreme right position, the flow pattern and boundary-layer shape showed the expected symmetry with the extreme left position of oscillation.

The flow patterns for $\frac{A}{D} = 1.77$ and $Re_A = 147$, which correspond to a frequency of oscillation of 0.57 cycles per second, are illustrated in Figure 43. The free convective effects were more dominant for this larger value of $\frac{A}{D}$, and the free convective characteristics are apparent when Figures 41 and 43 are compared. When the cylinder was positioned at the extreme left position, the flow pattern resembled free convection with a boundary layer encircling the cylinder that was separated from the top of the cylinder and was slanted to the left. The boundary layer on the right side of the cylinder separated near the middle of the right side.

As the cylinder accelerated to the right, the heated air which resembled a plume moved down the left side of the cylinder and was sheared off. The separated flow from the previous half cycle of oscillation on the right side of the cylinder reattached. As the cylinder approached the center of oscillation, the separated flow trailed the cylinder slanted upward revealing the free convective influence. Below the separated flow, the external region of the boundary layer exhibited vortex motion, and the boundary layer on the leading

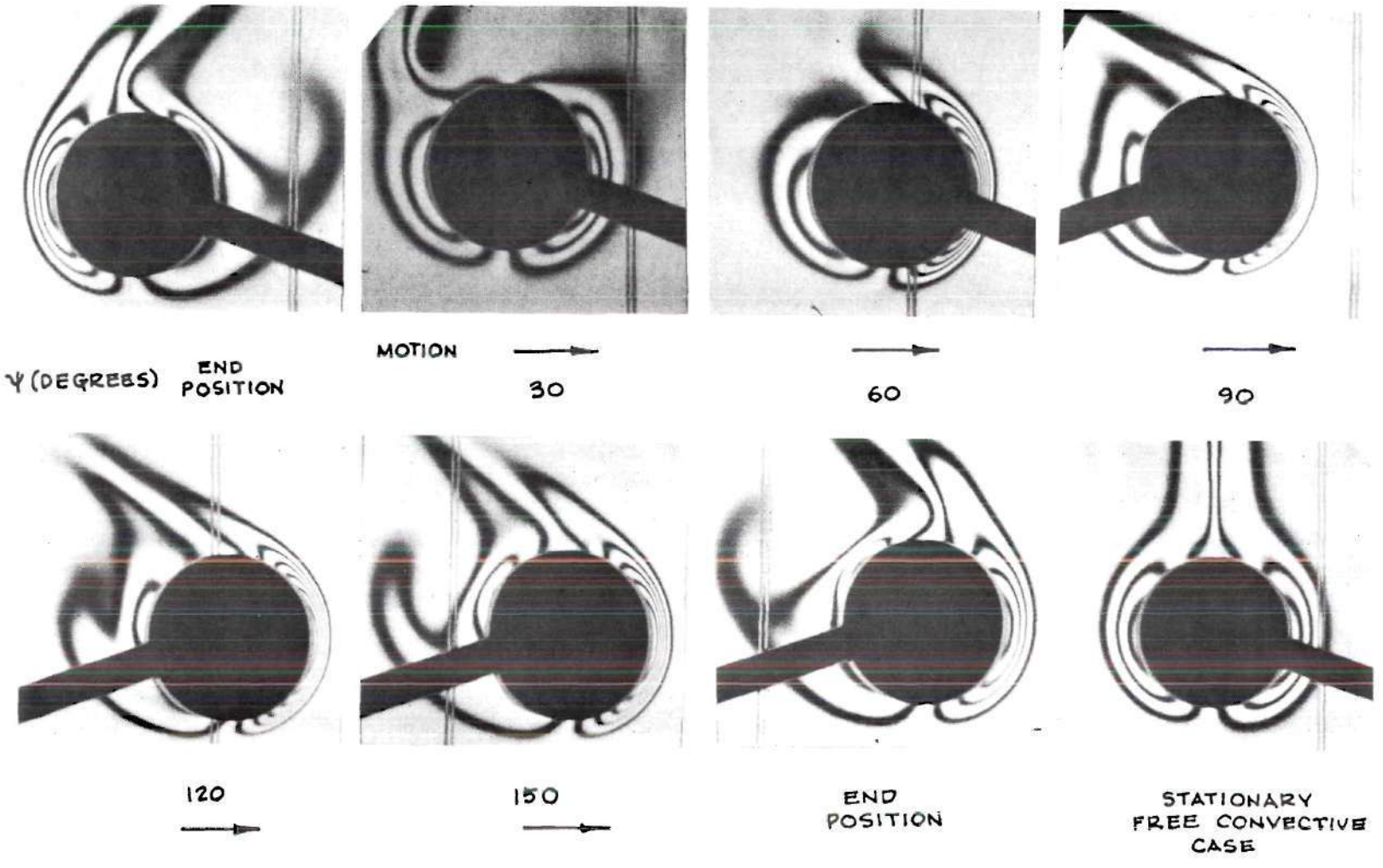

Figure 43. Horizontal Infinite Fringe Interferograms for $\frac{A}{D}$ = 1.77, Re_A = 147, and Gr = 46183

side resembled a forced convective boundary layer.

As the cylinder decelerated, two effects were noticed in the boundary layer on the trailing side. The free convective plume began to move over the top of the cylinder, and the outer part of the boundary layer on the left side began to separate near the center of the left side. As the cylinder approached the extreme right position, the separated flow at the middle of the left side began to reattach, and the mirror image of the flow pattern at the extreme left position was observed.

For intermediate values of Re_A (approximately 300), the flow characteristics for $\frac{A}{D}$ of 0.24 very closely resembled those for low Re_A. For higher $\frac{A}{D}$, the flow patterns had characteristics resembling those for low Re_A, but the forced convective and oscillatory characteristics were more dominant, and the free convective characteristics were less pronounced.

When Re_A was increased to about 600, the free convective characteristics had disappeared in the flow for $\frac{A}{D}$ of 0.39 and 0.51 and were much weaker for $\frac{A}{D}$ of 0.99 and 1.78 but were still present. For Re_A of about 600, the flow pattern for $\frac{A}{D}$ of 0.51 and 1.78 will be described.

The flow patterns for $\frac{A}{D} = 0.51$ and $Re_A = 586$, which correspond to a frequency of oscillation of eight cycles per second, are illustrated in Figure 44. The flow appeared to be completely dominated by oscillatory forces. Free convective effects were minimal since the flow pattern for the

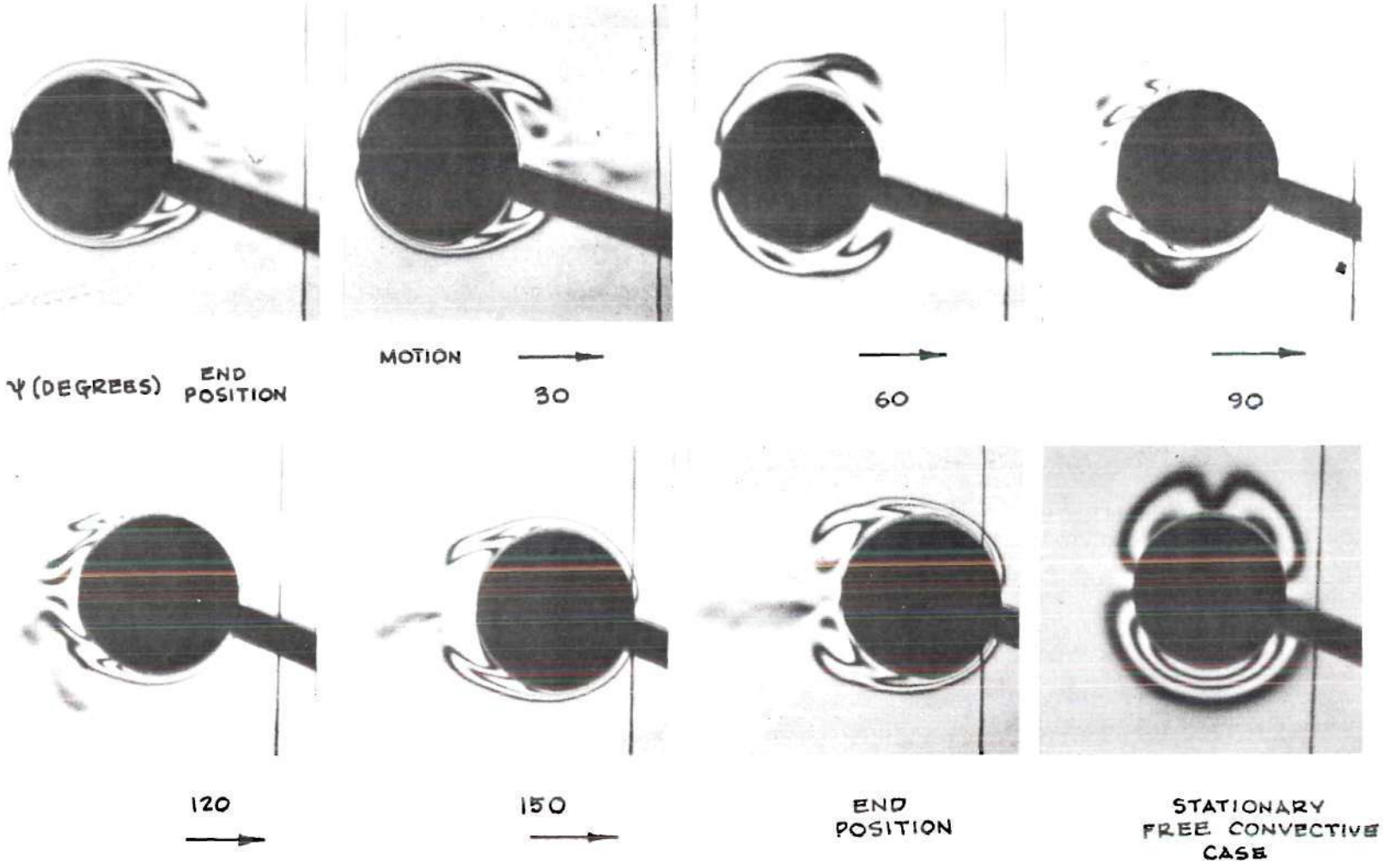

Figure 44. Vertical Infinite Fringe Interferograms for $\frac{A}{D} = 0.51$, $Re_A = 586$, and Gr = 44989

upper and lower halves of the cylinder were nearly symmetrical.

When the cylinder was in the extreme left position, the flow resembled forced flow with boundary-layer separations on the right side of the cylinder near the center of the upper and lower quadrants. However, due to the high deceleration that occurred near the end point of oscillation, the separated flow had begun to overtake the cylinder.

As the cylinder accelerated to the right, the separated flow were forced over the top and under the bottom of the cylinder, and vortices appeared to roll over the top and bottom of the cylinder. The boundary layer on the right side resembled a forced convective boundary layer.

The boundary layer on the left side of the cylinder was also affected by the motion of the cylinder to the right. It thickened and began to separate in the center of the left side, and two regions of separated flow moved in opposite directions until they were positioned in the middle of the upper and lower quadrants of the cylinder. As the cylinder approached the extreme right position, the separated flow began to overtake the cylinder, and the flow pattern resembled the pattern at the left extreme but with left and right sides reversed.

As $\frac{A}{D}$ was increased at high values of Re_A, the free convective influences became noticeable. At $\frac{A}{D} = 1.78$ and $Re_A = 586$, which correspond to a frequency of oscillation of

2.3 cycles per second (see Figure 45), the free convective influences were apparent especially at the extreme positions of oscillations. At the extreme left position, two boundary-layer separations were present. One was located on the left side of the cylinder near the top of the cylinder, and the other was located on the right side near the bottom of the cylinder. The flow above the cylinder appeared to be turbulent.

When the cylinder moved to the right, the upper separated flow was shed behind the cylinder. Part of the lower separated flow was forced under the cylinder, and part was forced around the top. At a Gr of 2.5×10^4, most of the separation was forced under the cylinder, but at a Gr of 4.6×10^4, an appreciable part of the separation was forced around the top. As the cylinder continued to move to the right, the flow resembled forced flow with two regions where the boundary layer separated from the cylinder. Both regions of separated flow trailed the cylinder slanted upward revealing the free convective influences on the flow.

As the cylinder approached the extreme right position, the separated regions moved around the cylinder in opposite directions, but the upper separated flow progressed faster around the top of the cylinder. When the cylinder reached the right extreme position, the flow pattern was identical with the pattern at the left extreme but with left and right sides reversed.

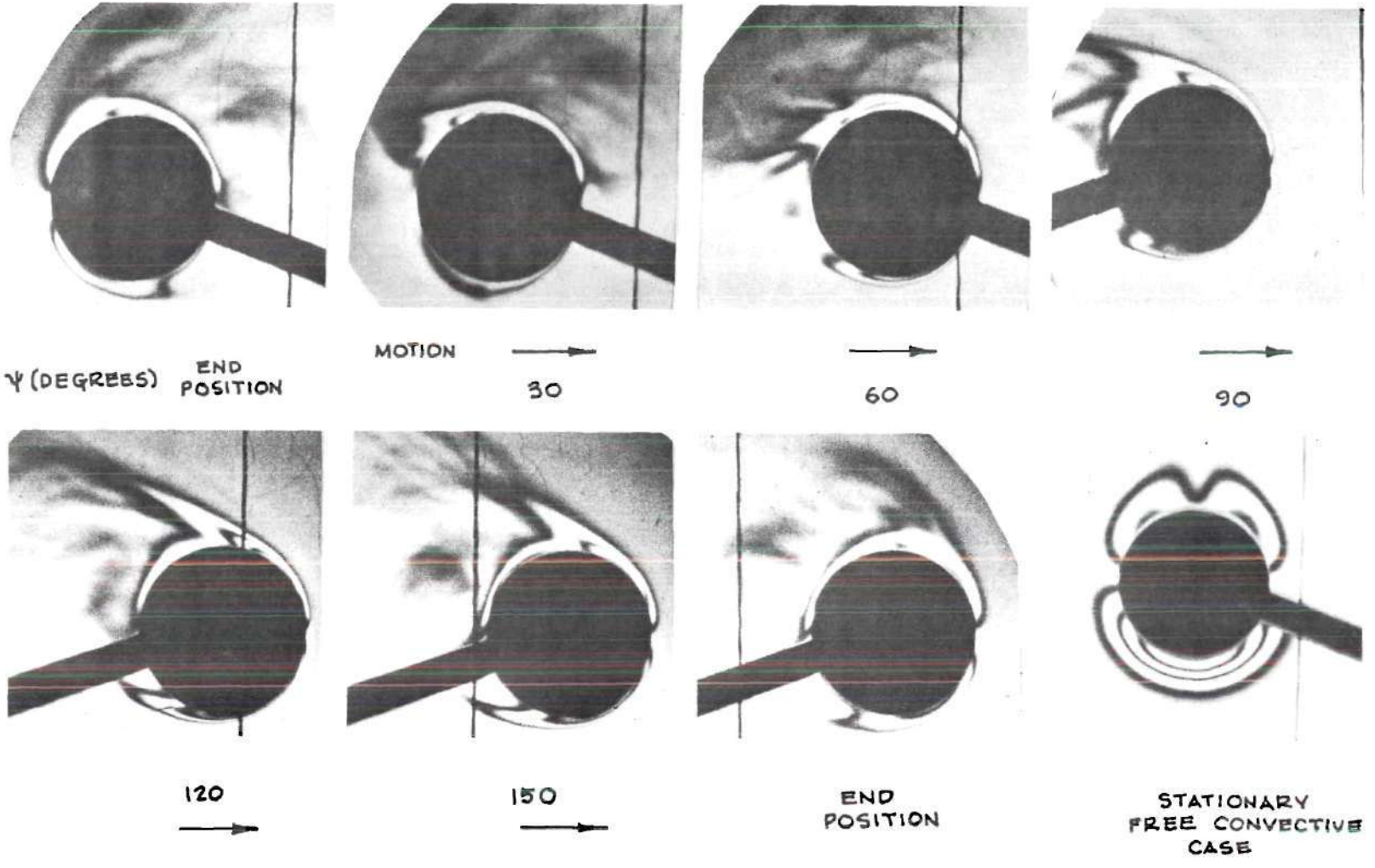

Figure 45. Vertical Infinite Fringe Interferograms for $\frac{A}{D} = 1.78$, $Re_A = 586$, and Gr = 45643

Several basic conclusions can be drawn from the flow visualization study. The heat-transfer mechanism at low $\frac{A}{D}$ (0.12 and 0.24) was primarily free convection with vortex motion in the upper quadrant superposed on the free convection. The range of Re_A was limited at low values of $\frac{A}{D}$ due to the type of vibrational equipment used, and measurements at the critical vibrational level reported in references [1, 4, 12] were unattainable. However, the vortex motion observed on the upper half of the cylinder appeared to be similar to that reported by Richardson [5]. In reference 5, the conclusion was drawn that the changes in the flow pattern from free convection are progressive and that the critical vibration intensity necessary to produce significant increases in the heat-transfer rate is not a sudden phenomenon and therefore has no intrinsic fluid-mechanical significances. Others [1, 4, 12] have claimed that the vortex flow begins to form only when the vibrational intensity has reached a critical value. The flow visualization study appears to substantiate Richardson's conclusion.

For intermediate values of $\frac{A}{D}$ (0.39 and 0.51), the heat-transfer mechanism at low Re_A appears to be a combination of free convection, forced convection, and the oscillatory phenomenon of boundary-layer shedding both at the bottom and top of the cylinder each time the cylinder changes direction. For the same values of $\frac{A}{D}$ but at higher values of Re_A (600) and correspondingly higher frequencies of oscillation, the

heat-transfer mechanism appears to be dominated by the oscillatory phenomenon.

For larger values of $\frac{A}{D}$ (0.99 and 1.78), the heat-transfer mechanism appears to be a combination of free convection, forced convection, and the oscillatory phenomenon. For large values of Re_A (600), free convective effects are less pronounced but are still present.

Discussion of Error Analysis and Reproducibility

The results of an error analysis of the uncertainties involved in the heat-transfer measurements and the reproducibility of the heat-transfer measurement are discussed in this section. Equation (31) in Chapter III gives the relationship for the heat-transfer coefficient in terms of measurable properties, known constants, and the number of fringe shifts. The main sources of error in this equation are the measurement of temperature difference, ΔT, the thermal conductivity, k, and the measurement of fringe shifts, m_s. There are interferometric sources of error which are end effects, the approximation in Equation (19), and refraction. All of these errors are discussed in detail in Appendix I.

A tabulation of estimated errors for instantaneous, local heat-transfer measurements is presented in Table 6. The estimation of these errors are conservative, and in general, the error involved in the instantaneous, local measurements for the vibratory tests should be less than the values stated in the table.

Table 6. Tabulation of Estimated Errors for Instantaneous, Local Heat-Transfer Measurements

Source of Error	ΔT Per Cent	25° Stat.	25° Vib.	50° Stat.	50° Vib.	100° Stat.	100° Vib.
Properties							
1. k		+1.0	+1.0	+1.0	+1.0	+1.0	+1.0
2. ΔT		+2.0	+2.0	+1.0	+1.0	+0.5	+0.5
Interferometric							
1. Fringe Shifts		*	+6.6	*	+3.6	*	+4.2
2. End Effects		+1.6	+0.5	+0.8	+0.5	+0.2	+0.3
3. Approximation $\frac{\partial n}{\partial x} \simeq \frac{\Delta n}{\partial x}$		-0.2	-0.4	+1.4	+1.2	+1.1	+2.2
4. Refraction		0.0	0.0	0.0	0.0	0.0	-0.4
Maximum Total		+4.4	+9.7	+4.2	+7.3	+2.8	+7.8

*Test repeated several times to minimize reading error

Since the instantaneous, average measurements were obtained by averaging 24 instantaneous, local measurements, the errors involved in reading individual fringe shifts tended to cancel. Thus, the instantaneous, average measurements should be more reliable. Further, since overall average measurements were obtained by averaging seven instantaneous, average measurements or by averaging 168 instantaneous, local measurements, the error in reading fringe shifts should be negligible for the overall average measurements. With this assumption, the expected errors in the overall average measurements are 3.1, 3.7, and 3.6 per cent for ΔT of 25, 50, and 100 degrees, respectively.

The reproducibility of the steady state heat-transfer results was checked by conducting each stationary test several times. The local results for each position around the cylinder were averaged to obtain average local Nusselt numbers which were then reliable values for comparison with values of the corresponding vibratory tests. A per cent difference between the averaged local Nusselt number and the individual local values of each test was calculated. The average per cent differences were 3.3, 1.8, and 3.2 per cent for temperature differences of 25, 50, and 100 degrees F, respectively.

An average Nusselt number was calculated for each stationary test by averaging the local Nusselt numbers over the entire cylinder surface. An overall average Nusselt number was calculated for each Grashof number by averaging

these values. A per cent difference between the overall average Nusselt number and the averaged Nusselt number of each test was calculated which resulted in average per cent differences of 1.5, 0.5, and 1.0 per cent for temperature differences of 25, 50, and 100 degrees F, respectively.

Two vibratory tests were repeated to check the reproducibility of the transient heat-transfer measurements. A comparison was made between the values of the original and duplicate tests for three measurements: instantaneous local measurements, instantaneous average measurements, and overall average measurements. Each reproduced test represents a comparison of a total of 168 instantaneous local measurements, 7 instantaneous average measurements, and a single overall average measurement. The parameters for the first reproduced tests were Gr of 46,888, Re_A of 145, and $\frac{A}{D}$ of 1.0. The average differences between the results of the two tests were 5.2, 2.6, and 0.9 per cent for the instantaneous local measurements, instantaneous average measurements, and the overall average measurements, respectively.

The parameters for the second reproduced test was Gr of 25,207, Re_A of 304, and $\frac{A}{D}$ of 0.51. The average differences between the results of the two tests were 9.0, 3.7, and 4.2 per cent for the instantaneous local measurements, instantaneous average measurements, and the overall average measurements, respectively.

CHAPTER VIII

CONCLUSION

The technique of employing a differential interferometer for the measurement of instantaneous, local heat-transfer rates proved to be an accurate method of measuring heat-transfer rates for both steady state and transient problems. The infinite fringe setting of the differential interferometer provided an excellent method of flow visualization for studying the heat-transfer mechanism.

Vibration can significantly affect the heat-transfer rate from an isothermal, horizontal cylinder. The overall heat-transfer rates show moderate increases as the vibrational speed is increased from zero; however, instantaneous, average heat-transfer rates show much larger effects, and the instantaneous, local heat-transfer rates can show significant changes with only small increases in vibrational speed.

For the range of dimensionless parameters investigated, the effect of vibration on the heat-transfer rate varies significantly with the parameters: the Grashof number, the ratio of amplitude of oscillation to cylinder diameter, and an appropriate Reynolds number. A successful correlation of the overall average Nusselt number was achieved as a function of these parameters. The heat-transfer rates for

tests conducted at higher Grashof numbers are less affected by vibration because the free convective characteristics of the flow pattern are more significant. The main effect of increasing the Reynolds number is to reduce the influence that free convection has on the heat-transfer mechanism with a resulting increase in importance of the forced convective and the oscillatory mechanisms. Flow visualization indicated that the heat-transfer mechanism is significantly affected by the ratio of amplitude of oscillation to cylinder diameter and that the type of flow structure around the cylinder shows different characteristics for different ranges of this parameter.

CHAPTER IX

RECOMMENDATIONS

The resolution of the differential interferometer was not sufficient for quantitative measurements for Re_A above approximately 660 (Maximum value of $Re_v(\psi)$ of 1037) at Gr of 2.5×10^4 and 4.5×10^4, but this is probably due to the limitations of the instrument used in this investigation and not to differential interferometers in general. As Re_A is increased, the boundary layer on the leading side of the cylinder becomes thinner and the thermal gradient increases. As a result, the deflection of the fringe lines occurs over a small distance causing the fringe lines to become very closely spaced. When this occurs, the individual fringe lines are not distinct but are hazy and inseparable, making the determination of fringe positions at the surface of the test object very difficult.

Several possible remedies to this problem are suggested for future investigations. One solution is to reduce the prism wedge angle of the first two Wollaston prisms. This would reduce the fringe shifts which would reduce the angle through which the fringe lines are deflected in the boundary layer. A second possibility is to use a filter that produces a longer wavelength of light. This also would reduce the

fringe shifts and would reduce the angle through which the fringe lines are deflected.

A final solution would be to increase the wedge angle of the third Wollaston prism which would increase the number of fringe lines. By increasing the number of fringe lines, the angle through which the fringe lines are deflected is reduced. This solution is suggested over the other solutions since it would reduce the angle through which the fringe lines are deflected without reducing the fringe shifts (or sensitivity) of the instrument.

The differential interferometer could be used to resolve the question of the heat-transfer mechanism at low values of $\frac{A}{D}$ (less than 0.05) that has been a subject of controversy between several investigators [1, 5, 11, 34]. The infinite fringe setting of the differential interferometer could be used to gain valuable insight into the heat-transfer mechanism for this range of $\frac{A}{D}$.

APPENDICES

APPENDIX A

THE WOLLASTON PRISM

The polarizing beam splitters used in the differential interferometer employed in this study were Wollaston prisms. The purpose of this appendix is to discuss the Wollaston prism and its functions in the operation of the differential interferometer. Further discussions of the Wollaston prism can be found in references 60 and 70.

Birefringent Materials

A Wollaston prism is a double prism consisting of two wedges of birefringent material cemented together so the optic axes of the two wedges are perpendicular. A birefringent material is one whose index of refraction depends on the direction of the electric vector of the light ray as it propagates through the medium. Two commonly used birefringent materials are quartz and calcite. For all but one direction of propagation, a plane polarized light ray propagated through the double refracting medium will be split into two refracted rays. These two rays are referred to as the ordinary ray or ray o and the extraordinary ray or ray e. Ray o is called ordinary because it obeys the ordinary laws of refraction. The index of refraction for ray o is a constant and independent of the direction of propagation, but

the index of refraction for ray e varies with the direction of propagation.

The one direction of propagation in which the incoming ray is not split into two rays is called the optic axis of the birefringent material. The basic difference between ray o and ray e is the relative orientation between their electric vectors and the optic axis of the medium. Ray o is the component of the incident ray that has an electric vector perpendicular to the optic axis of the medium. The remaining component of the incident ray is ray e. For a propagation direction along the optic axis, the ray will not split into two rays since the entire electric vector of the ray is perpendicular to the optic axis. For propagation in any other direction, ray e will travel either faster or slower than ray o depending on the birefringent material. In quartz, for example, ray e will travel slower than ray o.

The effective index of refraction or n_{eff} for ray e varies as the radius of an ellipse where the semi-major axis is n_e, and the semi-minor axis is n_o [70] (see Figure 46). The index of refraction n_e is either the maximum or minimum index of refraction of ray e depending upon the birefringent material. For quartz, it is the maximum index of refraction of ray e. The expression for n_{eff} is [70]

$$n_{eff} = \left[\frac{n_e^2 n_o^2}{n_o^2 \cos^2\Lambda + n_e^2 \sin^2\Lambda}\right]^{1/2} \qquad (94)$$

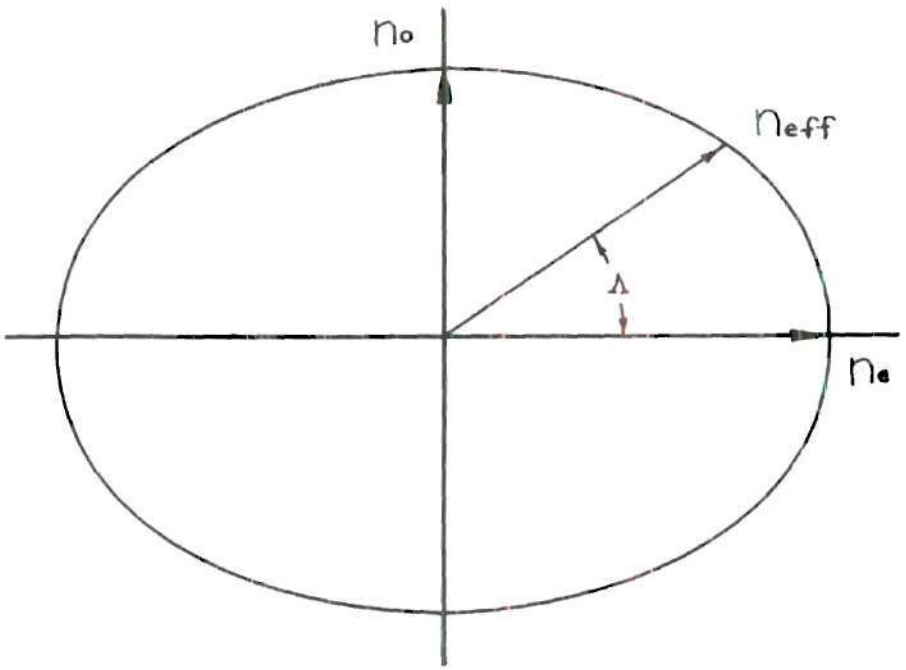

Figure 46. Schematic Diagram of the Effective Index of Refraction

where Λ is the angle between the electric vector of ray e and the optic axis. For the case of $\Lambda \tilde{} 0$, $n_{eff} \tilde{} n_e$.

Separation of Rays

A Wollaston prism arranged as it is in a differential interferometer with a plane polarizer positioned in front of the prism is shown schematically in Figures 47 and 48. The plane of polarization of the polarizer is oriented at an angle of 45 degrees with respect to the optic axes of the Wollaston prism and also with respect to the x and y axes. The optic axis in the first half of the Wollaston prism is parallel to the front face of the prism and is parallel to the x axis. The optic axis in the second half of the prism is parallel to the y axis.

The incident ray is propagated in the z direction and is normal to the front face of the prism. The polarizer has plane polarized the incident ray at an angle of 45 degrees with the x-z plane. Therefore the incident ray has two components with equal magnitude electric vectors E_x and E_y which lie along the x and y axes, respectively. The component with the electric vector E_x will be referred to as ray x, and the component with the electric vector E_y will be referred to as ray y. Since the incident ray is perpendicular to the front face of the prism, neither component is refracted. However, the two rays travel at different velocities in the first half of the prism, and a phase difference is developed

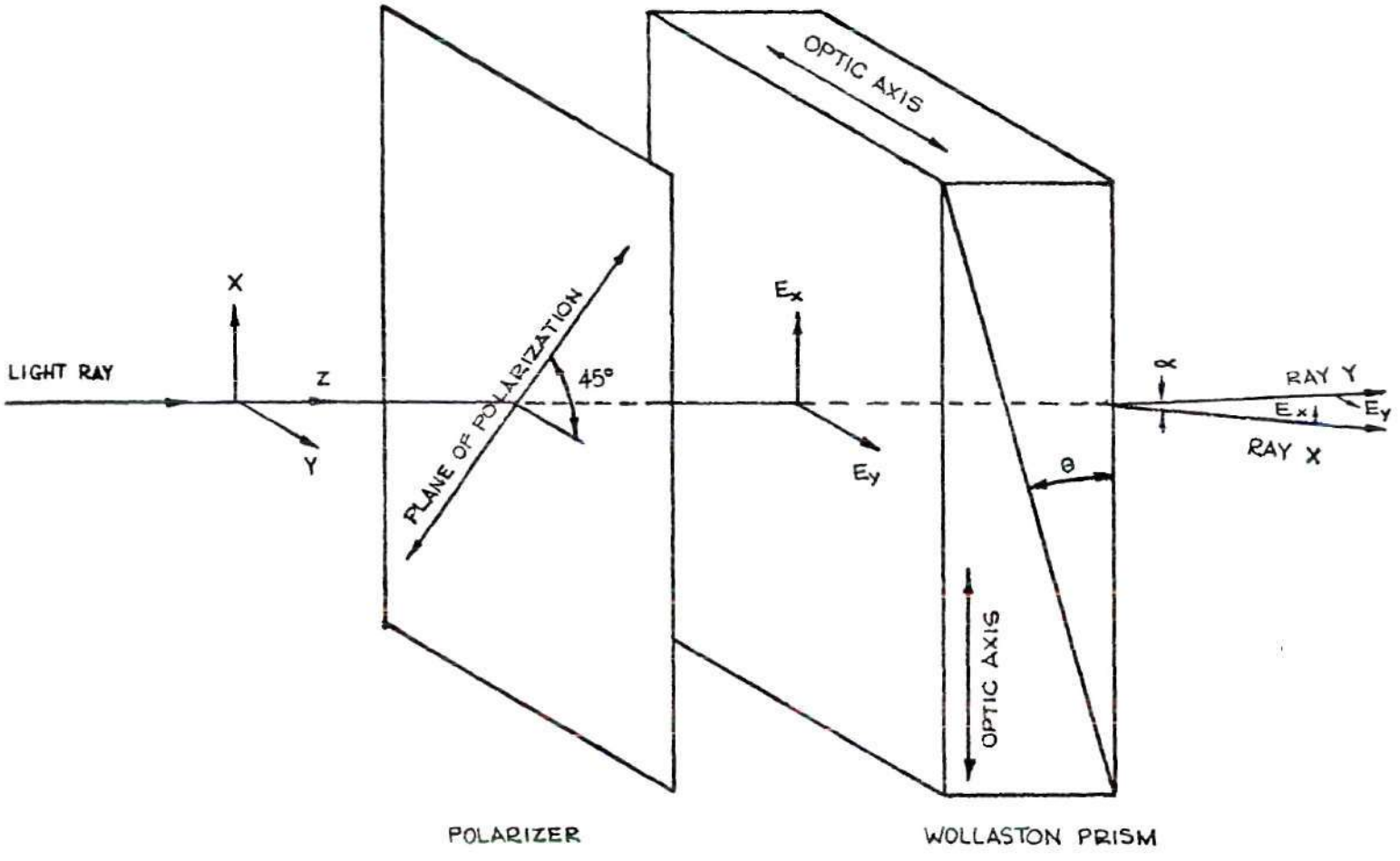

Figure 47. Division of a Single Ray Into Two Components

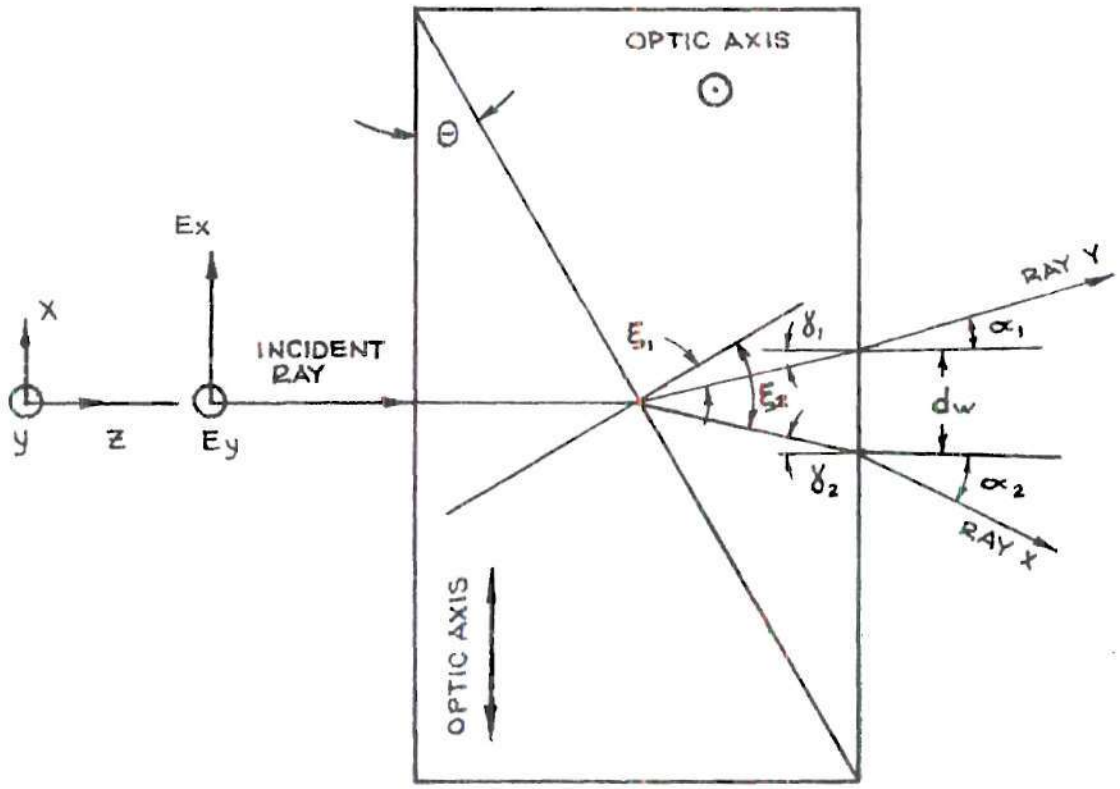

Figure 48. Schematic Diagram of Ray Division by Wollaston Prism

between ray x and ray y. In the first half of the prism, ray y is an ordinary ray since E_y is perpendicular to the optic axis. Thus ray y travels with the velocity

$$(\overline{C}_y)_1 = \frac{\overline{C}}{n_o} \tag{95}$$

where $\overline{C}$ is the velocity of light in a vacuum. Ray x is an extraordinary ray since E_x is parallel to the optic axis. In this case

$$\Lambda = 0 \tag{96}$$

and, therefore, from Equation (94)

$$n_{eff} = n_e \tag{97}$$

Thus ray x travels with the velocity

$$(\overline{C}_x)_1 = \frac{\overline{C}}{n_e} \tag{98}$$

At the intersection of the two halves of the Wollaston prism, ray x and ray y change roles as ordinary and extraordinary rays due to the change in direction of the optic axis. For the second half of the Wollaston prism, ray x is an ordinary

ray since E_x is perpendicular to the optic axis. In the second half of the prism, ray x travels with the velocity

$$(\bar{C}_x)_2 = \frac{\bar{C}}{n_o} \tag{99}$$

Ray y is an extraordinary ray since E_y is parallel to the optic axis. Again

$$\Lambda = 0 \tag{100}$$

and, therefore, from Equation (94)

$$n_{eff} = n_e \tag{101}$$

Thus, ray y travels with the velocity

$$(\bar{C}_y)_2 = \frac{\bar{C}}{n_e} \tag{102}$$

At the intersection of the two halves of the Wollaston prism, the direction of propagation is not perpendicular to the interface of the two halves of the prism. Since the index of refraction changes for both ray x and ray y when passing from the first half of the prism to the second half, double refraction occurs as shown schematically in Figure 48. When

ray x and ray y reach the back face of the Wollaston prism, both are refracted again. Upon leaving the Wollaston prism, ray x and ray y lie in the x-z plane at angles α_2 and α_1, respectively, with the x axis.

Lamb et al. [70] have shown by the application of Snell's law for each ray at each refracting surface that

$$\sin\alpha_1 = -n_o\sin\theta\cos\theta+n_e\sin\theta[1-(\frac{n_o}{n_e})^2\sin^2\theta]^{1/2} \qquad (103)$$

$$\sin\alpha_2 = n_e\sin\theta\cos\theta-n_o\sin\theta[1-(\frac{n_o}{n_e})^2\sin^2\theta]^{1/2} \qquad (104)$$

$$\alpha = \alpha_1+\alpha_2 \qquad (105)$$

These expressions can be used to find the total angle between ray x and ray y. By applying small angle approximations, Equations (103), (104), and (105) may be combined into a simplified expression derived in [70]

$$\alpha = 2(n_e-n_o)\tan\theta \qquad (106)$$

The error involved in this approximation for quartz Wollaston prisms with prism angles of 1, 3, and 8 degrees is 0.04,

0.0004, and 0.002 per cent, respectively.

Ray x and ray y are slightly displaced from each other when they leave the Wollaston prism. This displacement distance is very small compared to the displacement distance between ray x and ray y as they travel through the test section in the interferometer, and it is therefore neglected in the following analysis. The error in neglecting this displacement distance for quartz Wollaston prisms with prism angles of 1, 3, and 8 degrees is estimated to be less than 0.006, 0.017, and 0.046 per cent, respectively.

A value for the angle α was derived for an incident ray that is perpendicular to the front face of the Wollaston prism. Actually, a converging beam enters the prism with rays at some angle ξ with the normal to the face of the prism (see Figure 49). The incident rays in the beam can be considered to be within a cone with an apex angle ξ_{max}. In the present study, $\xi_{max} \cong 2.8$ degrees. The main difference between this case and the simpler case depicted in Figure 48 is the additional ray separation in the left half of the prism. Since the propagation direction is not perpendicular to the optic axis, the index of refraction for ray e is n_{eff} instead of n_e. For this case, Lamb et al. [70] have shown using small angle approximations that

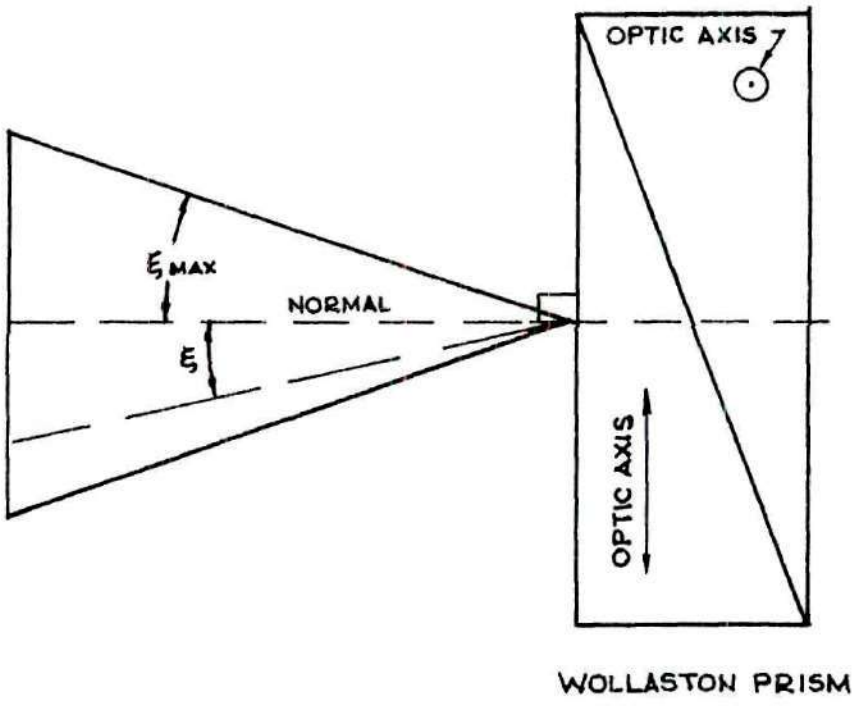

Figure 49. Schematic Diagram of a Converging Beam Entering the Wollaston Prism

$$\alpha_{\xi} = 2(n_e-n_o)\tan\theta-n_e\tan\theta+[n_e^2-(\frac{n_e^2-n_o^2}{n_o^2})\xi^2]^{1/2}\tan\theta \qquad (107)$$

If the formula for α given in Equation (106) is used instead, the fractional error introduced is

$$e_{\alpha} = \frac{n_e-[n_e^2-(\frac{n_e^2-n_o^2}{n_o^2})\xi^2]^{1/2}}{2(n_e-n_o)} \qquad (108)$$

In the present investigation, the maximum error introduced through this approximation is 0.05 per cent.

Wollaston Prism for Fringe Production

For the case where the incident ray enters at the center line of the Wollaston prism, ray x and ray y travel the same distance as ordinary and extraordinary rays. Thus, they leave the Wollaston prism without phase difference.

Figure 50 shows schematically the case where the incident ray is a vertical distance x from the center line of the Wollaston prism. In this case, ray x and ray y do not travel the same distance as ordinary and extraordinary rays. Ray x and ray y leave the Wollaston prism with a phase difference $\Delta\phi_{WP3}$ between them where

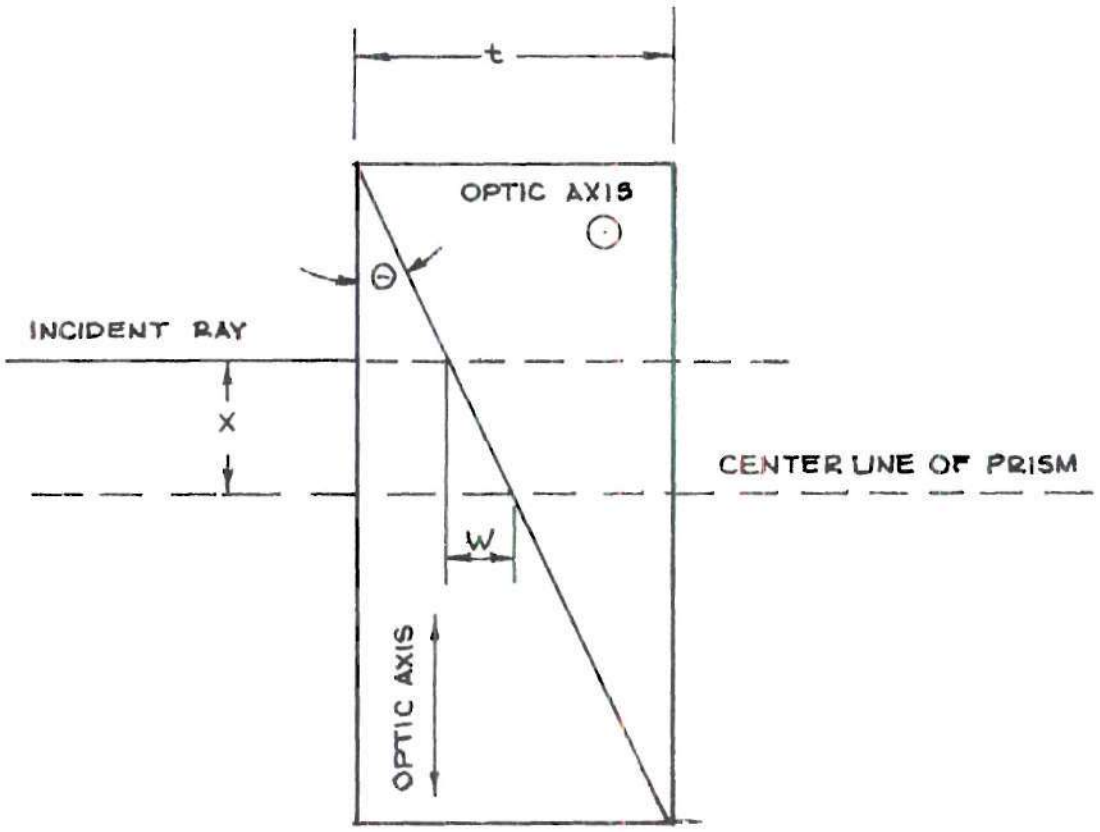

Figure 50. Incident Ray Entering Wollaston Prism
X Distance Above Center Line

$$\Delta\phi_{WP3} = \phi_x - \phi_y \tag{109}$$

The deflection of the rays at the interface of the two halves of the Wollaston prism is so small that it does not need to be considered in the calculation of $\Delta\phi_{WP3}$.

Ray x travels through the Wollaston prism in the time

$$\tau_x = \frac{\frac{t}{2} - W}{(\bar{C}_x)_1} + \frac{\frac{t}{2} + W}{(\bar{C}_x)_2} \tag{110}$$

Using Equations (98) and (99) to substitute for $(\bar{C}_x)_1$ and $(\bar{C}_x)_2$ gives

$$\tau_x = \frac{n_e(\frac{t}{2} - W)}{\bar{C}} + \frac{n_o(\frac{t}{2} + W)}{\bar{C}} \tag{111}$$

Ray y travels through the Wollaston prism in the time

$$\tau_y = \frac{\frac{t}{2} - W}{(\bar{C}_y)_1} + \frac{\frac{t}{2} + W}{(\bar{C}_y)_2} \tag{112}$$

Using Equations (95) and (102) to substitute for $(\bar{C}_y)_1$ and $(\bar{C}_y)_2$ yields

$$\tau_y = \frac{n_o(\frac{t}{2} - W)}{\bar{C}} + \frac{n_e(\frac{t}{2} + W)}{\bar{C}} \qquad (113)$$

The phase difference between ray x and ray y is given by the equation

$$\Delta\phi_{WP3} = \phi_x - \phi_y = \frac{2\pi}{\lambda}\bar{C}(\tau_x - \tau_y) \qquad (114)$$

where λ is the wavelength of light in a vacuum. From Figure 50, it can be seen that

$$W = x\tan\theta \qquad (115)$$

Substitution from Equations (111), (113), and (115) into Equation (114) gives

$$\Delta\phi_{WP3} = \frac{4\pi}{\lambda}(n_o - n_e)x\tan\theta \qquad (116)$$

The sign of the phase difference depends only on the sign of the incident ray position x from the center line of the Wollaston prism. The distance x measured above the center line of the prism is taken as positive, and x measured below the center line is assumed to be a negative quantity. For a given Wollaston prism and wavelength of light, Equation (116)

indicates that $\Delta\phi_{WP3}$ is a linear function of x or

$$\Delta\phi_{WP3} = Fx \tag{117}$$

where the proportionality constant F is given by

$$F = \frac{4\pi}{\lambda}(n_o - n_e)\tan\theta \tag{118}$$

Equation (117) was derived for the case of rays entering perpendicularly to the prism surface, but it is also valid for incident rays with small angles of inclination to the normal of the front face of the Wollaston prism [60].

The plane polarizer whose plane of polarization is oriented at an angle of 45 degrees with the optic axis and also the x and y axes has polarized the incident ray at 45 degrees with the x-y axes. Thus, the electric vectors of ray x and ray y are equal

$$E_x = E_y = E \tag{119}$$

If an analyzer (plane polarizer) is placed behind the Wollaston prism, any phase difference between ray x and ray y can be visualized. An analyzer whose plane of polarization is in the same plane as the polarizer's is shown in Figure 51. When ray x is in phase with ray y, their instantaneous

wave displacements are equal or

$$Y_x = E_x \sin\omega\tau = Y_y = E_y \sin\omega\tau = E\sin\omega\tau \qquad (120)$$

For this case shown in Figure 51, the resultant wave displacement when ray x and ray y pass through the analyzer is

$$Y_{result} = Y_x \cos 45° + Y_y \sin 45° = E\sqrt{2}\sin\omega\tau \qquad (121)$$

If the ray is incident on the prism at some x position other than x equal to zero, there will be a phase difference $\Delta\phi_{WP3}$ between ray x and ray y given by Equation (116). Then, the instantaneous wave displacements are

$$Y_x = E\sin\omega\tau \qquad (122)$$

$$Y_y = E\sin(\omega\tau+\Delta\phi_{WP3}) \qquad (123)$$

Then, the resultant wave displacement when ray x and ray y pass through the analyzer is

$$Y_{result} = Y_x \cos 45° + Y_y \sin 45° =$$

$$\frac{E}{\sqrt{2}}[\sin\omega\tau+\sin(\omega\tau+\Delta\phi_{WP3})] \qquad (124)$$

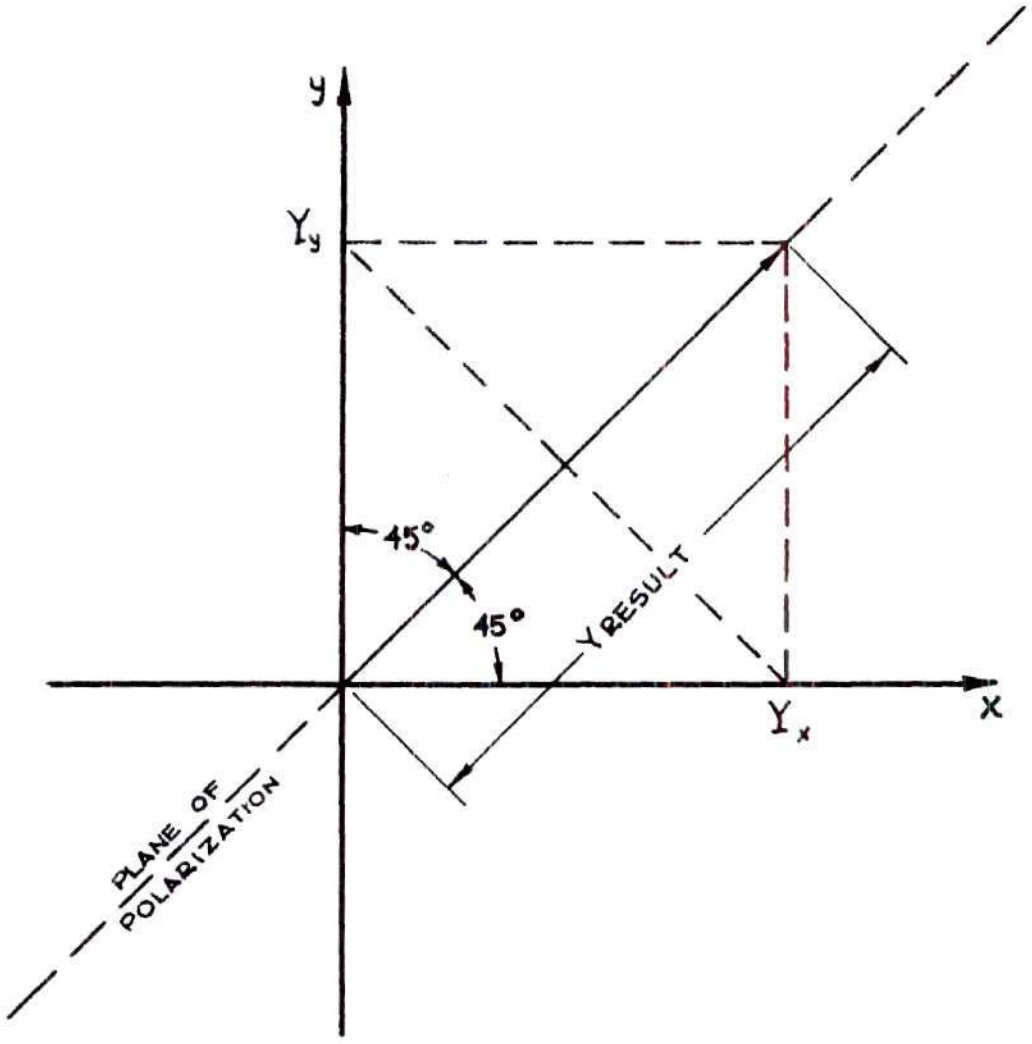

Figure 51. Orientation of Plane of Polarization Of Analyzer

From Equation (124), it is apparent that Y_{result} has maxima for

$$\Delta\phi_{WP3} = 0,\ 2\pi,\ 4\pi,\ldots,\ (p+1)\pi,\ldots \tag{125}$$

and has minima of value 0 for

$$\Delta\phi_{WP3} = \pi,\ 3\pi,\ldots,\ p\pi,\ldots \tag{126}$$

where p is an odd integer.

If the Wollaston prism is illuminated by a beam of light which is parallel to the normal of the front face of the Wollaston prism, a series of fringes parallel to the y direction will be produced as the light leaves the analyzer. The variation in intensity across the fringes is given by the equation [70]

$$I = \frac{E^2}{4}\sqrt{\frac{\varepsilon_p}{\mu_p}}(1+\cos\Delta\phi_{WP3}) \tag{127}$$

where E is the amplitude of the electric vector of the incident ray, ε_p is the permittivity of the medium, and μ_p is the permeability of the medium. For a given light source and medium, Equation (127) can be written

$$I = K(1+\cos\Delta\phi_{WP3}) \tag{128}$$

where K is a constant. When the condition expressed in Equation (126) is satisfied,

$$I = 0 \tag{129}$$

Therefore, positions x that correspond to Equation (126) are positions of zero intensity. At these x positions, black bands extend parallel to the y axis. Similarly, x positions corresponding to Equation (125) are positions of maximum intensity, and at these positions, bright bands run parallel to the y axis.

APPENDIX B

ALIGNMENT PROCEDURES FOR THE DIFFERENTIAL INTERFEROMETER

The use of the differential interferometer required the alignment of the light source and the mirrors as well as adjustment of the optical components before measurements could be obtained. The light beam and mirrors were aligned by placing paper with a small pin hole over the center of the collamator. The light source was then positioned so the small beam of light passing through the pin hole entered the center of the condensing lens. The two spherical and plane mirrors were then carefully adjusted and rotated so that the beam passed through the center of each mirror and through the center of the telescopic objective. When this condition was achieved, the mirrors and light source were considered to be properly aligned.

The procedure for the alignment of the differential interferometer for vertical and horizontal measurements will now be duscussed. The coordinate system (x, y, z) used in this discussion is the same as shown in Figure 47: x is vertical, y is horizontal, and z is the direction of light propagation. When viewed through the eyepiece of a properly aligned interferometer, the observed plane of the test section

contains the x and y coordinates.

A plumb bob was suspended in the test section and used for a vertical reference. The test cylinder was carefully leveled with torpedo levels and used as a horizontal reference in the z direction. Both arms of the interferometer were rotated into the same angular position as indicated by graduated rings placed on each arm. The third Wollaston prism WP3 was removed from the system. The second Wollaston prism was misaligned in the direction of light propagation. This caused the beam to pass through a circular area of WP2. With WP3 removed and the system misaligned, WP2 produced fringes normal to the direction in which the gradient is measured. Since the interferometer was adjusted for horizontal measurements, for a leveled interferometer, the fringes would be vertical and parallel to the plumb bob. The supporting legs on the interferometer were adjusted until the fringes were parallel to the plumb bob and until the cylinder image was sharpest. This insured that the interferometer was aligned properly with all coordinates.

APPENDIX C

EXPERIMENTAL MEASUREMENT OF RAY SEPARATION DISTANCE

An expression for the theoretical separation distance Δx_s between ray x and ray y which travel parallel paths through the test section was given in Equation (4) in Chapter III. An experimental measurement of the separation distance was made to check this relationship. The measurement was made by taking a 4 by 5 inch photograph of a vertical plate suspended in the test section of the interferometer. The interferometer was set to measure gradients in the horizontal direction. With this arrangement, a double image appeared on the vertical edges of the plate as explained in Chapter III. The double image or gray area on the edge of the plate has a theoretical thickness of Δx_s. The negative of the plate was placed under a microscope, and the thickness of the double image of the plate was measured. The uncertainty of the edges of the gray area introduced some error in the measurement. To minimize this error, the thickness of the gray region was measured several times at various positions along the plate and averaged. The differences between the averaged experimental value and the theoretical value were 0.5, 1.1, and 0.8 per cent for Wollaston prism angles of 1, 3, and 8 degrees, respectively. Since these

differences can be accounted for by the uncertainty of the position of the edges of the gray area, the theoretical value of the separation distance was used in all of the calculations.

APPENDIX D

THE PROPERTIES OF AIR

The properties of air used in this investigation are discussed in this appendix. The properties used were the Gladstone-Dale constant, G, the density, ρ, the coefficient of thermal expansion, β, the thermal conductivity, k, and the absolute viscosity, μ_a.

Gladstone-Dale Constant

The Gladstone-Dale constant for air actually is not a constant but is a slight function of the wavelength of the light used and the amount of water vapor present in the air. The wavelength of the light used in this investigation was constant (λ = 5460 $\mathring{A}$). An expression for G for this wavelength was obtained as a function of the partial pressure of water vapor in the air [96]. The expression used was

$$G = 3.6257 \times 10^{-3}(1-0.01007\ P_{vap}) \qquad (130)$$

where G is in ft^3/lbm, and P_{vap} is in lbf/in^2.

Density

The density of air was obtained from the equation of state

$$\rho = \frac{P}{ZR_a T} \tag{131}$$

where Z is the compressibility factor for air [97], P is the absolute pressure, R_a is the gas constant for air, and T is the absolute temperature. For the temperature range and atmospheric pressure which existed during the heat-transfer tests, the compressibility factor for air was assumed to be one for the purposes of density calculations. In other words, the air was assumed to be an ideal gas for the density calculations. The more general equation of state containing the compressibility factor was retained for the calculation of the coefficient of thermal expansion.

Coefficient of Thermal Expansion

The definition of the coefficient of thermal expansion is

$$\beta = -\frac{1}{\rho}\left[\frac{\partial \rho}{\partial T}\right]_P \tag{132}$$

This expression was evaluated using the equation of state (131) so that

$$\beta = \frac{1}{T} + \frac{1}{Z}\left(\frac{\partial Z}{\partial T}\right)_P \tag{133}$$

Data for Z were obtained from reference 97, and a second

order polynomial in temperature was fitted to the data to give an expression for Z(T). This expression was used in Equation (133) to derive an expression for β. The equation used to evaluate β was

$$\beta = \frac{1}{T} - 3.0064 \times 10^{-8}T+2.1398 \times 10^{-5} \qquad (134)$$

where β is in $\frac{1}{\text{degree R}}$ and T is in degree R.

Thermal Conductivity

An expression for the thermal conductivity of atmospheric air was obtained by fitting a second order polynomial in temperature through the data presented in reference 98. The difference between the polynomial fit and the data for a temperature range from 80 to 188 degrees F was less than 0.02 per cent. The expression used to evaluate thermal conductivity of air was

$$k = -7.7296 \times 10^{-9}T^2+3.1904 \times 10^{-5}T+1.3293 \times 10^{-4} \qquad (135)$$

where k is in Btu/(hr-degree R-ft), and T is in degree R.

Absolute Viscosity

The absolute viscosity of air was computed from Sutherland's formula [99] which is

$$\mu_a = 7.3028\left(\frac{T^{3/2}}{T+198.6}\right) \tag{136}$$

where μ_a is in $\frac{\text{lbm}}{\text{sec.-ft}}$, and T is in degrees R.

APPENDIX E

AVERAGE HEAT-TRANSFER COEFFICIENT BY AN ENERGY BALANCE

An average heat-transfer coefficient was calculated by writing an energy balance on the cylinder. The cylinder temperature, ambient air temperature, support temperatures, and energy input to the cylinder were used in this calculation.

The energy losses from the cylinder were due to:

1. Radiative loss from the cylinder
2. Convective end loss
3. Conductive loss through nylon supports
4. Conductive thermocouple lead loss
5. Conductive electrical lead loss

The bulk of the energy losses were due to 1 and 2. The calculation of each of these losses will be briefly discussed.

Radiative Loss From the Cylinder

Radiative losses from the cylinder can be classified as radiation from the cylinder surface and from the exposed end areas. Two assumptions were made in calculating the radiative loss. The assumption was made that the surroundings and the cylinder were gray bodies. The second assumption was that none of the radiation leaving the cylinder would be

reflected back to the cylinder. This assumption was justified by the fact that the surface area of the cylinder was less than 0.05 per cent of the surroundings that it sees, and the surroundings were painted with black paint with an absorptivity of 0.97.

The radiative loss was calculated using the equation

$$Q_{rad} = (A_{sur}+A_{end})(T_s^4-\varepsilon_\infty T_\infty^4)\sigma\varepsilon_{sur} \qquad (137)$$

where A_{sur} is the cylinder surface area, A_{end} is the total exposed cylinder end areas, T_s is the absolute temperature of the surface, ε_∞ is the emissivity of the surroundings, T_∞ is the absolute temperature of the surroundings, σ is the Stefan-Boltzmann constant, and ε_{sur} is the emissivity of the cylinder surface.

The emissivity of the cylinder surface was measured at surface temperatures of 586 and 635 degrees R using a vacuum chamber. The expression used for the emissivity of the surface was

$$\varepsilon_{sur} = 1.03 \times 10^{-4} T_s + 0.0969 \qquad (138)$$

where T_s is in degrees R.

Convective End Loss

Convective losses were present on both ends of the

cylinder. The total convective loss was calculated using the equation

$$Q_{conv} = h_{end} A_{end} (T_s - T_\infty) \qquad (139)$$

where h_{end} is the convective heat-transfer coefficient of the end of the cylinder which was calculated using a relationship for the Nusselt number for a vertical surface given in reference 100, and A_{end} is the total exposed area of both ends of the cylinder.

Conductive Loss Through Nylon Supports

There were conductive losses from both ends of the cylinder through the nylon supports (see Figure 8). The supports were composed of two sections. The first section was nylon, and the second section was nylon with a stainless steel rod along its axis.

An energy balance was performed on both sections of the support for the purpose of determining the temperature gradient in the nylon section. Several assumptions were made in the analysis for both sections: steady state conditions prevailed, no radial or angular variations in temperature at any cross section, constant thermal conductivity, and constant emissivity for the nylon surface. For the first section, the heat loss from the surface of the cylinder was assumed to be due to both radiation and

convection. For the second section, the assumption was made that radiative loss could be linearized and accounted for by multiplying the convective heat-transfer coefficient by a correction factor C_{cor} defined as

$$C_{cor} = \frac{q_{rad}}{q_{conv}} = \frac{\varepsilon_{ny}\sigma(T_t^4 - T_\infty^4)}{h_2(T_t - T_\infty)} \tag{140}$$

where ε_{ny} is the emissivity of nylon, σ is the Stefan-Boltzmann constant, T_t is the temperature at the tip end of section 2, and h_2 is the convective heat-transfer coefficient of section 2 calculated from a relationship for the Nusselt number for a horizontal cylindrical surface given in reference 100.

The temperature gradient in the nylon section at the interface of the nylon section and the end of the cylinder was obtained from the analyses of the two sections using the following boundary conditions: at the interface of nylon section and end of cylinder,

$$T = T_s \tag{141}$$

at the interface of sections 1 and 2,

$$T_1 = T_2 \tag{142}$$

$$q_1 = q_2 \tag{143}$$

where T_1 is the temperature of section 1, T_2 is the temperature of section 2, q_1 is the heat flux in section 1, and q_2 is the heat flux in section 2. At the end of section 2,

$$q_2 = o \tag{144}$$

Once the temperature gradient at the interface of the nylon section and the end of the cylinder was obtained by applying the boundary conditions, the conductive loss through the nylon support was calculated using the equation

$$Q_{cond} = -k_{ny} A_{ny} \left.\frac{\partial T}{\partial x}\right|_{x=o} \tag{145}$$

where k_{ny} is the thermal conductivity of the nylon support, and A_{ny} is the cross sectional area of the nylon support.

The boundary condition (144) was not completely satisfied, so an analysis was made including the heat transfer from the end of the support. Both convection to the air and conduction to the stainless steel support were considered. A comparison was made between the simplified solution and the

solution including the end losses for a surface temperature of the cylinder of 100 degrees F above ambient temperature. The support conduction loss by the two solutions differed by less than 6 per cent. Since the conduction loss from the nylon support was small (less than 15 per cent) compared to the total loss, the simplified boundary condition was used in this calculation.

Thermocouple Lead Loss

Conductive losses through the thermocouples were considered in the energy balance of the cylinder. Energy balances were performed on the wires considering them as cylindrical fins of infinite length. The following assumptions were made: steady state conditions prevailed, no radial variations in temperature at any cross section, constant thermal conductivity, constant emissivity, and radiation could be linearized and accounted for by multiplying the convective heat-transfer coefficient by a correction factor.

The boundary conditions used to solve for the temperature distribution from the energy balance were: at the interface of the wire and the cylinder,

$$T_{wire} = T_s \tag{146}$$

where T_{wire} is the temperature of the wire. At an infinite distance from the cylinder,

$$T_{wire} = T_{\infty} \tag{147}$$

Once the temperature distribution was obtained, the gradient of temperature in the thermocouple wire at the surface of the cylinder was found by differentiation. Then the thermocouple lead loss was computed from the equation

$$Q_{tc} = -Jk_{eq}A_{eq}\left.\frac{dT}{dx}\right|_{x=o} \tag{148}$$

where J is the number of thermocouple wires and

$$k_{eq}A_{eq} = k_{cov}A_{cov}+k_{wire}A_{wire} \tag{149}$$

where k_{cov} is the thermal conductivity of the covering of the wire, A_{cov} is the cross sectional area of the cooling, k_{wire} is the thermal conductivity of the wire, and A_{wire} is the cross sectional area of the wire.

Electrical Lead Loss

Conductive losses through the electrical leads were present. These losses were calculated by performing an energy balance on the electrical leads. The leads were analyzed in two sections. The first section of the lead was inside of the nylon support and considered to conduct axially without losses. The second section was considered as an

infinite cylindrical fin. All of the assumptions made in the thermocouple lead loss analysis were made in the analysis of the electrical lead loss.

The boundary conditions used to solve for the temperature distribution from the energy balance were: at the interface of the wire and the cylinder,

$$T_{wire} = T_s \tag{150}$$

where T_{wire} is the temperature of the wire. At the interface of section 1 and section 2,

$$(T_{wire})_1 = (T_{wire})_2 \tag{151}$$

At an infinite distance from the cylinder,

$$T_{wire} = T_\infty \tag{152}$$

Once the temperature distribution was determined, the temperature gradient in the leads was obtained by differentiation. Then the electrical lead loss was computed from the equation

$$Q_{el} = -2k_{eq}A_{eq}\left.\frac{\partial T}{\partial x}\right|_{x=o} \tag{153}$$

Average Heat-Transfer Coefficient for Stationary Cylinder

The total loss from the cylinder was calculated by summing the losses

$$Q_{loss} = Q_{rad}+Q_{conv}+Q_{cond}+Q_{tc}+Q_{el} \tag{154}$$

The energy loss from the cylinder surface by convection Q_{sur} was the difference between the total energy input to the cylinder Q_{input} minus the total energy loss Q_{loss} or

$$Q_{sur} = Q_{input}-Q_{loss} \tag{155}$$

The average heat-transfer coefficient, $\bar{h}_{bal}$, using the energy balance method was calculated from the equation

$$\bar{h}_{bal} = \frac{Q_{sur}}{A_{sur}(T_s-T_\infty)} \tag{156}$$

where A_{sur} is the surface area of the cylinder. The average Nusselt number $\overline{Nu}_{bal}$ was calculated using $\bar{h}_{bal}$ and Equation (44).

Average Heat-Transfer Coefficient for Vibrating Cylinder

For the vibratory tests, the additional assumption was

made that all of the losses except the radiative loss were effected by vibration by the same magnitude as the free convection from the cylinder surface or

$$Q_{loss} = Q_{rad} + X_n (Q_{conv} + Q_{cond} + Q_{tc} + Q_{el}) \tag{157}$$

where

$$X_n = \frac{\overline{Nu}_{bal}}{\overline{Nu}_F} \tag{158}$$

where $\overline{Nu}_{bal}$ is the Nusselt number of the vibratory test, and $\overline{Nu}_F$ is the Nusselt number of the free convective test conducted at the same Grashof number. Equations (155) through (158) were used for the calculations. An iterative procedure was necessary. After the first iteration X_n was calculated from Equation (158). The iterative process was continued until the calculated value of X_n differed from the previous value of X_n by less than 0.01 per cent.

APPENDIX F

COMPUTER PROGRAM FOR DATA REDUCTION

Since approximately 17,000 deflected fringe measurements were made during the course of experimentation, it was necessary to use a computer program to reduce the data. The computer program was composed of a main program and two subprograms. The first subprogram was an interpolation subroutine that fitted a Q-1 degree polynomial through Q points ($2 \leq Q \leq 10$). A third order polynomial ($Q = 4$) was used for all the interpolations. The subroutine was written so that two points on each side of the interpolation point were used whenever possible. The second subprogram was an integration subroutine based on Simpson's rule.

Data was entered into the program in two groups. The first group contained the cylinder surface temperature, T_s; the ambient air temperature, T_∞; the tip temperature of both nylon supports, T_t; the total rate of energy input to the cylinder, Q_{input}; the atmospheric pressure, P; the vapor pressure of water at dry bulb temperature, P_{vap}; the number of ψ positions analyzed, Q_p; ray separation distance, Δx_s; and the frequency of oscillation, f.

The second group of data was the raw data for the fringe shift measurements. First the positions of the

cylinder relative to the vertical reference for the Q_p analyzed vertical interferograms were entered. Next, the deflected and undeflected vertical fringe data for the Q_p positions were entered. Following the vertical data, the horizontal fringe data were entered.

The purpose of the computer program was to calculate the following quantities:

I. Properties of air (see Appendix D) and the Grashof number Gr, both evaluated at the air film temperature.

II. (1) Vertical and horizontal fringe shifts (see Equation (42)).

(2) Fringe shift data for 15 degree increments in θ.

(3) Amplitude of oscillation (see Equation (45)).

(4) The ψ positions of the seven analyzed interferograms (see Equation (47)).

(5) Interpolated fringe shifts for ψ equal to 0, 30, 60, 90, 120, 150, and 180 degrees.

III. Instantaneous, local heat-transfer coefficients for 15 degree increments of θ beginning at θ equal to 0 degrees and at the seven ψ positions of 0, 30, 60, 90, 120, 150, and 180 degrees. (See Equations (31) and (36).)

IV. Instantaneous, average heat-transfer coefficients for the seven ψ positions from the instantaneous, local heat-transfer coefficients.

V. Average heat-transfer coefficient from the instantaneous, average heat-transfer coefficients.

VI. An energy balance average heat-transfer coefficient using equations in Appendix E and input data.

VII. Nusselt number data by using the heat-transfer coefficient data and Equation (44).

VIII. Per cent difference between

(A) Instantaneous, local Nusselt number and local Nusselt number of stationary cylinder at same Gr and same θ (based on stationary cylinder).

(B) Instantaneous, average Nusselt number and average Nusselt number of stationary cylinder (based on stationary cylinder).

(C) Average Nusselt number of oscillating cylinder and average Nusselt number of stationary cylinder (based on stationary cylinder).

(D) Average interferometric Nusselt number and energy balance average Nusselt number (based on average of the two).

IX. Instantaneous values of $Re_v(\psi)$ and $\frac{Gr}{Re^2_v(\psi)}$ for the seven ψ positions.

X. Average values of Re_A and $\frac{Gr}{Re_A^2}$.

APPENDIX G

IMPORTANT PARAMETERS FROM DIMENSIONLESS GOVERNING EQUATIONS

Dougal et al. [92] have analytically investigated the problem of coupled transverse vibration and free convection from a heated horizontal cylinder. By applying Lin's method [101], they have shown that the product Af is an important parameter for determining the magnitude of changes produced in the steady flow solution by the presence of harmonic oscillations. This fact agrees with experimental observations.

The important dimensionless parameters were obtained by writing the governing equations in non-dimensional form. The curvilinear orthogonal system of coordinates shown in Figure 52 was used.

The reference frame was taken at the surface of the cylinder, that is, to an observer on the cylinder, the cylinder appears stationary, and the fluid a large distance from the cylinder appears to execute harmonic motion. The same results would be obtained as those for a reference frame fixed in space, since an inertia force per unit volume is balanced by an equal pressure gradient. The assumption was made that the cylinder was sufficiently long so that the

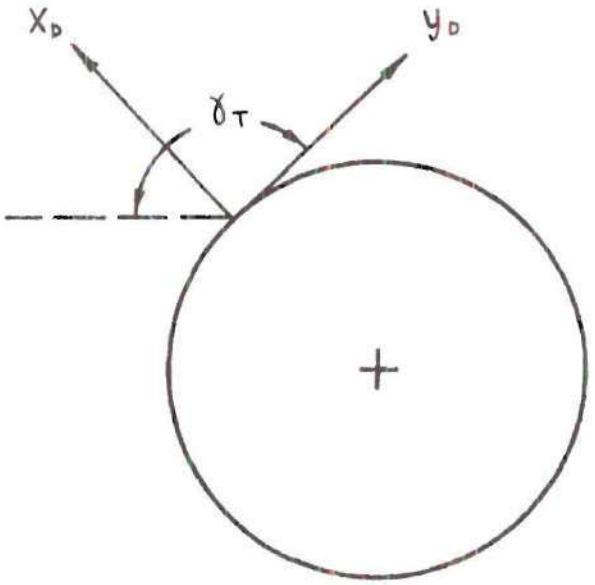

Figure 52. Curvilinear Coordinate System

problem is two-dimensional.

The expressions for the complete Navier-Stokes equations in a curvilinear coordinate system indicated in Figure 52 were written in a modified form. By applying the usual boundary-layer assumptions, assuming the radius of the cylinder was large compared to the boundary-layer thickness, and adding the buoyancy-force term in the momentum equation, the resulting boundary-layer equations are:

Continuity:

$$\frac{\partial u}{\partial x_D} + \frac{\partial v}{\partial y_D} = 0 \tag{159}$$

Momentum:

$$\frac{\partial u}{\partial \tau} + u\frac{\partial u}{\partial x_D} + v\frac{\partial u}{\partial y_D} = -\frac{1}{\rho}\frac{\partial P}{\partial x_D} + \nu\frac{\partial^2 u}{\partial y_D^2} + g_o\beta\theta_T \sin\gamma_T \tag{160}$$

Energy:

$$\frac{\partial \theta_T}{\partial \tau} + u\frac{\partial \theta T}{\partial x_D} + v\frac{\partial \theta_T}{\partial y_D} = \frac{k}{\rho c_p}\frac{\partial^2 \theta_T}{\partial y_D^2} \tag{161}$$

These equations do not apply near the upper part of the cylinder where the normal components of velocity become of the same order of magnitude as the tangential component

since this is contrary to the boundary-layer assumptions.

Outside the boundary layer, the unsteady Bernoulli equation applies

$$-\frac{1}{\rho}\frac{\partial P}{\partial x_D} = \frac{\partial U}{\partial \tau} + U\frac{\partial V}{\partial x_D} \tag{162}$$

The most general boundary conditions are

$$y_D=o;\ u=v=o,\ \theta_T=(\theta_T)_s \tag{163}$$

$$y_D\to\infty;\ u=u(x_D,\tau),\ \theta_T\to o \tag{164}$$

In Dougall et al.'s case and for the situation investigated in this thesis, the boundary condition (164) can be written as

$$y_D\to\infty;\ u\to U=2A\omega\sin\omega\tau\sin(\gamma_T+\lambda_D) \tag{165}$$

where $\lambda=o$ for vertical oscillations, and $\lambda = \frac{\pi}{2}$ for horizontal oscillations.

Dougall et al. obtained a simplification of the differential equations by use of the stream function ψ. The continuity equation is satisfied identically when

$$u = \frac{\partial \psi}{\partial y_D}; \quad v = - \frac{\partial \psi}{\partial x_D} \tag{166}$$

By substituting the expression for the free stream velocity (165) into the unsteady Bernoulli equation, an expression for the pressure term in the momentum equation can be obtained. By using this expression and the stream function, the following governing equations were obtained.

Momentum:

$$\frac{\partial^2 \psi}{\partial y_D \partial \tau} + \frac{\partial \psi}{\partial y_D} \frac{\partial^2 \psi}{\partial y_D \partial x_D} - \frac{\partial \psi}{\partial x_D} \frac{\partial^2 \psi}{\partial y_D^2} =$$

$$2A\omega^2 \cos\omega\tau \sin(\gamma_T + \lambda_D) + \frac{4(A\omega)^2}{R} \sin^2\omega\tau \sin(\gamma_T + \lambda_D)\cos(\gamma_T + \lambda_D)$$

$$+ \nu \frac{\partial^3 \psi}{\partial y_D^3} + g_o \beta \theta_T \sin\gamma_T \tag{167}$$

Energy:

$$\frac{\partial \theta_T}{\partial \tau} + \frac{\partial \psi}{\partial y_D} \frac{\partial \theta_T}{\partial x_D} - \frac{\partial \psi}{\partial x_D} \frac{\partial \theta_T}{\partial y_D} = \frac{k}{\rho c_p} \frac{\partial^2 \theta_T}{\partial y_D^2} \tag{168}$$

Boundary Conditions:

$$y_D=0,\ \frac{\partial\Psi}{\partial x_D} = \frac{\partial\Psi}{\partial y_D} = 0,\ \theta_T=(\theta_T)_s \tag{169}$$

$$y_D\to\infty,\ \frac{\partial\psi}{\partial y_D} \to 2A\omega\ \sin\omega\tau\ \sin(\gamma_T+\lambda_D),\ \theta_T\to 0 \tag{170}$$

Equations (167) through (170) can be written in dimensionless form by making the following substitutions:

$$\overline{\tau} = \omega\tau \tag{171}$$

$$\overline{x}_D = \frac{x_D}{R} \tag{172}$$

$$\overline{y}_D = \alpha_D y_D \tag{173}$$

$$\overline{\Psi} = \frac{1}{\gamma_D}\,\Psi \tag{174}$$

$$\overline{\theta}_T = \frac{\theta_T}{(\theta_T)_s} \tag{175}$$

The dimensionless equations are:

Momentum:

$$\left(\frac{R\omega}{\alpha_D\gamma_D}\right)\ \frac{\partial^2\overline{\psi}}{\partial\overline{y}_D\partial\overline{\tau}} + \frac{\partial\overline{\psi}}{\partial\overline{y}_D}\ \frac{\partial^2\overline{\psi}}{\partial\overline{y}_D\partial\overline{x}_D} - \frac{\partial\overline{\psi}}{\partial\overline{x}_D}\ \frac{\partial^2\overline{\psi}}{\partial\overline{y}_D^{\,2}} =$$

$$2\left(\frac{A\omega^2 R}{\alpha_D^2 \gamma_D^2}\right)\cos\bar{\tau}\ \sin(\gamma_T+\lambda_D)\ +$$

$$4\left(\frac{A\omega}{\alpha_D\gamma_D}\right)^2\sin^2\bar{\tau}\ \sin(\gamma_T+\lambda_D)\ +\ \left(\frac{\nu\alpha_D R}{\gamma_D}\right)\ \frac{\partial^3\bar{\psi}}{\partial\bar{y}_D^3}+$$

$$\frac{g_o\beta(\theta_T)s^R}{\alpha_D^2\gamma_D^2}\ \bar{\theta}_T\sin\gamma_T \tag{176}$$

Energy:

$$\left(\frac{R\omega}{\alpha_D\gamma_D}\right)\ \frac{\partial\bar{\theta}_T}{\partial\bar{\tau}}+\frac{\partial\bar{\psi}}{\partial\bar{y}_D}\ \frac{\partial\bar{\theta}_T}{\partial\bar{x}_D}-\frac{\partial\bar{\psi}}{\partial\bar{x}_D}\ \frac{\partial\bar{\theta}_T}{\partial\bar{y}_D}=\left(\frac{k\alpha_D R}{\rho c_p\gamma_D}\right)\frac{\partial^2\bar{\theta}_T}{\partial\bar{y}_D^2} \tag{177}$$

Boundary Conditions:

$$\bar{y}_D=o,\ \frac{\partial\bar{\psi}}{\partial\bar{x}_D}=\frac{\partial\bar{\psi}}{\partial\bar{y}_D}=o,\ \bar{\theta}_T=1 \tag{178}$$

$$\bar{y}_D\to\infty,\ \frac{\partial\bar{\psi}}{\partial\bar{y}_D}\to 2\left(\frac{A\omega}{\alpha_D\gamma_D}\right)\sin\bar{\tau}\ \sin(\gamma_T+\lambda_D),\ \bar{\theta}_T\to o \tag{179}$$

There are six coefficients in the dimensionless equations to be considered. Since α_D and γ_D used in Equations

(173) and (174) have not been specified, these quantities can be chosen to make as many of the coefficients equal to unity as possible. The maximum number of the six coefficients that can be eliminated simultaneously is two. Four possible choices are presented in Table 7. Four dimensionless parameters fully describe the flow: namely, a fluid parameter represented by the Prandtl number, a temperature parameter represented by the Grashof number, a vibrational parameter represented by the ratio of amplitude to cylinder radius, and a second vibrational parameter represented by one of the four groups in Table 7.

Table 7. Sets of Dimensionless Parameters

Case No.	I	II	III	IV
α_D	$\frac{Gr^{1/4}}{R}$	$\frac{1}{\delta_{ac}}$	$\frac{\sqrt{Re_{osc}}}{R}$	$(\frac{A\omega^2}{\nu^2 R})^{1/4}$
γ_D	νGr	$R\sqrt{\nu\omega}$	$\nu\sqrt{Re_{osc}}$	$(A\omega^2\nu^2 R^3)^{1/4}$
Fluid Parameter	Pr	Pr	Pr	Pr
Temperature Parameter	Gr	Gr	Gr	Gr
Vibrational Parameter	$\frac{A}{R}$ or $\frac{A}{D}$	$\frac{A}{R}$ or $\frac{A}{D}$	$\frac{A}{R}$ or $\frac{A}{D}$	$\frac{A}{R}$ or $\frac{A}{D}$
Vibrational Parameter	$\frac{Re^2_{freq}}{Gr}$	$\frac{1}{Re_{freq}}$	Re_A	$\frac{Re_A}{(\frac{A}{D})^{1/2}}$

APPENDIX H

COMPUTER PROGRAM FOR DATA CORRELATION

A computer program based on a least squares technique [102, 103] was used to determine the coefficient and exponents in Equation (82) to best fit the interferometric, average heat-transfer data. The least square technique can be explained by using the set of simultaneous equations

$$B_i = \sum_j A_{ij} X_j \tag{180}$$

where i is an integer from 1 to $\bar{M}$, j is an integer from 1 to $\bar{N}$, and $\bar{M} \geq \bar{N}$. A_{ij} are known coefficients of the independent variable X_j, and B_i are the known dependent variables.

For $\bar{M} = \bar{N}$, a unique solution for X_j is obtained, but for $\bar{M} \geq \bar{N}$ the solution is overdetermined. For $\bar{M} \geq \bar{N}$, the least square technique determined a solution such that the sum of the squares of the residues $\bar{r}_i$ where

$$\bar{r}_i = B_i - \sum_{j=1}^{\bar{N}} A_{ij} X_j \tag{181}$$

is a minimum. The sum of the squares of the residues

$$S = \sum_{i=1}^{\bar{M}} (\bar{r}_i)^2 = \sum_{i=1}^{\bar{M}} (B_i - \sum_{j=1}^{\bar{N}} A_{ij} X_j)^2 \qquad (182)$$

is a minimum when

$$\frac{\partial s}{\partial x_j} = o \text{ for } 1 \leq j \leq \bar{N} \qquad (183)$$

Equation (183) represents a set of $\bar{N}$ equations that can be solved for the $\bar{N}$ values of $\bar{X}_j$.

APPENDIX I

ERROR ANALYSIS

A systematic analysis of the errors involved in this investigation has been undertaken in order to give an estimation of the accuracy of the measured heat-transfer coefficients. The errors that were considered can be categorized into the following groups:

1.) property errors

2.) fringe shift measurement errors

3.) errors in the approximation $\frac{\partial n}{\partial x_s} \simeq \frac{\Delta n}{\Delta x_s}$

4.) end effect errors

5.) refraction errors

These errors are discussed in the above order in this appendix.

Property Errors

The two property errors are the uncertainties in the value of the thermal conductivity and in the measurement of temperature difference. The uncertainty in the value of thermal conductivity is within ± 1 per cent [98]. Temperature was measured using thermocouples which were calibrated using a silicon constant temperature bath and calibrated thermometers. The uncertainty in the temperature readings is estimated to be less than 0.25 degrees F. For temperature

differences of 25, 50, and 100 degrees F, the uncertainties introduced due to the temperature readings are 2.0, 1.0, 0.5 per cent, respectively.

Fringe Shift Measurement Errors

The procedures for measuring the positions of undeflected and deflected fringes are discussed in Chapter VI. The uncertainties in reading the positions of the undeflected and deflected fringe positions are estimated to be no greater than ± 0.025 and ± 0.05 fringes, respectively, so that the maximum error due to reading fringe shifts is +0.075 fringes or

$$m_\zeta = (m_\zeta)_A \pm 0.075 \text{ fringes} \tag{184}$$

$$m_\eta = (m_\eta)_A \pm 0.075 \text{ fringes} \tag{185}$$

where m_ζ is the measured fringe shift due to horizontal gradients, $(m_\zeta)_A$ is the actual fringe shift due to horizontal gradients, m_η is the measured fringe shift due to vertical gradients, and $(m_\eta)_A$ is the actual fringe shift due to vertical gradients.

The resultant fringe shift at the surface of the cylinder, m_s, is given by Equation (36)

$$m_s = m_\zeta \cos\gamma_R + m_\eta \sin\gamma_R \tag{36}$$

Substitution for m_ζ and m_η from Equations (184) and (185) into Equation (36) yields

$$m_s = (m_\zeta)_A \cos\theta + (m_\eta)_A \sin\theta +$$

$$(0.075)(\cos\theta+\sin\theta) \text{ fringes} \tag{186}$$

The resulting fringe shift error, e_{fs}, due to error in reading fringe positions is then

$$e_{fs} = \pm(0.075)(\cos\theta+\sin\theta) \text{ fringes} \tag{187}$$

The average fringe shift error, $\bar{e}_{fs}$, is obtained by integrating the absolute value of the error over the entire cylinder surface or

$$e_{fs} = \pm\frac{1}{2\pi}\int_0^{2\pi} e_{fs}\,d\theta = \pm 0.0954 \text{ fringes} \tag{188}$$

The average number of fringe shifts for both the stationary tests and vibratory tests was calculated. For the stationary tests, the average numbers of fringe shifts were 2.25, 2.61, and 1.77 for temperature differences of 25, 50, and 100

degrees F, respectively. The resulting uncertainties in the heat-transfer measurements due to fringe shift reading errors were 4.2, 3.7, and 5.4 per cent for temperature differences of 25, 50, and 100 degrees F, respectively. For the vibratory tests, the average numbers of fringe shifts were 1.44, 2.67, and 2.25 for temperature differences of 25, 50, and 100 degrees F, respectively. The resulting uncertainties in the heat-transfer measurements due to fringe shift reading errors were 6.6, 3.6, and 4.2 per cent for temperature differences of 25, 50, and 100 degrees F, respectively.

Error in Assumption $\frac{\partial n}{\partial x_s} \simeq \frac{\Delta n}{\Delta x_s}$

Another source of error is in the approximation of Equation (19)

$$\frac{\partial n}{\partial x_s} \simeq \frac{\Delta n}{\Delta x_s} \tag{19}$$

where n is the index of refraction of air, x_s is the coordinate in the direction in which the gradient is being measured, and Δx_s is the separation distance between ray x and ray y. A Maclauren expansion was written for n about the point $x_s = o$ in terms of Δx_s to obtain an expression for the error due to the approximation. This expression for n is

$$n(\Delta x_s) = n(o)+\Delta x_s n'(o)+ \frac{(\Delta x_s)^2}{2!} n''(o)+ \frac{(\Delta x_s)^3}{3!} n'''(o)+... \quad (189)$$

By rearranging this expression, an equation for the error can be obtained

$$e_{approx} = \left[\frac{\frac{n(\Delta x_s)-n(o)}{\Delta x_s} - n'(o)}{n'(o)}\right] =$$

$$\frac{\frac{\Delta x_s}{2!}n''(o)+ \frac{(\Delta x_s)^2}{3!} n'''(o)+ \frac{(\Delta x_s)^3}{4!} n''''(o)+...}{n'(o)} \quad (190)$$

To determine e_{approx}, the right hand side of Equation (190) was evaluated for two temperature distributions. One of these was a sixth order polynomial curve fit to Chiang and Kaye's [104] theoretical temperature distribution around a free convecting, isothermal cylinder.

$$\frac{T-T_\infty}{T_s-T_\infty} = 1 - 2.2212 \left(\frac{x_s}{\delta}\right) - 0.0181 \left(\frac{x_s}{\delta}\right)^2 + 0.3499 \left(\frac{x_s}{\delta}\right)^3$$

$$+ 9.8081 \left(\frac{x_s}{\delta}\right)^4 - 12.3172 \left(\frac{x_s}{\delta}\right)^5 + 3.8238 \left(\frac{x_s}{\delta}\right)^6 \quad (191)$$

The second temperature distribution was a cubic parabala satisfying the boundary conditions of boundary-layer flow.

$$\frac{T-T_s}{T_s-T_\infty} = -\frac{3}{2}\left(\frac{x_s}{\delta}\right) + \frac{1}{2}\left(\frac{x_s}{\delta}\right)^3 \qquad (192)$$

By relating the index of refraction to temperature through the Lorenz-Lorentz Equation (24), the temperature distributions given in Equations (191) and (192) can be used to evaluate e_{approx} given in Equation (190). The resulting expression for e_{approx} using the temperature distribution given in Equation (191) is

$$e_{approx} = \left(\frac{\Delta x_s}{\delta}\right)\left(2.2212\ \bar{\theta}_s + 0.0181\right)$$

$$+ \left(\frac{\Delta x_s}{\delta}\right)^2\left(4.9337\ \bar{\theta}_s^{\,2} + 0.03629\ \bar{\theta}_s - 0.1575\right)$$

$$+ \left(\frac{\Delta x_s}{\delta}\right)^3\left(-10.9588\ \bar{\theta}_s^{\,3} + 0.1209\ \bar{\theta}_s^{\,2} - 0.6997\ \bar{\theta}_s - 4\ 4156\right)$$

$$+ \left(\frac{\Delta x_s}{\delta}\right)^4\left(24.3421\ \bar{\theta}_s^{\,4} + 0.3581\ \bar{\theta}_s^{\,3} - 19.6221\ \bar{\theta}_s + 5.5450\right)$$

$$+ \ldots \qquad (193)$$

where

$$\bar{\theta}_s = \frac{T_s-T_\infty}{T_s} \qquad (194)$$

The result using the temperature distribution in Equation (192) is

$$e_{approx} = \{ (\frac{\Delta x_s}{\delta}) \ (1.5000 \ \overline{\theta}_s) + (\frac{\Delta x_s}{\delta})^2 \ (2.5000 \ \overline{\theta}_s^2 - 0.3333)$$

$$+ (\frac{\Delta x_s}{\delta})^3 \ (3.3750 \ \overline{\theta}_s^3 - \overline{\theta}_s) + (\frac{\Delta x_s}{\delta})^4 \ (5.0625 \ \overline{\theta}_s^4 + 2.2500 \ \overline{\theta}_s^2)$$

$$+ \ldots \} \qquad (195)$$

These equations indicate that the error due to the approximation in the gradient of the index of refraction is a function only of a temperature parameter, $\overline{\theta}_s$, and a ratio of the ray separation distance to the boundary-layer thickness, $(\frac{\Delta x_s}{\delta})$. Using interferograms, the boundary-layer thickness, δ, was measured on the leading side of the cylinder at the center of oscillation. The boundary-layer thickness is thinnest here, and the interferometric errors are maximum. For all three Grashof numbers, average values of δ and Δx_s were calculated to provide values of $(\frac{\Delta x_s}{\delta})$ to compute the interferometric errors.

Several values of e_{approx} are tabulated in Table 8 for both temperature distributions. Values of e_{approx} were calculated using Equation (193) for the stationary tests and Equation (195) for the vibratory tests.

Table 8. Tabulation of e_{approx} as a Function of $\frac{\Delta x_s}{\delta}$ For Three Temperature Differences

$\frac{\Delta x_s}{\delta}$	e_{approx} (per cent)					
	Temperature Distribution in Equation (191) ΔT(°F)			Temperature Distribution in Equation (192) ΔT(°F)		
	25	50	100	25	50	100
0.05	0.5	1.0	1.8	0.3	0.6	1.1
0.10	0.6	1.6	3.2	0.4	1.0	2.1
0.15	0.2	1.3	4.0	0.2	1.2	2.9
0.20	-1.1	0.7	4.0	0.0	1.2	3.5
0.25	-3.1	-1.0	2.8	-0.1	1.1	4.0

End Effect Errors

In the theoretical discussion, the temperature fields in the test section are considered to be two dimensional. Variations in the direction of the light propagations were neglected. Due to the finite length of the test object, this assumption is not valid, because an additional optical path difference between ray x and ray y is introduced at the ends of the cylinder. The error introduced due to end effects has been analyzed in reference [82] for a single Wollaston prism schlieren interferometer. This analysis also applies to the differential interferometer. The assumptions made in reference [82] are: 1.) at the end of the test section the boundary layer forms an arc with its center at the edge of the test section; 2.) a temperature distribution of

$$\frac{T-T_\infty}{T_s-T_\infty} = (1 - \frac{x_s}{\delta})^2 \qquad (196)$$

and 3.) the index of refraction and temperature can be related through the expression

$$n-n_\infty = \frac{\partial n}{\partial T} (T-T_\infty) \qquad (197)$$

With these assumptions, the fractional fringe shift error due to end effects was derived in reference [82] as

$$e_{end} = \left[\frac{2\left(\frac{\delta}{L}\right)}{\left(\frac{\Delta x_s}{\delta}\right)\left(2 - \frac{\Delta x_s}{\delta}\right)}\right]$$

$$\left\{\frac{[1-(sq)]}{3} + \left[\frac{\Delta x_s}{\delta}\right]^2 \left[\ln\left(\frac{1+(sq)}{\frac{\Delta x_s}{\delta}}\right) - \frac{2}{3}(sq)\right]\right\} \qquad (198)$$

where

$$sq = \left[1 - \left(\frac{\Delta x_s}{\delta}\right)^2\right]^{1/2} \qquad (199)$$

Values of e_{end} versus $\frac{\Delta x_s}{\delta}$ for several values of $\frac{\delta}{L}$ are presented in Table 9.

Refraction

Refraction occurs when a gradient in the index of refraction normal to the light path exists which results in a curvature in the light ray path (see Figure 53). When a thermal boundary layer exists on the surface of a test body, a gradient in the index of refraction normal to the light ray path is present. For a heated test object, the light ray path curves away from the test object. Since the optical paths of the refracted ray path and the unrefracted ray path are different, an error in the fringe shift may exist.

The problem of refraction error in interferometry of boundary layers has been investigated in detail by Wachtell

Table 9. Tabulation of e_{end} as a Function of $\frac{\Delta x_s}{\delta}$ for Several Values of $\frac{\delta}{L}$

$\frac{\Delta x_s}{\delta}$	e_{end} (per cent) $\frac{\delta}{L}$					
	0.005	0.010	0.015	0.020	0.025	0.03
0.05	0.1	0.2	0.2	0.3	0.4	0.5
0.10	0.1	0.3	0.4	0.5	0.7	0.8
0.15	0.2	0.3	0.5	0.7	0.8	1.0
0.20	0.2	0.4	0.6	0.8	1.0	1.2
0.25	0.2	0.5	0.7	0.9	1.1	1.4

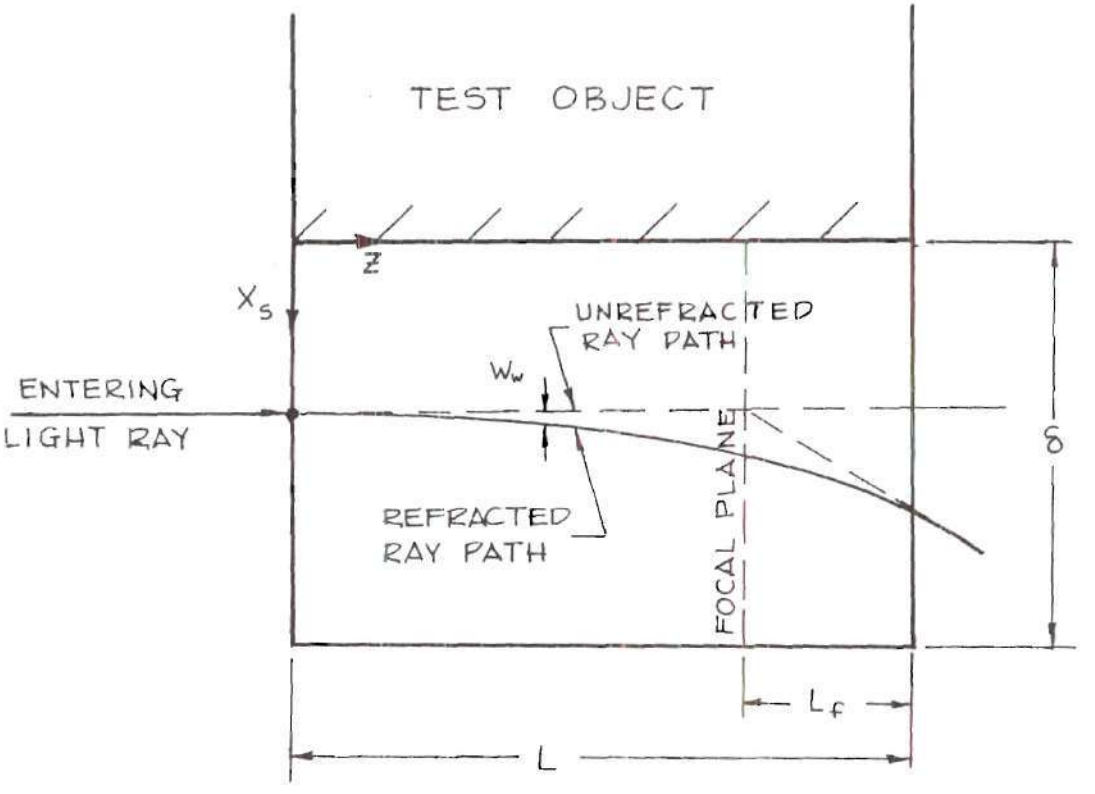

Figure 53. Schematic Diagram of a Refracted Ray Passing Through a Thermal Boundary Layer

[105]. The main assumptions in Wachtell's analysis are:

1.) n depends only on $\frac{x_s}{\delta}$

$$n = n\left(\frac{x_s}{\delta}\right) \tag{200}$$

2.) n can be expressed by a power series

$$\frac{n}{n_{ref}} = b_o + b_1 w_w + b_2 w_w^2 + b_3 w_w^3 + \ldots \tag{201}$$

where n_{ref} is the index of refraction of the medium at the position where the light ray first enters the boundary layer, w_w is the position perpendicular to the surface of the test object and is zero where the individual light ray enters the boundary layer, and b_o, b_1, b_2, b_3,... are constants.

3.) the position w_w of the refracted light ray can be expressed in the form

$$w_w = a_o + a_1 z + a_2 z^2 + a_3 z^3 + \ldots \tag{202}$$

where z is the coordinate in the direction of light propagation, and a_o, a_1, a_2, a_3,... are constants. With these assumptions, the change in optical path of any ray at the photographic plane due to refraction was derived by Wachtell as

$$\Delta \ell_{ref} = b_1{}^2 L^3 \{ (\frac{\alpha_w}{2} - \frac{1}{6}) + L^2 b_2 (-\alpha_w{}^2 + \alpha_w - \frac{1}{5})$$

$$+L^4 [b_2{}^2 (-\frac{2}{3}\alpha_w{}^2 + \frac{4}{9}\alpha_w - \frac{4}{63}) + b_1 b_3 (\alpha_w{}^3 - \frac{3}{2}\alpha_w{}^2 + \frac{3}{4}\alpha_w - \frac{3}{28})]\}$$

$$+ \ldots \qquad (203)$$

where

$$b_o = 0 \qquad (204)$$

$$b_1 = \frac{1}{n_{ref}} (\frac{\partial n}{\partial w_w})_{w_w=o} \qquad (205)$$

$$b_2 = \frac{1}{2n_{ref}} (\frac{\partial^2 n}{\partial w_w{}^2})_{w_w=o} \qquad (206)$$

$$b_3 = \frac{1}{6n_{ref}} (\frac{\partial^3 n}{\partial w^3})_{w_w=o} \qquad (207)$$

$$\alpha_w = \frac{L_f}{L} \qquad (208)$$

where L_f is the distance from the end of the test object nearest to the camera to the object plane, and L is the length of the test object in the direction of light propagation.

For this investigation, α_w was 1/3. If α_w is selected as 1/3, $\Delta \ell_{ref}$ is zero in the first approximation; however,

the following refraction error analysis was carried out to insure higher order effects were negligible.

The theoretical optical path difference between ray x and ray y is given by Equation (5) in Chapter III as

$$\Delta\ell = \Delta[(n_{ray\ x} - n_{ray\ y})L] = (\Delta n)L \tag{3}$$

The actual optical path difference including refraction effects is

$$\Delta\ell_A = \Delta\ell + (\Delta\ell_{ref_{ray\ x}} - \Delta\ell_{ref_{ray\ y}}) \tag{209}$$

Then, the error due to refraction is

$$e_{ref} = \frac{\Delta\ell_A - \Delta\ell}{\Delta\ell} = \frac{(\Delta\ell_{ref_{ray\ x}} - \Delta\ell_{ref_{ray\ y}})}{\Delta\ell} \tag{210}$$

The refraction error was calculated using Equations (3), (203) through (208), and (210), and the temperature distributions given in Equations (191) and (192). The refraction errors were less than 0.1 per cent for all cases except the vibrating tests at Gr of approximately 7.5×10^4. In this case, the maximum refraction error was approximately -0.4 per cent.

BIBLIOGRAPHY

1. Fand, R. M., "Mechanism of Interaction between Vibrations and Heat Transfer," *The Journal of the Acoustical Society of America*, Volume 34, pages 1887-1894, 1962.

2. Westervelt, P. J., "The Effects of Sound Waves on Heat Transfer," *The Journal of the Acoustical Society of America*, Volume 32, pages 337-338, 1960.

3. Sprott, A. C., Holman, J. P., and Durand, F. L., "An Experimental Study of the Effects of Strong Progressive Sound Fields on Free-Convection Heat Transfer from a Horizontal Cylinder," ASME Paper No. 60-HT-19, presented at the ASME-AIChE Heat Transfer Conference, Buffalo, New York, August, 1960.

4. Fand, R. M. and Kaye, J., "Acoustic Streaming Near a Heated Cylinder," *The Journal of the Acoustical Society of America*, Volume 32, pages 579-584, 1960.

5. Richardson, P. D., "Influence of Sound Upon Local Heat Transfer from a Cylinder," *The Journal of the Acoustical Society of America*, Volume 36, pages 2323-2327, 1964.

6. Richardson, P. D., "Local Details on the Influence of a Vertical Sound Field on Heat Transfer from a Circular Cylinder," *Proceedings of the Third International Heat Transfer Conference*, pages 71-77, 1966.

7. Richardson, P. D., "The Effect of Vibration and Oscillations on Heat Transfer from a Circular Cylinder," Brown University, Division of Engineering, Report, AF USAF Research Laboratories, ARL 66-0235, 1966.

8. Richardson, P. D., "Effects of Sound and Vibrations on Heat Transfer," *Applied Mechanics Review*, Volume 20, pages 201-207, 1967.

9. Richardson, P. D., "Heat Transfer from a Circular Cylinder by Acoustic Streaming," *Journal of Fluid Mechanics*, Volume 30, pages 337-355, 1967.

10. Davis, G. and Richardson, P. D., "Natural Convection from a Horizontal Cylinder in the Presence of a Sound Field Giving Large Streaming Reynolds Numbers," Brown University, Division of Engineering, Report AF 175413, 1967.

11. Richardson, P. D., "Local Effects of Horizontal and Vertical Sound Fields on Natural Convection from a Horizontal Cylinder," *Journal of Sound Vibrations*, Volume 10, pages 32-41, 1967.

12. Fand, R. M., Roos, J., Cheng, P., and Kaye, J., "The Local Heat-Transfer Coefficient Around a Heated Horizontal Cylinder in an Intense Sound Field," *ASME Journal of Heat Transfer*, Volume 84, pages 245-250, 1962.

13. Richards, R. C., "The Resistance of a Hot Wire in an Alternating Air Current," *Philosophical Magazine and Journal of Science*, Volume 45, pages 926-934, 1923.

14. Maxwell, R. S., "The Escape of Heat from a Harmonically Oscillating Hot Wire," *Philosophical Magazine and Journal of Science*, Volume 6, pages 945-965, 1928.

15. Martinelli, R. C. and Boelter, L. M. K., "The Effect of Vibration on Heat Transfer by Free Convection from a Horizontal Cylinder," *Proceedings of the Fifth Congress of Applied Mechanics*, pages 578-584, 1938.

16. Mason, W. E. and Boelter, L. M. K., "Vibration, Its Effect on Heat Transfer," *Power Plant Engineering*, pages 43-44, 1949.

17. Lemlich, R., "The Effect of Vibration, Its Effect on Heat Transfer," Ph.D. Thesis, University of Cincinnati, 1954.

18. Lemlich, R., "Effect of Vibration on Natural Convective Heat Transfer," *Industrial and Engineering Chemistry*, Volume 47, pages 1175-1180, 1955; Errata Volume 53, page 314, 1961.

19. Hutton, Jr., J. E., "The Effect of Transverse Vibrations on the Heat Transfer Rate from a Heated Horizontal Cylinder in Free Convection," M.S. Thesis in Mechanical Engineering, United States Air Force Institute of Technology, 1958.

20. Eisele, D. F., "The Effect of Vibrations on the Heat Transfer Rate from Cylinders in Free Convection," M.S. Thesis in Mechanical Engineering, United States Air Force Institute of Technology, 1960.

21. Teleki, C., Fand, R. M., and Kaye, J., "Influence of Vertical Vibrations on the Rate of Heat Transfer from a Horizontal Cylinder in Air," Wright Air Development Command, TN 59-357, 1960.

22. Fand, R. M. and Kaye, J., "The Influence of Vertical Vibrations on Heat Transfer by Free Convection from a Horizontal Cylinder," *International Developments in Heat Transfer*, International Heat Transfer Conference, pages 490-498, 1961.

23. James, E. C., "The Effect of Vibration on the Heat Transfer Rate from Cylinders in Free Convection," M.S. Thesis, United States Air Force Institute of Technology, 1961.

24. Deaver, F. K., Penney, W. R., and Jefferson, T. B., "Heat Transfer from an Oscillating Horizontal Wire to Water," *ASME Journal of Heat Transfer*, Volume 84, pages 251-256, 1962.

25. Fand, R. and Pebbles, E. M., "A Comparison of the Influence of Mechanical and Acoustical Vibration on Free Convection from a Horizontal Cylinder," *ASME Journal of Heat Transfer*, Volume 84, page 268, 1962.

26. Russ, R. M., "Effect of Vibration on Heat Transfer from Cylinders in Free Convection," M.S. Thesis in Mechanical Engineering, United States Air Force Institute of Technology, 1962.

27. Neely, D. F., "Effect of Vibration on Heat Transfer from Cylinders in Free Convection," M.S. Thesis in Mechanical Engineering, United States Air Force Institute of Technology, 1964.

28. Lemlich, R. and Rao, M. A., "The Effect of Transverse Vibration from a Horizontal Cylinder," *International Journal of Heat and Mass Transfer*, Volume 8, Pergamon Press, pages 27-33, 1965.

29. Lemlich, R. and Levy, M. R., "The Effect of Vibration on Natural Convection Mass Transfer," *American Institute of Chemical Engineers Journal*, Volume 7, pages 240-242, 1961.

30. Penney, W. R. and Jefferson, T. B., "Heat Transfer from an Oscillatory Horizontal Wire to Water and Ethylene Glycol," *ASME Journal of Heat Transfer*, Volume 88, pages 359-366, 1966.

31. Thrasher, B. H. and Schaetzle, W. J., "Instantaneous Measurement of Heat Transfer from an Oscillating Wire in Free Convection," ASME Paper No. 69-WA/HT-15.

32. Armaly, B. F. and Madsen, D. H., "Heat Transfer from an Oscillating Horizontal Wire," *ASME Journal of Heat Transfer*, Volume 93, pages 239-240, 1971.

33. Grigull, U. and Hahne, E., editors, *Progress in Heat and Mass Transfer*, Bergles, A. E., "Survey and Evaluation of Techniques to Augment Convective Heat and Mass Transfer," Volume 1, pages 331-424, 1969.

34. Fand, R. M., "Comments on 'Influence of Sound Upon Local Heat Transfer from a Cylinder', [P. D. Richardson, *The Journal of the Acoustical Society of America*, Volume 36, pages 2323-2327, 1964]," Volume 65, pages 370-372, 1965.

35. Kennard, R. B., "An Optical Method for Measuring Temperature Distribution and Convective Heat Transfer," *Bureau of Standards Journal of Research*, Volume 8, pages 287-805, 1932.

36. Kennard, R. B., "Temperature Distribution and Heat Flux in Air by Interferometry," *Temperature, Its Measurement and Control in Science and Industry*, Reinhold Publishing Corporation, New York, Volume 1, pages 685-706, 1941.

37. Hansen, G., *Feischrist Für Schweisstechnik, Physik*, Volume 12, page 436, 1931.

38. Eckert, E. R. G., Drake, R. M., and Soehngen, E., "Manufacture of a Zehnder-Mach Interferometer," AF Technical Report Number 5721, 1948.

39. Eckert, E. R. G. and Soehngen, E. E., "Studies of Heat Transfer in Laminar Free Convection with the Zehnder-Mach Interferometer," AF TR-5747, Wright Patterson Air Force Base, Ohio, December, 1948.

40. Eckert, E. R. G., "Interferometric Studies of Beginning Turbulence in Free and Forced Convection Boundary Layers on a Heated Plate," Heat Transfer and Fluid Mechanics Institute, Berkeley, California, 1949.

41 Eckert, E. R. G. and Soehngen, E., "Interferometric Studies on the Stability and Transition to Turbulence of a Free Convection Boundary Layer," *Proceedings of General Discussion on Heat Transfer*, London, ASME-IME, pages 321-323, 1951.

42. Eckert, E. R. G. and Soehngen, E., "Distribution of Heat Transfer Coefficients Around Circular Cylinders in Crossflow at Reynolds Numbers from 20 to 500," *ASME Journal of Heat Transfer*, pages 343-347, April, 1952.

43. Bartalsky, S. L., "Free Convection on a Vertical Plate Under Conditions of Non-Uniform Surface Temperature Distribution," M.S. Thesis, Air Force Institute of Technology, August, 1958.

44. Holman, J. P., Gartrell, H. E., and Soehngen, E., "An Interferometer Method of Studying Boundary Layer Oscillations," *ASME Journal of Heat Transfer*, Volume 80, pages 263-264, 1960.

45. Brodowicz, K., "An Analysis of Laminar Free Convection Around Isothermal Vertical Plates," *International Journal of Heat and Mass Transfer*, Volume II, Number 2, pages 201-209, 1968.

46. Haug, R. E., Stevenson, W. H., and Winter, E. R. F., "An Interferometer Study of Thermal Stratification by Natural Convection in a Contained Liquid," *Warme und Stoffubertragung*, Bd. 1, pages 251-253, 1968.

47. Harnett, J. P. and Irvine, T. F., editors, *Advances in Heat Transfer*, Hauf, W. and Grigull, U., "Optical Methods in Heat Transfer," Volume 6, pages 133-366, 1970.

48. Bryngdahl, O., "Application of Shearing Interferometry," *Progress in Optics*, Volume 4, North-Holland Publishing Company, Amsterdam, pages 39-83, 1965.

49. Waetzmann, E., *Annalen der Physik*, Volume 39, page 1042, 1912.

50. Normarski, G., Brevet Francais Numbers 1059.123 and 1059.124.

51. Normarski, M. G., "Microintérferométre différentiel á ondes polarisees," *Journal de Physique et Radium*, Volume 16, 59-13, 1955.

52. Normarski, M. G., "Remarques sur le fonctionement d'une classe de dispositifs interférentiels á polarisation, preséntation de quelques experiences nouvelles," *Journal de Physique et Radium*, Volume 17, 51-3, 1956.

53. Philbert, M., "Interferentialstrioscopy as Applied to Aerodynamics," *Recherche Aeronautique*, Number 59, published by O.N.E.R.A., 1957.

54. Philbert, M., "Application Metrologiques de la Strioscopie Interferentielle," *Revue D'Optique*, Volume 37, pages 598-608, 1958.

55. Philbert, M., "Emploi de la Strioscopie Interferentielle en Aerodynamique," *Recherche Aeronautique*, Volume 65, pages 19-27, 1958.

56. Philbert, M. and Dubois, G., "La Visualisation Des Ecoulements Aérodynamiques A Faible Masse Spécifique," *Recherche Aeronautique*, Volume 68, pages 31-35, 1961.

57. Waterhouse, J. F. and Spence, H. B., "The Application of the Schlieren Interferometer to the Study of Supersonic Flow Around Unyawed Axi-Symmetric Bodies," *Journal of the Royal Aeronautical Society*, Volume 65, pages 703-706, 1961.

58. Chevalerias, R., Latron, Y., and Veret, C., "Methods of Interferometry Applied to the Visualization of Flows in Wind Tunnels," *Optical Society of America Journal*, Volume 47, pages 703-706, 1957.

59. Oertel, H., "Differentialinterfenzaufnahmen Kurzzeitiger Hyperschallströmungen," *Kino-Technik*, Volume 16, Number 2, pages 29-34, February, 1962.

60. Smeets, G., "Differentialinterferometer Zur Beofachtung and Ausmessung Von Grenzschichten," Note Technique-Technische Mitteilung, Institute Franco-Allemand de Réserches de Saint Louis, Deutsch-Französisches Forchung-institut Saint Louis, September, 1960.

61. Smeets, G., "Photographs with the Differential Interferometer and their Evaluation," *Proceedings of the Eighth International Congress on High Speed Photography*, Stockholm, Sweden, pages 374-378, 1968.

62. Kramer, C., "Die Differentialinterferometric als Messverfahren der gasdynamischen Forchung," Abh. Aerodynamics Institute, Technische Hochschule, Aachen, Number 18, pages 37-43, 1965.

63. Solignac, J. L., "Examples D'Application Des Methodes De Mesure Optique A Des Recherches Fondamentales D'Aerodynamique, *Organization Du Traite De L'Atlantique Nord*, Rapport 398.

64. Brown, D., "A Shearing Interferometer with Fixed Shear and Its Application to Some Problems in the Testing of Astro-Optics," *The Proceedings of the Optical Society, The Physical Society*, Volume 67B, page 232, 1954.

65. Brown, D. S., "The Application of Shearing Interferometry to Routine Optical Testing," *Journal of Scientific Instruments*, The Institute of Physics and the Physical Society, Volume 32, pages 137-139, 1955.

66. Brown, D. S., "Radial Shear Interferometry," *Journal of Scientific Instruments*, The Institute of Physics and the Physical Society, Volume 39, pages 71-72, 1961.

67. Prasad, J., "Comparative Studies of Optical Path Difference Measurement with Michelson and Polarisation Interferometers," *Physics and Chemistry of Glasses*, Volume 4, pages 112-115, 1963.

68. Tsurruta, T., "Measurement of Transfer Functions of Photographic Objectives by Means of a Polarizing Shearing Interferometer," *Optical Society of America Journal*, Volume 53, page 1156, October, 1963.

69. Tsurruta, T., "A New Type of Shearing Interferometer for the Measurement of Transfer Functions of the Microscope Objective, *Applied Optics*, Volume 2, pages 371-378, April, 1963.

70. Lamb, J. D. and Schreiber, P. W., "The Application of a Differential Interferometer to an Axially Symmetric Arc Heated Plasma," Aerospace Research Laboratories, No. ARL 66-0222, November, 1966.

71. Bryngdahl, O. and Ljunggren, S., "A New Refractive Index Gradient Recording Interferometer Suitable for Studying Diffusion, Electrophoresis, and Sedimentation," *Journal of Physical Chemistry*, Volume 64, pages 1264-1270, 1960.

72. Bryngdahl, O., "Wavefront-Shearing Interferometer for Direct Recording of the Refractive Index Gradient in Cartesian Coordinates," *Optical Society of America Journal*, Volume 53, pages 571-576, 1963.

73. Bryngdahl, O., "The Accurate Estimation of the Thermal Conductivity Properties in Liquids by Means of a Shear-Interferometric Method," *Arkiv För Fysik*, Volume 21, paper 22, pages 289-369, 1962.

74. Bryngdahl, O., "Determination of Thermal Conductivity by the Non-Stationary Heated Wire Method," *Zeitchrift Für Angewandte Physik*, Volume 16, pages 258-262, 1963.

75. Ingelstam, E., "Measurements of Optical Path Gradients by Means of Birefringence Interference," *Arkiv För Fysik*, Volume 9, pages 197-226, 1955.

76. Ingelstam, E., "Some Quantitative Measurements of Path Differences and Gradients by Means of Phase Contrast and New Interferometric Devices," *Optical Society of America Journal*, Volume 47, pages 536-544, 1957.

77. Mordchelles-Regnier, G. and Kaplan, C., "Visualization of Natural Convection on a Plane Wall and in a Vertical Gap by Differential Interferometry, Transitional and Turbulent Regimes," *Proceedings of the Heat Transfer and Fluid Mechanics Institute*, Stanford University Press, page 94, 1963.

78. Spence, G., "An Investigation of Transient Free Convection Inside a Horizontal Cylinder by Means of Differential Interferometry," Master of Science Thesis in Mechanical Engineering, Georgia Institute of Technology, 1968.

79. Black, W. Z. and Carr, W. W., "Application of a Differential Interferometer to the Measurement of Heat Transfer Coefficients, *The Review of Scientific Instruments*, Volume 42, pages 337-340, 1971.

80. Black, W. Z. and Carr, W. W., "A Differential Interferometer and its Application to Heat and Mass Transfer Measurements, ASME Paper No. 72-HT-12, presented at the ASME-AIChE Heat Transfer Conference, Denver, Colorado, August, 1972.

81. Sernas, V. and Fletcher, L. S., "A Schlieren Interferometer Method for Heat Transfer Studies," *ASME Journal of Heat Transfer*, Volume 92, pages 202-204, 1970.

82. Sernas, V., Fletcher, L. S., and Aung, W., "Heat Transfer Measurements with a Wollaston Prism Schlieren Interferometer," ASME Paper No. 72-HT-9, presented at the ASME-AIChE Heat Transfer Conference, Denver, Colorado, August, 1972.

83. Grossin, R., Jannot, M., and Viannay, S., "Schlieren Visualization Device Allowing An Arbitrary Orientation of the Lines with Respect to the Scanning Direction," *Applied Optics*, Volume 10, pages 201-204, 1971.

84. Wollaston, W. H., "On the Method of Cutting Rock for Micrometers," *Philosophical Transactions of the Royal Society*, Volume 110, pages 126-131, 1820.

85. Gebhart, B., "Transient Natural Convection from Vertical Elements," *ASME Journal of Heat Transfer*, Volume 83, pages 61-70, 1961.

86. Gebhart, B., "Transient Natural Convection from Vertical Elements - Appreciable Thermal Capacity," *ASME Journal of Heat Transfer*, Paper No. 62-HT-10.

87. Gebhart, B. and Adams, D. E., "Measurement of Transient Natural Convection on a Flat Vertical Surface," *ASME Journal of Heat Transfer*, Paper No. 62-HT-25.

88. Gebhart, B., "Transient Natural Convection for Vertical Elements for Time Dependent Internal Energy Generation - Appreciable Thermal Capacity," *International Journal of Heat and Mass Transfer*, Volume 6, pages 951-957, 1963.

89. Gebhart, B., "Natural Convection Cooling Transients," *International Journal of Heat and Mass Transfer*, Volume 7, pages 479-483, 1964.

90. Ostrach, S., "An Analysis of Laminar Free Convection Flow and Heat Transfer About a Flat Plate Parallel to the Direction of the Generating Body Force," NACA Report 1111, 1953.

91. Herman, R., "Heat Transfer by Free Convection from Horizontal Cylinders in Diatomic Gases, NACA TM 1366, November, 1954.

92. Dougall, R. S., Chiang, T., and Fand, R. M., "A Study of the Differential Equations of Coupled Vibrations from a Heated Horizontal Cylinder," USAF Aeronautical Research Laboratories, ARL-TN 146, 1961.

93. Holman, J. P., *Heat Transfer*, page 170, McGraw-Hill Book Company, New York, 1968.

94. Oosthuizen, P. H. and Madan, S., "Combined Convective Heat Transfer from Horizontal Cylinders in Air," *ASME Journal of Heat Transfer*, Volume 92, pages 194-196, 1970.

95. Oosthuizen, P. H. and Madan, S., "The Effect of Flow Direction on Combined Convective Heat Transfer from Cylinders to Air," *ASME Journal of Heat Transfer*, Volume 93, pages 240-242, 1971.

96. Weast, R. C., Editor, *Handbook of Chemistry and Physics*, 50th Edition, the Chemical Rubber Company, page E-233, 1969-1970.

97. *The NBS-NACA Table of Thermal Properties of Gases*, National Bureau of Standards, page C544, 1949.

98. Touloukian, Y. S., Liley, P. E., and Soxena, S. C., "Thermal Conductivity," *Thermophysical Properties of Matter*, Volume 3, New York: IFI/Plenum, pages 512-514, 1970.

99. Hansen, A. G., *Fluid Mechanics*, First Edition, John Wiley and Sons, Inc., New York, 1967.

100. Kreith, F., *Principles of Heat Transfer*, Second Edition, The Haddon Craftsmen, Inc., Scranton, Pennsylvania, 1965.

101. Lin, C. C., "Motion in the Boundary Layer with a Rapidly Oscillating External Flow," *Proceedings of the 9th International Congress of Applied Mechanics*, page 135, 1959.

102. Businger, P. and Golub, G. H., "Linear Least Squares Solution by Householder Transformations," *Numerische Mathematik*, Volume 7, pages 269-276, 1965.

103. Berghaus, D. G., "A Least Squares Method for Overdetermined Photoelastic Stress Solutions," unpublished paper, Engineering Science and Mechanics, Georgia Institute of Technology, Atlanta, Georgia, 1971.

104. Chiang, T. and Kaye, J., "On Laminar Free Convection from a Horizontal Cylinder," *Proceedings of the Fourth United States National Congress of Applied Mechanics*, New York, ASME Volume 2, pages 1213-1219, 1962.

105. Wachtell, G., "Refraction Error in Interferometry of Boundary Layers in Supersonic Flow Along a Flat Plate," Ph.D. Thesis, Princeton University, 1951.

VITA

Wallace Woodrow Carr was born in Nansemond County, Virginia, on March 12, 1943, the son of Elsie McClenny Carr and John Morris Carr. He was educated in the public schools of Nansemond County and graduated from Holland High School in June, 1961. He entered the University of Virginia in the fall of that year, and in June of 1966, graduated with a Bachelor of Mechanical Engineering degree. During the summer of 1966, he worked as a mechanical engineer in the Nuclear Engineering Department of the Norfolk Naval Shipyard in Portsmouth, Virginia.

In the fall of 1966, he entered the graduate program at Georgia Institute of Technology and was awarded a National Aeronautics and Space Administration Graduate Traineeship. He was enrolled in the doctoral program and completed requirements for the Master of Science in Mechanical Engineering in June, 1968. In 1969 he was the recipient of the National Defense Education Act Graduate Fellowship, and in 1971, was a graduate research assistant in the School of Mechanical Engineering at Georgia Institute of Technology.

Mr. Carr was married in June, 1967, to the former Catherine Beale Young.